

An experimental investigation on the fate of xenocrystic garnet in kimberlitic melts under upper mantle conditions

by
Marelize Grobbelaar

*Thesis presented in fulfilment of the requirements for the degree of Master
of Science at the University of Stellenbosch*



Supervisor: Prof. Gary Stevens
Faculty of Science
Department of Earth Science

March 2015

DECLARATION

By submitting this thesis electronically, I declare that the entirety of the work contained therein is my own, original work, that I am the authorship owner thereof (unless to the extent explicitly otherwise stated) and that I have not previously in its entirety or in part submitted it for obtaining any qualification.

Signature:

Date:

ABSTRACT

Insets of large anhedral minerals in kimberlites are proposed to mainly have their origin from the disaggregation of mantle-derived xenoliths through mechanical abrasion by the ascending kimberlite magma. Garnet, despite being an important constituent of both mantle-derived peridotite and eclogite, forms only a minor constituent of kimberlites. This suggests that a large proportion of garnet liberated into the kimberlite through the disaggregation of such xenoliths, is consumed before the emplacement of kimberlite. This study records the breakdown mechanism of garnet by the ascending kimberlite magma by conducting experiments between pressures of 2 and 4 GPa and temperatures between 1100 and 1300°C. The starting material used in the experiments was prepared from a natural hypabyssal kimberlite that closely resembles the composition of a proposed primary Group I kimberlite magma. To the kimberlite material 5 wt % garnet, sourced from a natural peridotite, was added. It was found that garnet is not a stable equilibrium phase within the kimberlite magma under the investigated temperature and pressure conditions. Based on large volumes of phlogopite in the experiments it is concluded that garnet melts incongruently in the kimberlite magma to form phlogopite as a peritectic product and melts transitional in composition between silicate and carbonate melts. This is in contrast to more SiO₂-rich melt compositions produced as a consequence of the incongruent breakdown of both orthopyroxene and omphacite within kimberlite magmas. The consequence of the melt compositions produced in the experiments is increased solubility of CO₂ in the form of carbonate (CO₃²⁻). This finding has implications for both kimberlite ascent mechanisms and the solubility of diamond transported within kimberlite magmas.

UITTREKSEL

Dit word voorgestel dat groot oneenvormige mineraalinsluitels in kimberliet hoofsaaklik afkomstig is van xenolitiese mantelmateriaal wat verbrokkel weens die meganiese werking van die stygende kimberliet magma. Ten spyte daarvan dat granaat 'n belangrike komponent is van peridotiet en eklogiet xenoliete afkomstig uit die mantel, vorm granaat slegs 'n geringe deel van die kimberliet mineraalsamestelling. Dit dui daarop dat 'n beduidende gedeelte van die granaat wat vrygestel word in die kimberliet magma deur die verbrokkeling van xenolitiese materiaal, afgebreek word deur die stygende kimberliet magma voordat dit stol. Hierdie studie ondersoek die afbreekmeganisme van granaat afkomstig van die mantel in die stygende kimberliet magma deur eksperimente uit te voer by drukke tussen 2 en 4GPa en temperature tussen 1100 en 1300°C. Die materiaal met die aanvang van die eksperimente was voorberei uit 'n natuurlike hipabissale kimberliet wat soortgelyk is in samestelling as 'n voorgestelde primêre Groep I kimberliet magma se samestelling. Vyf gewigsprosent (5 wt %) granaat, verkry van 'n natuurlike peridotiet, is bygevoeg tot die kimberlietmateriaal. Daar is gevind dat granaat nie 'n stabiele ewewigsfase is in die kimberliet magma binne die temperatuur-en drukstoestand ondersoek nie. Groot volumes flogopiet teenwoordig in die eksperimente dui daarop dat granaat inkongruent smelt in die kimberliet magma om flogopiet as 'n peritektiese produk te vorm te same met 'n smelt wat neig na 'n karbonatiese smeltsamestelling. Die bevinding is in teenstelling met meer SiO₂-ryke smeltsamestellings as gevolg van die inkongruente afbreek van beide ortopirokseen en omfasiet in die kimberliet magma. Die gevolg van die meer karbonatiese smeltsamestellings, is 'n toename in die oplosbaarheid van CO₂ in die smelt in die vorm van karbonaat (CO₃²⁻). Die bevinding het nagevolge vir beide kimberliet stygingsmeganismes asook die oplosbaarheid van diamant tydens die vervoer van diamant deur kimberliet magmas.

ACKNOWLEDGEMENTS

I would like to thank my supervisor, Professor Gary Stevens (University of Stellenbosch). Professor Stevens provided insight and advice on experimental and analytical techniques as well as valuable guidance in the interpretation of the results obtained through this study. Additionally, Dr Marcos Garcia Arias (University of Stellenbosch) provided valuable instruction on the construction of the experimental assemblage and the use and accuracy of experimental equipment.

I would also like to thank Professor John J. Gurney (MS Group, Cape Town, South Africa), Dr Richard A. Brooker (University of Bristol) and Dr Rudolph M. Erasmus (University of Witwatersrand). Professor Gurney shared his knowledge about kimberlite in general, the compositions of mantle-derived garnet and the use of garnet during diamond exploration. Dr Brooker gave constructive advice on the interpretation of the behaviour of volatiles as a function of kimberlite melt composition. Dr Erasmus performed the micro-Raman spectroscopic analyses on the samples. Additionally, Professor Anton le Roex (University of Cape Town) provided the kimberlite used in the starting material.

The research for this study was made possible by funding from the South African National Research Foundation (NRF) in the form of grant funding to Professor G Stevens via the SARChI programme and an MSc Bursary to M. Grobbelaar

Table of Contents

Declaration	i
Abstract	ii
Uittreksel	iii
Acknowledgements	iv
Table of Contents	v
List of Figures	viii
List of Tables	x
Introduction	1
Previous experimental investigations on the interaction of xenocrysts with kimberlite magmas	4
Experimental technique	9
<i>Piston cylinder apparatus</i>	9
<i>Capsules</i>	9
<i>Starting materials</i>	10
Analytical techniques	13
<i>Scanning electron microscope</i>	13
<i>Micro-Raman spectroscopy</i>	13
Results	14
<i>Textural description of run products</i>	15
<i>Phase Chemistry</i>	21
<i>Olivine</i>	29
<i>Clinopyroxene</i>	29
<i>Phlogopite</i>	29
<i>Garnet</i>	30
<i>Apatite</i>	32
<i>Ilmenite</i>	32

<i>Spinel</i>	33
<i>Perovskite</i>	33
<i>Melt</i>	33
<i>High temperature experiments and Fe-loss to AgPd capsules</i>	37
<i>Modal proportions</i>	37
Discussion	39
<i>Reliability of results</i>	39
<i>Garnet</i>	39
<i>Garnet stability</i>	39
<i>Mechanism of garnet breakdown</i>	40
<i>Controls on garnet recrystallization</i>	40
<i>Melt compositions</i>	43
<i>Variation in melt composition due to changing PT conditions and charge mineralogy</i>	43
<i>Comparison between melt compositions produced in the present study and melt compositions produced in two related experimental investigations on orthopyroxene and omphacite breakdown in kimberlite melts under comparable PT conditions</i>	48
<i>Controls on carbonate content</i>	51
<i>Consequences of carbonate abundance</i>	53
Conclusion	54
References	55
<u>Appendices</u>	61
Appendix 1: <i>Internal standards used during SEM analysis of mineral phases in run products and results of SEM analysis of standard reference materials.</i>	61
Appendix 2: <i>Back-scattered electron images of textural characteristics of run products.</i>	63
Appendix 3: <i>Electron microprobe analyses of minerals produced in the experiments.</i>	69
Appendix 4: <i>Electron microprobe analyses of quenched melt produced in the experiments.</i>	89

Appendix 5: <i>Electron microprobe analyses of minerals produced in MG-11 (1300°C, 3GPa) and back-scattered electron images of MG-11 (1300°C, 3GPa).</i>	96
Appendix: 6: <i>Melt compositions produced in experiments of Jacobs (2012) and Burness (2013) and modal proportion estimates of phases produced in the experiments of Jacobs (2012) and Burness (2013)</i>	99

List of Figures

Figure 1: <i>P-T diagram of mineral assemblages produced during the experiments</i>	14
Figure 2: <i>Back-scattered electron image of quenched melt separated from adjacent olivine</i>	15
Figure 3: <i>Back-scattered electron images of the textural features produced in the experiments.</i>	17
Figure 4: <i>Back-scattered electron images showing textural characteristics of remnant garnet crystals in MG-05 (1200°C, 3GPa).</i>	18
Figure 5: <i>Compositional variation in remnant garnet crystal in MG-05 (1200°C, 3GPa) garnet.</i>	19
Figure 6: <i>Back-scattered electron images showing textural characteristics of remnant garnet crystal in MG-07 (1100°C, 4GPa)</i>	20
Figure 7: <i>Garnet compositions. Atomic proportion plots of Si versus Ti and (Al + Cr) versus Ti</i>	31
Figure 8: <i>Garnet compositions: Ternary plot showing the variation in the proportions pyrope, almandine and grossular between the different compositional zones in remnant garnet crystals</i>	32
Figure 9: <i>Comparison of melt compositions produced in the experiments to geochemically determined estimates of primary kimberlite compositions</i>	35
Figure 10: <i>Background-subtracted Raman spectra of melts in MG-01 (1100°C, 2GPa), MG-04 (1100°C, 3GPa) and MG-08 (1200°C, 4GPa)</i>	36
Figure 11: <i>Simplified diagram depicting the dynamic change in melt composition at the reaction interface between garnet and the kimberlite melt.</i>	42

Figure 12: Comparison of melts produced in the experiments to the starting composition as a function of molar concentration Ca, Mg, Fe and Si; and molar concentration Ca, P and Si	45
Figure 13: Comparison of melt compositions produced in the experiments for selected major oxides as a function of the modal phase assemblage	47
Figure 14: Comparison of the compositions of melts produced in the present study for selected oxides to melts produced in two related experimental investigations using the same starting kimberlite composition but with xenocrystic orthopyroxene (Jacobs, 2012) and omphacite respectively (Burness, 2013)	49
Figure 15: Comparison of the modal phase assemblage produced in the experiments of the present study to the modal phase assemblages produced in the pyroxene-melting experiments of Jacobs (2012) and Burness (2013).	50
Figure 16: Silicate-carbonate transition (Brooker et al., 2011)	52
<u>Appendices</u>	
Figure A.1: Back-scattered electron images of MG-01 (1100°C, 2GPa)	63
Figure A.2: Back-scattered electron images of MG-04 (1100°C, 3GPa)	64
Figure A.3: Back-scattered electron images of MG-05 (1200°C, 3GPa)	65
Figure A.4: Back-scattered electron images of MG-07 (1100°C, 4GPa)	66
Figure A.5: Back-scattered electron images of MG-08 (1200°C, 4GPa)	67
Figure A.6: Back-scattered electron images of MG-09 (1100°C, 4GPa, 6 hours)	68
Figure A.7: Back-scattered electron images of MG-11 (1300°C, 3GPa)	98

List of Tables

Table 1: <i>Compositions of the kimberlite sample and mineral xenocrysts used as starting materials in the experimental investigation of Chepurov et al. (2013).</i>	7
Table 2: <i>Garnet compositions produced in the experimental investigation of Chepurov et al. (2013).</i>	8
Table 3: <i>Proposed estimates of primary kimberlite magma compositions based on geochemical arguments.</i>	11
Table 4: <i>Compositions of the starting material and the components from which it was prepared.</i>	12
Table 5: <i>Representative compositions of olivine produced in the experiments.</i>	21
Table 6: <i>Representative compositions of clinopyroxene produced in the experiments.</i>	22
Table 7: <i>Representative compositions of phlogopite produced in the experiments.</i>	23
Table 8: <i>Representative compositions of garnet produced in the experiments.</i>	24
Table 9: <i>Representative compositions of apatite produced in the experiments.</i>	26
Table 10: <i>Representative compositions of spinel, ilmenite and perovskite produced in the experiments.</i>	27
Table 11: <i>Representative compositions of quenched melts produced in the experiments.</i>	28
Table 12: <i>Modal proportion estimates of phases within run products.</i>	38
Table 13: <i>Composition of the starting material used in the experiments, the composition of the kimberlite composition ADF 1 and representative compositions of the melts produced in experiments: MG-07 and MG-09.</i>	44

Appendices

Table A.1: <i>Internal standards used during SEM analysis of mineral phases produced in experiments.</i>	61
Table A.2: <i>Results of electron microprobe analyses of standard reference materials.</i>	62
Table A.3: <i>Electron microprobe analyses of olivine produced in experiments.</i>	69
Table A.4: <i>Electron microprobe analyses of clinopyroxene produced in experiments.</i>	73

Table A.5: <i>Electron microprobe analyses of phlogopite produced in experiments.</i>	76
Table A.6: <i>Electron microprobe analyses of garnet produced in experiments.</i>	79
Table A.7: <i>Electron microprobe analyses of apatite produced in experiments.</i>	83
Table A.8: <i>Electron microprobe analyses of spinel produced in experiments.</i>	85
Table A.9: <i>Electron microprobe analyses of ilmenite produced in experiments.</i>	86
Table A.10: <i>Electron microprobe analyses of perovskite produced in experiments.</i>	88
Table A.11: <i>Electron microprobe analyses of quenched melts produced in MG-01 (1100°C, 2GPa).</i>	89
Table A.12: <i>Electron microprobe analyses of quenched melts produced in MG-04 (1100°C, 3GPa).</i>	90
Table A.13: <i>Electron microprobe analyses of quenched melts produced in MG-05 (1200°C, 3GPa).</i>	91
Table A.14: <i>Electron microprobe analyses of quenched melts produced in MG-07 (1100°C, 4GPa).</i>	92
Table A.15: <i>Electron microprobe analyses of quenched melts produced in MG-08 (1200°C, 4GPa).</i>	93
Table A.16: <i>Electron microprobe analyses of quenched melts produced in MG-09 (1100°C, 4GPa, 6hours).</i>	94
Table A.17: <i>Electron microprobe analyses of quenched melts produced in the experiments. Recalculated to molar concentration.</i>	95
Table A.18: <i>Electron microprobe analyses of mineral phases of MG-11 (1300°C, 3GPa).</i>	96
Table A.19: <i>Melt compositions produced in experiments of Jacobs (2012) and Burness (2013).</i>	99
Table A.20: <i>Modal proportion estimates of phases in run products of Jacobs (2012) and Burness (2013).</i>	100

1. Introduction

Kimberlites have been the subject of intense scientific investigation that can largely be ascribed to their economic significance as the primary host of diamonds (Harris et al., 2004; le Roex et al., 2003; Stachel and Harris, 2008). Kimberlites are almost exclusively located within the boundaries of ancient cratons and originate at depths in excess of 150km within the Earth's interior (Russel et al., 2012; Sparks et al., 2006) from which the low viscosity magmas rises rapidly to their emplacement environment (Canil and Fedortchouk, 1999; Sparks et al., 2006, Spera, 1984). Kimberlite magmas typically transport a large cargo of mantle- derived xenoliths and xenocrysts, providing researchers with a means to directly study the composition of the sub-continental lithospheric mantle (le Roex et al., 2003; Schulze, 2003) and has fundamentally shaped the view that the sub-continental lithospheric mantle has a predominantly peridotitic and eclogitic nature (Griffin et al., 2009; Schulze, 2003). Furthermore, kimberlites have unusual chemistry that is characterised by low SiO₂ and high volatile contents with elevated concentrations of both incompatible and compatible trace elements (Becker and le Roex, 2006; Harris et al., 2004; le Roex et al., 2003; Mitchell, 2008). The major and trace element geochemistry of kimberlites indicate that they arise from small degrees of previously depleted metasomatised mantle source rocks. The abovementioned considerations have resulted in a substantial body of geochemical (Becker and le Roex, 2006; Harris et al., 2004; Kopylova et al., 2007; le Roex et al., 2003; Price et al., 2002) and experimental (Brey et al., 2008; Dalton and Presnall, 1998; Girnir et al., 1995; Moore and Wood, 1998) research aimed at elucidating the primary nature of kimberlite magmas and the composition of source rocks that, through partial melting, can produce magmas with such unusual compositions. The majority of researchers are in agreement that kimberlite magmas arise from small degrees of partial melting of carbonated garnet peridotite. The interaction of entrained mantle minerals with the ascending kimberlite magma has only more recently become the focus of experimental investigations (Canil and Fedortchouk, 1999; Chepurov et al., 2013; Jacobs, 2012; Russel et al., 2012).

Kimberlites are characterised by an inequigranular texture of larger grains set within a finer grained matrix (Clement et al., 1984). The larger grains usually occur as anhedral individual crystals or crystal aggregates and are referred to as macrocrysts (Arndt et al., 2010). The macrocrystic minerals include the following: olivine, phlogopite, picroilmenite, Cr-spinel, pyrope garnet, clinopyroxene and orthopyroxene (Clement et al., 1984). These macrocrysts are believed to mainly originate from the disintegration of mantle-derived xenoliths through mechanical abrasion by the ascending kimberlite magma (e.g. Arndt et al., 2010; Brett et al., 2009; Clement et al., 1984). An inference supported by the habit the macrocrysts assume and

deformation characteristics not usually attributed to minerals primary to magma crystallisation (Arndt et al., 2010; le Roex et al., 2003). A consequence of the foreign nature of the ferromagnesian silicate macrocrystic minerals is disequilibrium with the host kimberlite magma (Canil and Fedortchouk, 1999; Russel et al., 2012). Orthopyroxene, as the most SiO₂-rich of the macrocrystic minerals, is the most reactive within the silica-undersaturated host kimberlite magma (Russel et al., 2012). Therefore, the paucity of orthopyroxene in kimberlite, despite being an important constituent (10-50 vol %; Mitchell, 2008) of mantle-derived xenoliths, is attributed to rapid and efficient dissolution by the kimberlite magma (e.g. Chepurov et al., 2013; Jacobs, 2012; Mitchell, 2008; Russel et al., 2012). In the rare instances orthopyroxene is observed in kimberlites, the reaction relationship is documented by the formation of reaction rims around orthopyroxene (Arndt et al., 2010; le Roex et al., 2003; Russel et al., 2012).

Mineral assemblages, mineral chemistry and melt composition are influenced by processes of assimilation and crystallisation during magma ascent (Ogilvie-Harris et al., 2009; Kavanagh and Sparks, 2009). Mitchell (2008) noted that assimilation of orthopyroxene by kimberlite magmas has important consequences for the SiO₂ and volatile content of kimberlite melts. Subsequently, Jacobs (2012) experimentally determined that orthopyroxene melts incongruently within kimberlite magmas under upper mantle conditions leading to olivine crystallisation while enriching the kimberlitic melt in SiO₂. This finding is particularly important regarding CO₂ solubility in kimberlitic melts since CO₂ solubility, in addition to being pressure dependent, is a strong function of melt composition; CO₂ solubility decreases with the degree of polymerization (increased SiO₂) of melts (Brooker et al., 2001; Brooker et al., 2011; Spera, 1984). CO₂ exsolution is believed to be essential in the initiation and propagation of fractures through which kimberlites are thought to ascend (Spera, 1984; Wilson and Head, 2007) as well as acting as a buoyant propellant driving the rapid ascent of kimberlite magmas (Russel et al., 2012). Russel et al. (2012) experimentally showed that the assimilation of orthopyroxene by melts carbonatitic in nature can lead to melts of kimberlite-like composition. The increased SiO₂ content as a consequence of orthopyroxene assimilation is accompanied by a drastic decrease in the solubility of CO₂ in the melt and exsolution of a CO₂-rich fluid phase. The exsolved low density CO₂-rich fluid is proposed to aid the rapid ascent of kimberlite magmas (Russel et al., 2012).

Based on the findings of the fate of orthopyroxene within kimberlite magmas, a similar argument can be made for macrocrystic garnet. Although garnet is found ubiquitously within kimberlites it rarely exceeds accessory amounts, notwithstanding being an important constituent of mantle-derived peridotite and eclogite xenoliths (Arndt et al., 2010; Wood et al., 2013). Therefore a significant proportion of garnet liberated from the disaggregation of such xenoliths into the kimberlite magma is likely consumed before emplacement of kimberlite.

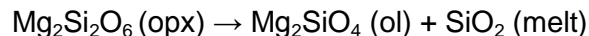
Exceptionally fast dissolution rates for garnet in kimberlite magmas have been experimentally documented by Canil and Fedortchouk, (1999); providing evidence for the rapid ascent of kimberlite magmas. As with orthopyroxene, the reaction relationship between garnet and kimberlite magmas is recorded by the formation of reaction rims at the expense of garnet (Dawson and Stephens, 1975; Hunter and Taylor, 1982, Ivanic et al., 2012). Despite the obvious reaction relationship between garnet and kimberlite magmas, a dearth of studies exist aimed at resolving the breakdown mechanism of garnet in kimberlite magmas or how the assimilation of garnet alters kimberlite melts during ascent.

The experimental investigations on the digestion of orthopyroxene by kimberlitic (Jacobs, 2012) and carbonatitic melts (Russel et al., 2012) underline the significance of such studies as a tool in understanding kimberlite petrogenesis. This study aims to record the digestion of peridotite garnet by ascending kimberlite magmas under upper mantle conditions in an attempt to identify the breakdown mechanism of garnet. Additionally, the effect of garnet breakdown on kimberlite melt compositions will be documented to determine whether the digestion of garnet by the kimberlite magma affects kimberlitic melts in a similar way as orthopyroxene and thus aid in the exsolution of CO₂ and the assimilation-driven buoyant ascent of the magma. This study experimentally replicates the interaction of entrained peridotite garnet in a proposed close-to-primary Group 1 kimberlite composition (Becker and le Roex, 2006) during ascent under upper mantle conditions (1100°C to 1300°C; 2 to 4GPa).

2. Previous experimental investigations on the interaction of xenocrysts with kimberlitic melts

Experimental investigations on the interaction of xenocrystic material with melts of kimberlitic and carbonatitic composition has shown the importance of such investigations in understanding the modification of the kimberlite magma as a consequence of xenocryst assimilation during ascent (Jacobs, 2012); in determining kimberlite magma ascent rates (Canil and Fedortchouk, 1999) and understanding processes that influence kimberlite magma ascent (Russel et al., 2012). Additionally, such studies have shown that different types of xenoliths might undergo different degrees of assimilation by the kimberlite magma as a result of variable stability of minerals within the kimberlite magma comprising such xenoliths (Chepurov et al., 2013).

Jacobs (2012) experimentally investigated the stability of peridotite-derived orthopyroxene within a natural aphanitic hypabyssal kimberlite sample (ADF1, Becker and le Roex, 2006) under upper mantle conditions (1100 to 1300°C; 2 to 3.5GPa). He found that orthopyroxene assimilation within the kimberlite composition used, is a strong function of both temperature and pressure. He determined that orthopyroxene melts incongruently at lower temperatures (1100 & 1200°C) and pressures (2 & 2.5 GPa) along the reaction:



At higher pressures (> 2.5 GPa), he found orthopyroxene to be stable and concluded that ~5.5% vol % olivine is added to the ascending kimberlite magma under the investigated conditions from the melting of ~8 vol % orthopyroxene.

Russel et al. (2012) performed open air experiments on mixtures of synthetic Na_2CO_3 and crushed natural orthopyroxene at temperatures of 1000 to 1100°C. The Na_2CO_3 was taken as an approximation of the composition of a natural carbonatitic melt. Melts of pure Na_2CO_3 was stable at these conditions and contained 44 wt % dissolved CO_2 . Melts of mixtures of Na_2CO_3 and orthopyroxene was accompanied by decarbonation indicated by weight loss which was taken as a quantitative measure of CO_2 loss. The authors proposed a mechanistic model for the rapid buoyantly-driven ascent of kimberlite magmas by exsolution of a CO_2 -rich fluid upon assimilation of orthopyroxene. The model requires that kimberlite magmas originate as carbonatitic melts evolving to more silicic kimberlite compositions through the assimilation of orthopyroxene. The increase in SiO_2 is accompanied by the gradual release of CO_2 up until a threshold SiO_2 content of 18 wt % is reached, after which, a drastic decrease in CO_2 solubility is seen. The authors mentioned that assimilation of other silicate phases such as garnet could also drive CO_2 exsolution, but that their dissolution rate might be too low to contribute

significantly to magma ascent. Two aspects of this study indicate that further investigation of this process is necessary. Firstly, the melt compositions used are a poor match with natural kimberlite magma compositions. Secondly, the compositional dependence of CO₂ solubility within melts is most drastic at low pressures (Brooker et al., 2011); the details of how digestion of entrained minerals occur at high pressure needs to be constrained by experimentation at realistic pressures.

Canil and Fedortchouk (1999) performed dissolution experiments on natural pyrope garnet spheres approximating 1mm in diameter in a H₂O-bearing (10 wt % H₂O) synthetic kimberlite composition in an effort to constrain kimberlite magma ascent rates. The synthetic kimberlite compositions were modelled after analyses of natural kimberlite and simplified to the system K₂O-MgO-Al₂O₃-SiO₂-CaO-FeO-H₂O±CO₂. FeO was replaced by CoO to prevent Fe-loss to platinum capsules. The starting composition contained either 10 wt % H₂O or 10 wt % CO₂; added as brucite or CaCO₃ respectively. The dissolution rate of garnet in the CO₂-bearing experiments could not be measured since the temperature these experiments were subjected to, exceeded the melting point of the garnet used in the experiments. Experimental pressures and temperatures were varied between 1.5 to 2.5 GPa and 1400 to 1550°C. The authors concluded that in order for the garnet to survive, the kimberlite magma can only remain at its liquidus temperature for a few minutes and kimberlite ascent has to occur within 1 to 10 hours at 1000 to 1200°C. Their findings suggest that the dissolution of garnet is strongly dependent on temperature at constant pressure and that pressure has an insignificant effect on garnet dissolution at constant temperature. Furthermore, to test the effect of garnet composition on its dissolution rate, an experiment was performed using a crustal-derived almandine-rich garnet. The authors found that the composition of garnet had a negligible effect on the dissolution rate.

Chepurov et al. (2013) experimentally tested the relative stabilities of ortho- and clinopyroxene, garnet and olivine derived from peridotite in a natural kimberlite composition at high pressure and temperatures (4GPa, 1300 to 1500°C). The kimberlite sample and one of each of the minerals under investigation were pressed into a cylindrical pellet such that the mineral grains were located in the centre of the charge. The starting composition of their experiments varied since the experimental design permitted the use of variable kimberlite sample weights (200mg and 100mg respectively) and mineral xenocrysts of 1-3mm in diameter. To illustrate this, two hypothetical starting compositions are tabulated together with the compositions of their kimberlite sample and xenocrystic minerals in Table 1. The variation in starting composition between experiments can influence the reactivity of the minerals under investigation as well as changing phase assemblages and phase compositions produced. Furthermore, a distorted view of dissolution rate can be created by variations in grain size. Smaller grains have a larger surface to volume ratio and are likely to react and dissolve faster

than larger grains (Putnis, 2009). The authors did not comment on the possible effect this had on their results. Under the conditions of the investigation it was determined that the pyroxenes are most reactive with the kimberlite melt while the reaction of olivine and garnet is more sluggish. Temperature dependent incongruent melting is proposed for both pyroxenes. This result led the authors to the conclusion that pyroxenites entrained in the kimberlite magma can decay to a greater degree than peridotites. The relic xenocrysts were zoned and differed slightly in composition to the original minerals indicating recrystallisation of the minerals during the experiments. Additionally, the reaction of both olivine and garnet was accompanied by the formation of a rim of compositionally distinct material containing inclusions of melt. In addition to the melt inclusions, the garnet rim contained olivine inclusions. The compositions for the recrystallised remnant garnet and the newly formed compositionally distinct garnet rims are tabulated in Table 2.

The studies discussed above, show that both mantle-derived orthopyroxene and garnet will breakdown as a result of interaction with kimberlite magmas. The incongruent melting of orthopyroxene alters the composition of kimberlitic melts in such a way as to lower CO₂ solubility of kimberlitic melts leading to CO₂ saturation and subsequent exsolution of CO₂. This process was only experimentally demonstrated to occur at low pressures but can be reasonably inferred to also occur at high pressure. Garnet breakdown within kimberlite magmas is rapid and accompanied by the growth of a rim of compositionally distinct garnet. The mechanism of garnet breakdown and the influence of the breakdown of garnet on the kimberlite melt composition and on the assemblage of minerals in equilibrium with the kimberlite melt however, remain unresolved.

Table 1: A: Compositions of the kimberlite sample and mineral xenocrysts used as starting materials in the experimental investigation of Chepurov et al. (2013). Only the wt % compositions were reported in the original study and the mineral formulae work has been calculated from the published information. B: Starting compositions are not reported in Chepurov et al. (2013), and the starting compositions presented are hypothetical; calculated to demonstrate the effect on the starting composition as a consequence of the use of mineral xenocrysts of variable size. The calculation was based on 100mg of kimberlite sample and mineral xenocrysts weighing 1.24mg (composition 1) and mineral xenocrysts weighing 6.13 mg (composition 2)

	A					B	
	Kimberlite sample	Grt	OI	Cpx	Opx	Starting composition 1	Starting composition 2
SiO ₂	32.08	42.69	40.47	54.42	56.28	32.85	35.31
TiO ₂	0.47	0.35	0.01	0.09	-	0.45	0.40
Al ₂ O ₃	3.71	21.48	-	3.38	2.32	3.86	4.32
Cr ₂ O ₃	-	2.10	0.04	1.08	0.57	0.04	0.19
FeO ^T	6.91	6.85	9.00	2.80	5.59	6.87	6.74
MnO	0.14	0.30	0.14	0.09	0.13	0.14	0.14
MgO	31.05	21.55	49.62	16.76	34.17	31.03	30.95
CaO	7.63	4.25	0.04	18.90	0.72	7.55	7.30
Na ₂ O	0.47	0.06	-	1.95	0.05	0.47	0.48
K ₂ O	1.74	-	-	0.02	0.01	1.66	1.40
P ₂ O ₅	0.31	-	-	-	-	0.30	0.25
NiO	-	-	0.41	0.06	-	0.01	0.02
LOI	16.18	-	-	-	-	15.42	12.99
Total	100.69	99.63	99.96	99.55	99.84	100.64	100.49
xO ²⁻		12	4	6	6		
Si	-	3.03	0.99	1.97	1.94	-	-
Ti	-	0.02	-	0.00	-	-	-
Al	-	1.80	-	0.14	0.09	-	-
Cr	-	0.12	0.00	0.03	0.02	-	-
Fe ²⁺	-	0.41	0.18	0.08	0.16	-	-
Mn	-	0.02	0.00	0.00	0.00	-	-
Mg	-	2.28	1.82	0.90	1.76	-	-
Ca	-	0.32	0.00	0.73	0.03	-	-
Na	-	0.01	-	0.14	0.00	-	-
K	-	-	-	0.00	-	-	-
P	-	-	-	-	-	-	-
Ni	-	-	0.01	0.00	-	-	-
ΣCations		8.00	3.01	4.01	4.00	-	-
Mg#		85	91	91	92	-	-

Table 2: Garnet compositions produced in the experimental investigation of Chepurov et al. (2013). The original study reported low proportions of sodium and potassium which have not been included. A: core composition; B and C: rim compositions of garnet in experiment 4-40-11(1400°C, 4 GPa & 5 min duration). D: core composition; E: rim composition of garnet in experiment 4-43-11 (1400°C, 4 GPa & 60 min duration). F and G: recrystallised garnet rim with distinct composition in experiment 4-43-11. Only wt % compositions were reported in the original study. The mineral formulae work has been calculated from the published information, with Fe³⁺ calculated according to Droop (1987). Site occupancy is based on the ideal unit formula of garnet (X₃Y₂Z₃O₁₂) given in Deer, Howie & Zussman (1992).

	A	B	C	D	E	F	G
T(°C)	1400	1400	1400	1400	1400	1400	1400
P(GPa)	4	4	4	4	4	4	4
Dur (min)	5	5	5	60	60	60	60
SiO ₂	42.08	41.58	43.47	41.8	42.9	41.4	40.6
TiO ₂	0.26	0.29	0.18	0.01	0.04	1.15	1.6
Al ₂ O ₃	20.37	20.27	21.59	20.7	21.7	18.3	17.6
Cr ₂ O ₃	4.35	3.28	3.03	4.6	2.39	0.63	0.26
Fe ₂ O ₃	1.61	-	0.82	0.77	0.57	7.16	7.62
FeO	5.18	5.07	3.42	5.91	4.50	1.96	2.94
MnO	0.28	0.23	0.15	0.2	0.06	0.08	0.13
MgO	21.72	24.13	24.67	21.3	24	19.1	16.5
CaO	4.74	4.48	3.51	4.6	3.7	10.3	12.7
Total	100.59	99.33	100.83	99.89	99.86	100.08	99.95
xO ²	12	12	12	12	12	12	12
Si	2.99	2.96	3.01	2.99	3.01	3.02	3.02
Al	0.01	0.04	-	0.01	-	-	-
ZO ₄ Tetrahedra	3.00	3.00	3.01	3.00	3.01	3.02	3.02
Ti	0.01	0.02	0.01	0.00	0.00	0.06	0.09
Al	1.69	1.66	1.76	1.73	1.79	1.58	1.54
Cr	0.24	0.18	0.17	0.26	0.16	0.04	0.02
Fe ³⁺	0.08	-	0.04	0.04	0.04	0.31	0.34
YO ₆ Octahedra	2.03	1.86	1.98	2.03	2.00	1.99	1.99
Fe ²⁺	0.29	0.30	0.19	0.34	0.21	0.09	0.15
Mn	0.02	0.01	0.01	0.01	0.00	0.00	0.01
Mg	2.30	2.56	2.55	2.27	2.51	2.08	1.83
Ca	0.36	0.34	0.26	0.35	0.28	0.81	1.01
X-ions	2.96	3.22	3.01	2.97	2.99	2.99	2.99
ΣCations	7.99	8.08	8.00	8.00	8.00	8.00	8.00
Mg#	89	89	93	87	92	96	93

3. Experimental technique

3.1. Piston cylinder apparatus

All experiments were conducted using a non-end-loaded piston cylinder apparatus fitted with a pressure plate of 10 mm internal diameter. Capsules were loaded into a pressure-furnace assembly which consisted of an outer NaCl-sleeve, a Pyrex thermal insulator sleeve, a graphite furnace tube and periclase filler pieces. The temperature was controlled by a Depths Of The Earth Temperature Control Unit (accurate to within 1°C). To minimize the effect of temperature gradients within capsules, the capsules were folded so that they were flat. The shortest dimension was placed parallel with the furnace, with the entire contents of the capsule within 3mm of the thermocouple tip. In this configuration the maximum error between the measured and actual temperature of the charge is ~ 5°C. Lower temperature (1100 and 1200°C) runs were monitored using type-K thermocouples whereas higher temperature (1300°C) runs were monitored using type-R thermocouples. Sample pressures reported are oil pressures and was taken as those given on a Heise Solid Front-CMM-31655 pressure gauge fitted to the hydraulic ram driving the carbide piston. Pressure measurement accuracy of the gauge is $\pm 0.1\%$ F.S. Discrepancies exist between the actual and measured experimental pressures due to loss of pressure along the length of the pressure chamber away from the piston face due to factors such as internal friction and the shear strength of the pressure medium (Johannes et al., 1971). To minimize errors associated with loss of pressure due to internal friction, the hot-piston out technique was used. Experiments were pressurized to 90% of the final experimental pressure. At this point a check was done that the thermocouple did not break during the initial pressurization, after which, experiments were heated at a rate of 100°C/min. Once the experimental temperature was reached the pressure was increased to ± 5 kbar above the final experimental pressure. Experiments were monitored and the pressure was adjusted accordingly if any change to the final experimental pressure was observed. Experiments were run for 6 to 48 hours. On completion of experimental runs, the experiments were isobarically quenched to room temperature within 30 seconds.

3.2. Capsules

Capsules were prepared from AgPd-tubing. Gold is the ideal material for construction of capsules used during rock melting experiments due to the slow rate of hydrogen diffusion through gold (Barr and Grove, 2010) and the fact that gold is largely inert to chemical interaction with silicate minerals and melts (Merrill and Wyllie, 1973). Temperatures required in melting experiments of mafic and ultramafic systems however, exceed the melting point of gold (Jakobsson, 2012). Absorption of Fe from sample material

by capsules made from Pt or AgPd-alloys is well documented (e.g. Barr and Grove, 2010; Jakobsson, 2012; Merrill and Wylie, 1973). Furthermore, it has been established that Pd-alloys are very efficient hydrogen diffusers (Holleck, 1970; Jakobsson, 2012). In an effort to contain both Fe-loss and hydrogen diffusion the Pd content of the alloy used in the experiments was adjusted according to the temperature of the experimental run: Ag₇₀Pd₃₀ capsules were used during lower temperature (1100°) runs while Ag₅₀Pd₅₀ and Ag₄₀Pd₆₀ capsules were used for higher temperature ($\geq 1200^\circ\text{C}$) runs. This method in limiting hydrogen diffusion is in accordance to Holleck (1970) who found that the activation energy for hydrogen diffusion increases with increasing silver content of the AgPd-alloy. Additionally, capsules were packed in a boron nitride plug, which is almost impermeable to hydrogen (Truckenbrodt et al., 1997). For each experiment, ~0.025g of prepared sample was packed into a capsule and arc-welded shut under a reducing gas to isolate the welding process from the atmosphere. This improved the quality of the weld. Subsequent to welding, capsules were leak tested in water under vacuum.

3.3. Starting materials

The experiments were conducted using a mixture of natural aphanitic hypabyssal kimberlite (ADF1; Becker and le Roex, 2006) proposed to closely approximate the composition of an average primary Group I kimberlite (Becker and le Roex, 2006) and peridotite garnet xenocrysts. Proposed estimates of primary kimberlite magmas based on geochemical considerations (Becker and le Roex, 2006; Harris et al., 2004; Kopylova et al., 2007; le Roex et al., 2003; Price et al., 2002) fall within a reasonably close compositional range (Table 3). For this reason a natural kimberlite sample, falling within these compositional limits, was chosen as the starting kimberlite composition. The powdered kimberlite sample was ground under acetone to obtain a uniform grain size of ~5 μm . Garnet xenocrysts approximating 1mm in diameter was handpicked under a reflecting microscope from the crushed peridotite sample. The garnet separate was ground in a pestle and mortar and passed through a series of sieves to yield a garnet xenocryst population of ~115 μm in size. Mixing of the kimberlite sample and garnet xenocrysts were done according to weight in the following proportion: ADF1 95%; garnet 5%. The resultant starting composition is given in Table 4 together with the composition of ADF1 and its mineral constituents as well as the average composition of the garnet xenocrysts. Variability in the major element chemistry, as determined by SEM analyses of the garnet xenocrysts, was negligible. The starting composition resembles that of an average primary Group 1 kimberlite composition as given in Becker and le Roex (2006). Compared to the average primary Group 1 kimberlite composition, the starting composition has increased concentrations of SiO₂, Al₂O₃ and Cr₂O₃ due to the addition of peridotite garnet. The lower

CaO and FeO content of the starting composition is the combined result of the composition of ADF1 and the peridotite garnet. A consequence of the composition of ADF1 is higher concentrations of P₂O₅, Na₂O and K₂O in the starting composition as compared to the average composition.

Table 3: Proposed estimates of primary kimberlite magma compositions based on geochemical arguments (in wt %; normalised to 100% anhydrous). A: Average Group 1 kimberlite composition (Becker and le Roex, 2006). B: Primitive Group 1 kimberlite. Average of samples k6/55, k8/115 and k119/2 which is proposed to closely resemble a primary Group 1 kimberlite composition (le Roex et al., 2003). C: Primitive Group 1 kimberlite. Average of sample UB-01 and UB-06 which is proposed to closely resemble a Group 1 kimberlite composition (Harris et al., 2004). D: Primitive Group 1 A kimberlite. Average of aphanitic hypabyssal kimberlite samples JD69 and JD82 (Price et al., 2000). E: Primitive kimberlite deep melt (Kopylova et al., 2007)

	A	B	C	D	E
SiO ₂	31.47	33.81	29.57	35.22	32.95
TiO ₂	3.10	1.95	3.83	0.78	2.14
Al ₂ O ₃	3.32	2.23	2.75	1.88	1.94
Cr ₂ O ₃	0.22	0.26	0.26	0.29	0.44
FeO ^T	11.61	9.66	10.96	7.68	9.35
MnO	0.23	0.22	0.22	0.19	0.22
MgO	30.32	34.46	30.88	29.06	34.86
CaO	15.96	14.11	17.84	23.03	15.92
Na ₂ O	0.19	0.16	0.06	0.22	0.12
K ₂ O	1.00	1.01	1.27	0.57	1.55
P ₂ O ₅	2.45	1.99	2.22	0.89	0.49
NiO	0.13	0.14	0.14	0.20	0.00
Total	100.00	100.00	100.00	100.00	100.00
H ₂ O ⁺	6.67	8.36	4.92	6.90	9.07
CO ₂	8.19	10.02	8.63	13.04	9.88

Table 4: Compositions (in wt %) of the starting material and the components from which it was prepared. A: starting material as calculated by weight (95 % ADF1 and 5 % garnet). B: bulk composition of Andriesfontein Group I kimberlite (ADF1) as reported in Becker and le Roex (2006) and its mineral constituents. C: garnet from a peridotite xenolith sourced from Bultfontein, South Africa. Numbers in parentheses are standard deviations.

	A	B							C
	Starting material	Kimberlite sample (ADF1)							Grt
		Bulk rock	Mineral compositions in kimberlite ADF1						
			Ap	Phl	Spl 1	Spl 2	Prv	OI	
SiO ₂	27.54	26.78	-	43.09	-	-	-	42.02	41.95 (0.20)
TiO ₂	1.68	1.75	-	1.05	11.21	6.59	57.73	-	0.26 (0.04)
Al ₂ O ₃	3.62	2.69	-	10.29	6.45	6.3	-	-	21.34 (0.14)
Cr ₂ O ₃	0.33	0.18	-	-	1.04	42.46	-	-	3.17 (0.04)
Nb ₂ O ₅	-	-	-	-	-	-	0.83	-	-
Fe ₂ O ₃	0.03	-	-	-	44.55	11.16	-	-	0.55 (0.18)
FeO	8.88	8.98	0.42	6.2	26.79	22.44	1.5	7.19	6.98 (0.21)
MnO	0.19	0.17	-	-	0.74	-	-	-	0.55 (0.12)
MgO	25.38	25.63	-	26.19	9.68	10.35	-	50.83	20.55 (0.10)
CaO	12.28	12.67	54.75	-	0.36	0.39	39.89	0.03	4.85 (0.10)
Na ₂ O	0.29	0.31	-	-	-	-	0.44	-	-
K ₂ O	0.94	0.99	-	9.76	-	-	-	-	-
P ₂ O ₅	3.97	4.18	40.48	-	-	-	-	-	-
SO ₃	0.03	0.03	-	-	-	-	-	-	-
NiO	0.15	0.16	-	-	-	-	-	0.21	-
F	0.00	0	2.67	-	-	-	-	-	-
H ₂ O ⁻	0.78	0.82	-	-	-	-	-	-	-
H ₂ O ⁺	7.50	7.89	-	-	-	-	-	-	-
CO ₂	5.23	5.5	-	-	-	-	-	-	-
Total	98.79	98.73	98.32	96.57	100.81	99.68	100.39	100.28	100.03
xO ²⁻			26	24	4	4	3	4	12
Si	-	-	-	6.06	-	-	-	1.01	2.99
Ti	-	-	-	0.11	0.29	0.17	0.99	-	0.01
Al	-	-	-	1.71	0.26	0.25	-	-	1.79
Cr	-	-	-	-	0.03	1.13	-	-	0.18
Nb	-	-	-	-	-	-	0.01	-	-
Fe ³⁺	-	-	-	-	1.14	0.28	-	-	0.03
Fe ²⁺	-	-	0.06	0.73	0.76	0.63	0.03	0.15	0.41
Mn	-	-	-	-	0.02	-	-	-	0.03
Mg	-	-	-	5.49	0.49	0.52	-	1.83	2.18
Ca	-	-	9.94	-	0.01	0.01	0.97	0.004	0.37
Na	-	-	-	-	-	-	0.02	-	-
K	-	-	-	1.75	-	-	-	-	-
P	-	-	5.81	-	-	-	-	-	-
Ni	-	-	-	-	-	-	-	0.01	-
F	-	-	1.43	-	-	-	-	-	-
ΣCations	-	-	15.81	15.85	3.00	3.00	2.01	2.99	8.00
Mg#	-	-	-	88	39	45	-	93	83

4. Analytical techniques

4.1. Scanning electron microscope

Analyses of the garnet xenocrysts and run products were done with a Zeiss EVO MA15VP SEM fitted with an Oxford X-Max EDS Silicon Drift Detector (SDD) at the University of Stellenbosch. Quantitative analysis was executed at an accelerating voltage of 20kV at a counting time of 10s per analysis and a working distance of 8.5mm. Minerals were analysed with a focused beam and the beam current was controlled by adjusting the spot size and maintained between 19-21nA. Internal standards used during analysis of individual minerals are listed in the appendix (Table A.1). Capsule walls were analysed operating in wavelength-dispersion mode (WDS) to test for Fe-loss. Peak and background counting times were 45s and 25s respectively. Melt analyses were done according to the cold stage method. The SEM was fitted with a Gatan cryogenic stage to allow reduction of analytical temperature to $\pm -180^{\circ}\text{C}$. This temperature reduces the migration of K, Na and H away from the site of beam and melt interaction during analysis. The beam was rastered over an area to obtain representative analyses for the melt phase. Accuracy of analyses was confirmed by analysing mineral standards of known compositions as unknowns (results given in the appendix; Table A.2). Mineral stoichiometry was calculated for mineral phases and the obtained mineral formulae were used to assess quality of analyses. Analyses falling beyond ± 0.02 of ideal stoichiometry was rejected (e.g. garnet = 8 ± 0.02 , olivine = 3 ± 0.02 ; pyroxene = 4 ± 0.02 etc.). Where appropriate, the Fe_2O_3 content for oxides and ferromagnesian silicates were calculated according to Droop (1987). A least squares mixing calculation method was used to calculate modal proportions of phases in samples.

4.2. Micro-Raman Spectroscopy

Micro-Raman spectroscopic analyses were performed on melts produced in experiments at the Raman facility of the University of Witwatersrand to qualitatively determine the presence of carbonate. Raman spectra were acquired with a Horiba LabRAM HR Raman spectrometer with an Olympus BX41 microscope attachment and the 514.5nm line of an argon ion laser as excitation source. The incident laser beam was focused onto the sample with a 100x objective and the backscattered light was dispersed via a 600 lines/mm grating onto a liquid nitrogen cooled CCD detector. Power at the sample was kept low ($<0,8$ mW) to avoid possible laser-induced heating.

5. Results

Products of successful experiments were mounted lengthwise in epoxy such that a vertical section through the run product was produced. These were ground on an abrasive disk to expose the sample surface and subsequently impregnated with epoxy under vacuum before final sectioning. In preparation of SEM analysis the samples were carbon coated.

Mineral assemblages produced in the experiments are shown in Figure 1. All runs produced olivine, clinopyroxene and phlogopite. The compositions of phases produced in the experiments are summarised in Table 5 to 11. For reasons discussed in Section 5.2.10, the 1300° experiments are omitted from Figure 1 and from consideration in the discussion. The complete phase chemistry dataset (Table A.3. to Table A.16.) and additional images (Figure A.1. to A.6.), in aid of the textural description, are provided in the appendix.

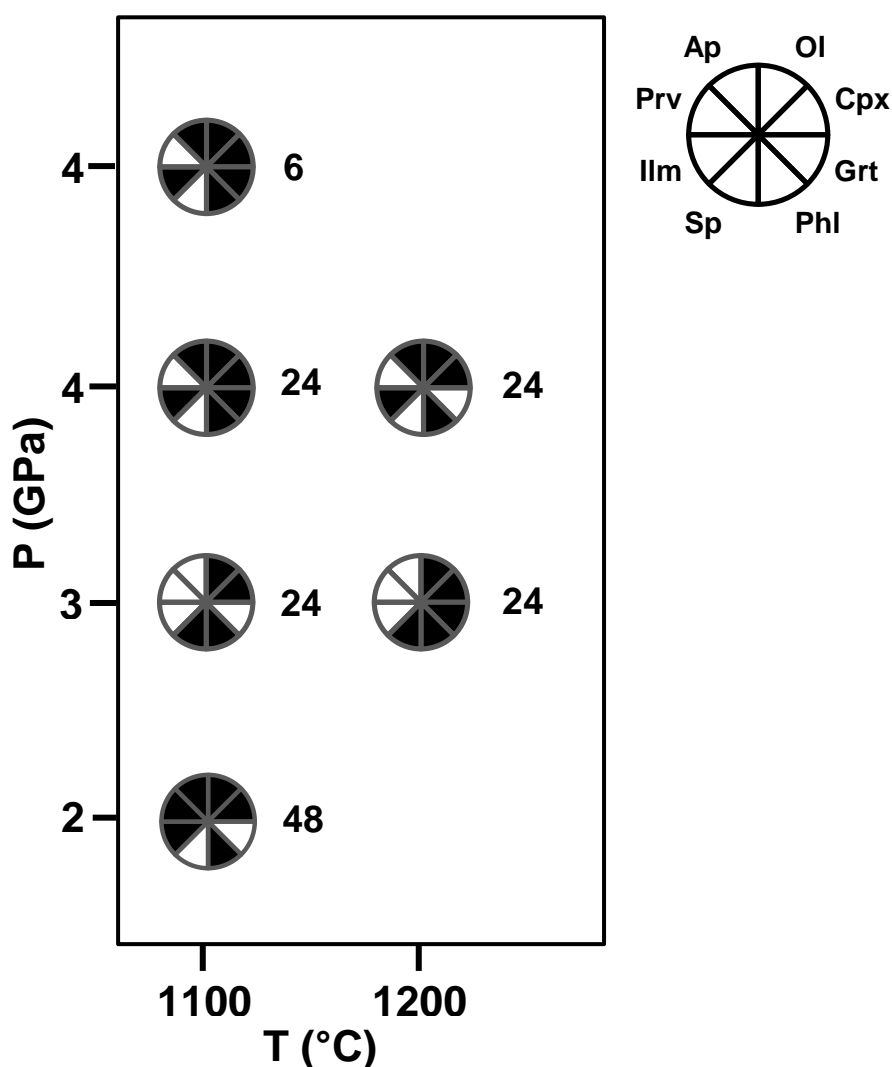


Figure 1: P-T diagram of mineral assemblages produced during the experiments. Filled wedges indicate the presence of mineral phases as shown on the legend. All runs contained melt as an additional phase. Ol = olivine; Cpx = clinopyroxene; Grt = garnet; Phl = phlogopite; Ap = apatite; Prv = perovskite; Ilm = ilmenite; Sp = spinel. Run duration is indicated by numbers given alongside the figures.

5.1. Textural description of run products

All run products consisted of mineral phases with a variable grain size distribution. A component of quench crystallisation is present in all charges often separating the melt phase from mineral phases. The quench phase displays a spinifex-like texture of very small needle shaped grains which was too narrow to analyse (Figure 2).

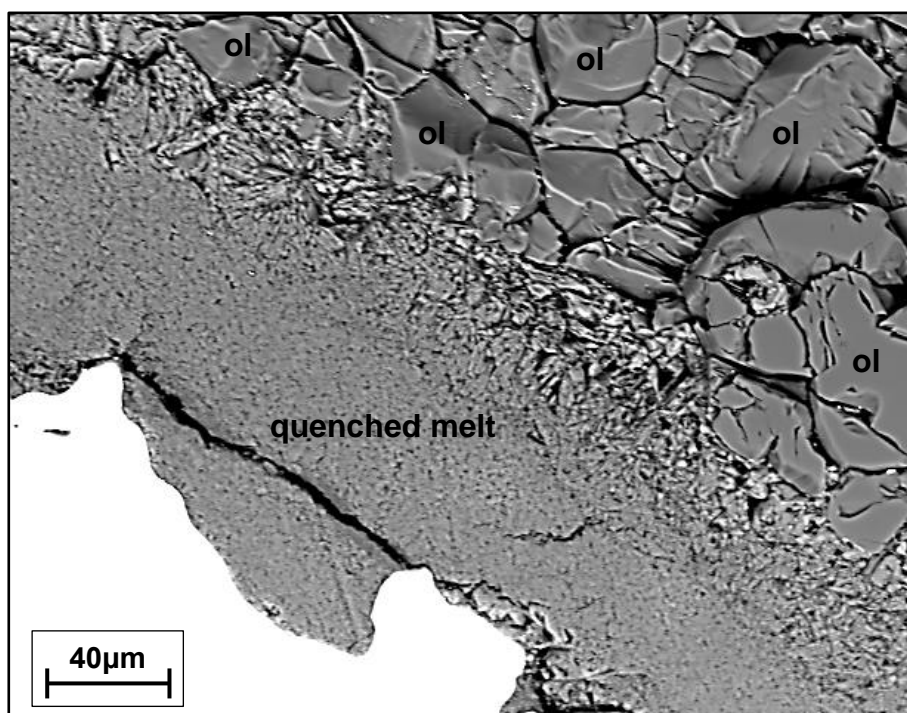


Figure 2: Back-scattered electron image of quenched melt separated from adjacent olivine by quench crystallisation with spinifex texture.

Minerals were unzoned with garnet being the exception showing pronounced zoning (Figures 4 to 6). Three well defined layers were observed in MG-01 (1100°C, 2GPa) characterised by variation in the abundance of different minerals. The first layer consisted almost entirely of olivine. The second layer is characterised by an increase in clinopyroxene abundance while the third layer predominantly consisted of phlogopite. This sample was also unique in producing perovskite. The perovskite crystals produced were located between the phlogopite-rich layer and the layer consisting of olivine plus clinopyroxene and formed discrete irregularly shaped grains enclosing small rounded grains of both olivine and clinopyroxene (Figure 3 A). Olivine crystals are characterised by variable grain size ranging from larger euhedral to subhedral grains to small rounded grains. Small, rounded clinopyroxene grains are ubiquitously found included in olivine (Figure 3 B). Individual clinopyroxene crystals occur as aggregates of small rectangular grains with rounded edges (Figure 3 F). Large subhedral to anhedral clinopyroxenes were

observed for only two experimental runs (MG-01 & MG-08; Figure 3 E). Phlogopite, apatite and ilmenite occupy various habits. The most conspicuous of phlogopite's habits is that of large interstitial pools poikilitically enclosing small grains of olivine and clinopyroxene (Figure 3 D). Phlogopite crystals also occur as small to medium sized blade-like and rectangular grains, smaller globular grains and large grains with well-defined grain edges (Figure 3 D). In most instances phlogopite crystals display characteristic cleavage (Figure 3 F). Apatite crystals occur as rounded isolated grains, lath shaped grains within the phlogopite layer of MG-01 and sometimes as larger elongated grains (Figure 3 E). Apatite and ilmenite is often found in close proximity (Figure 3 C). Ilmenite occurs as rounded grains with a pitted texture as a consequence of enclosing small grains of olivine and more seldom as lath shaped grains (Figure 3 C). Spinel crystals form only a minor component of two experiments [MG-04 (1100°C, 3GPa) & MG-05 (1200°C, 3GPa)]. In MG-04, spinel is small and irregularly shaped and completely surrounded by olivine (Figure 3 B). In MG-05, spinel is only found as very small rounded inclusions in garnet (Figure 4). When garnet crystals are present they are zoned, contain small inclusions of other phases and correspond in shape and size to the garnet xenocrysts (Figures 4 to 6). The zoning is clearly distinguishable through variation in the greyscale of garnet BSE-images (Figures 4 & 6) and X-ray element maps (Figure 5). For MG-07 (1100°C, 4GPa; Figure 6) and MG-09 (1100°C, 4 GPa, 6hours) the zoning of garnet is sharp and somewhat concentric. In MG-05 (1200°C, 3GPa) the zoning is still sharp but more pervasive across the garnet grain (Figures 4 & 5). Garnet edges are embayed by olivine and small rounded olivine inclusions are invariably found within all garnet crystals (Figures 4 & 6). Additionally the garnet in MG-05 contains small spinel inclusions (Figure 4 B) while the garnet in MG-07 contains rounded clinopyroxene inclusions (Figure 6 B). Phlogopite is present along what appears to be pre-existing fractures in the garnet found within MG-09. The mineral inclusions are all located preferentially toward the edge of the garnet crystals and within zones defined by a lighter shade of grey in the BSE-images (Figures 4 & 6).

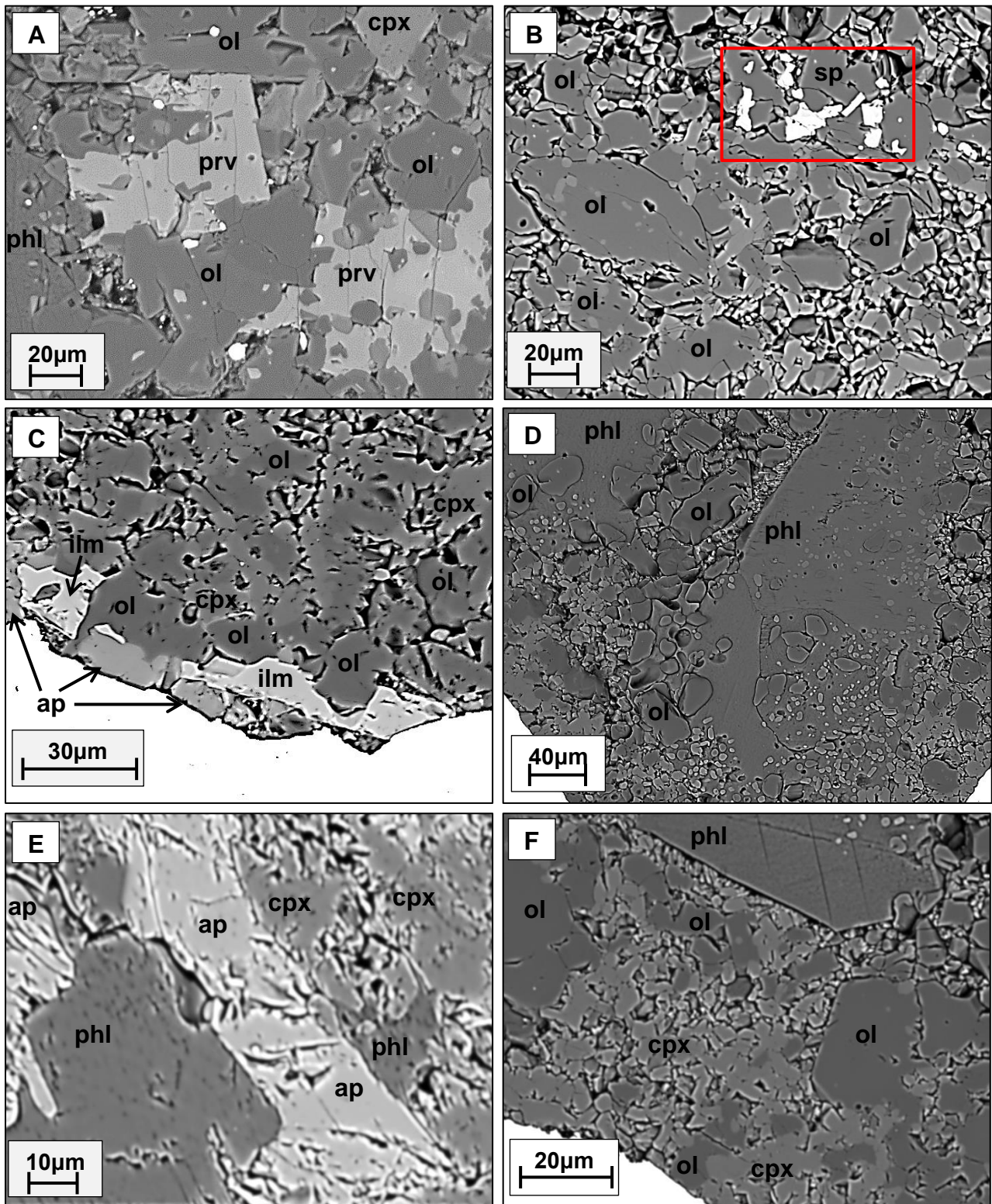


Figure 3: Back-scattered electron images showing some of the textural features produced in the experiments. A: Irregular perovskite crystals enclosing rounded grains of olivine and clinopyroxene within MG-01 (1100°C, 2GPa). The phlogopite-rich layer is located to the left of the image while the olivine plus clinopyroxene layer is located toward the right of the image. The small bright white particles are inclusions of the AgPd capsule; B: Small irregularly shaped spinel (enclosed by red rectangle) surrounded by olivine within MG-04 (1100°C, 3GPa). Also present in the image is a larger subhedral olivine with small rounded clinopyroxene inclusions. C: Lath shaped ilmenite and apatite within MG-07 (1100°C, 4GPa); D: Large interstitial pools of phlogopite enclosing small grains of olivine and clinopyroxene in MG-05 (1200°C, 3GPa); E: Elongated apatite with anhedral clinopyroxene in MG-08 (1200°C, 4GPa); F: Phlogopite with distinct cleavage and aggregates of small rectangular clinopyroxene in MG-05 (1200°C, 3GPa)

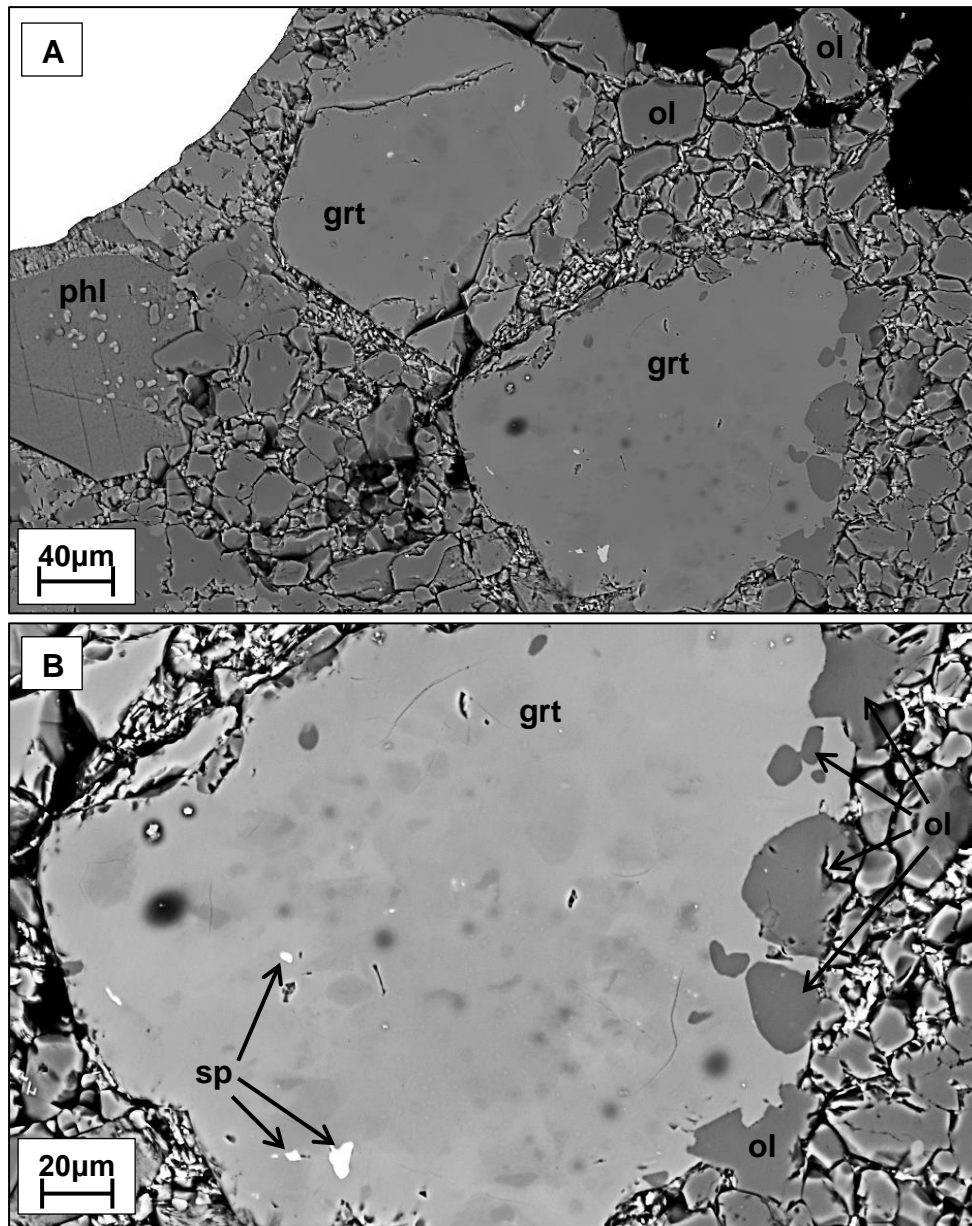


Figure 4: Back-scattered electron images showing textural characteristics of remnant garnet crystals in MG-05 (1200°C, 3GPa). Variation in grey scale across the garnet crystals defines three distinct compositional zones. Note that the lighter shade of grey is mostly confined toward the outer parts of the garnet crystals while the slightly darker grey is located toward the centre of the garnet crystals A: Overview of the remnant garnet crystals. B: Close up view of garnet in bottom right-hand corner of A. Note the location of olivine and spinel inclusions within the light grey areas of the garnet crystal. These lighter coloured areas are furthest removed in composition from the original garnet xenocrysts.

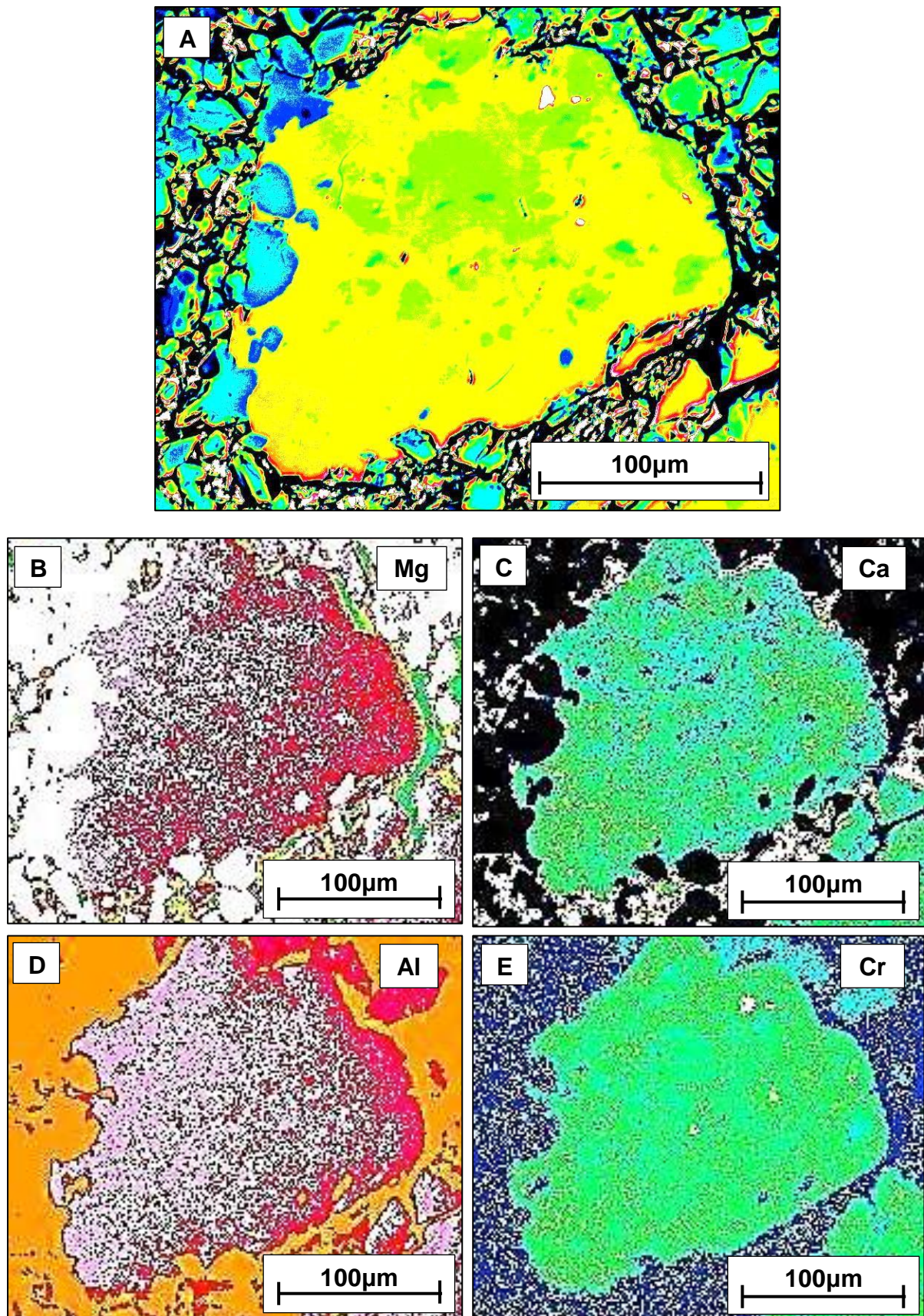


Figure 5: Compositional variation in remnant garnet crystal in MG-05 (1200°C, 3GPa). A: False coloured back-scattered electron image. B to E: X-ray element maps showing compositional zoning for B: magnesium (Mg), C: calcium (Ca), D: aluminium (Al), E: chromium (Cr). The lighter tones in colour indicate elevation in concentration for a particular element.

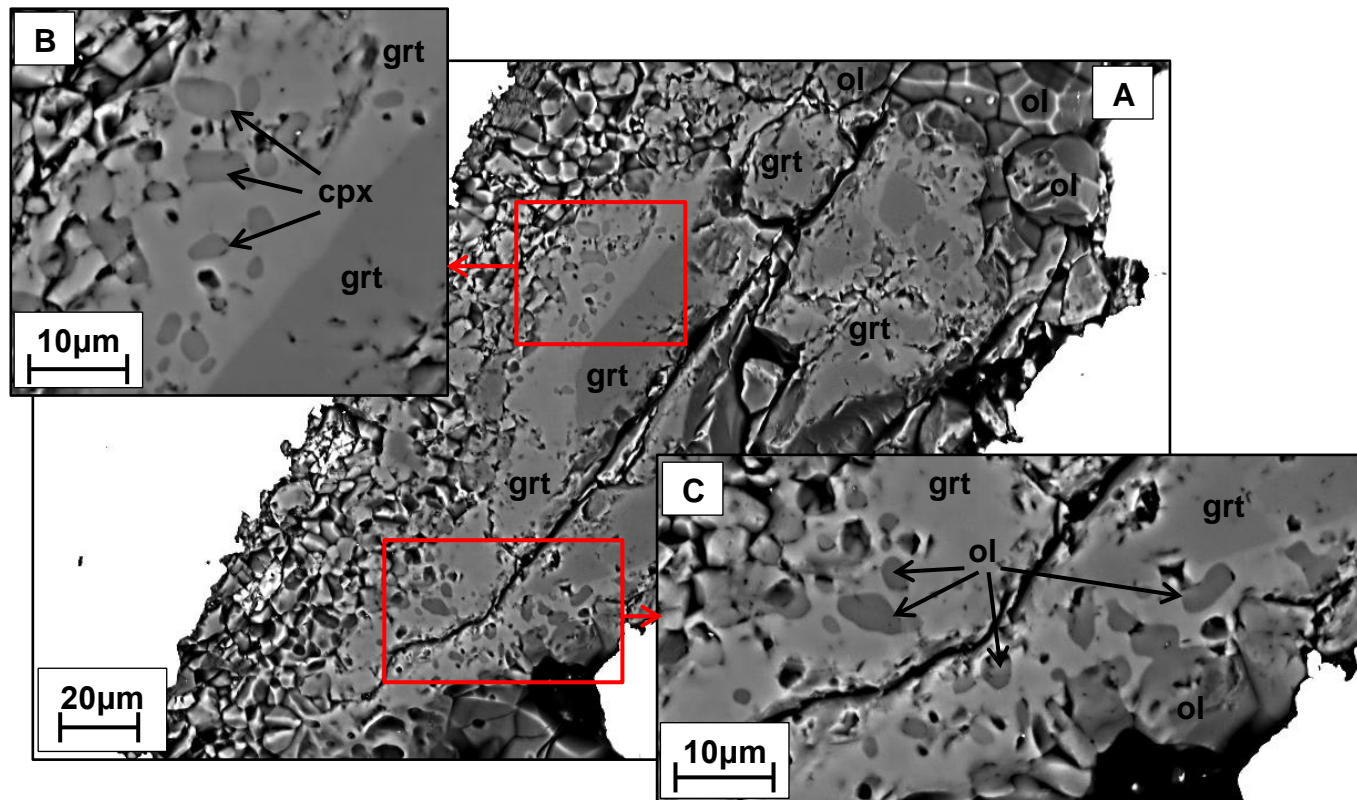


Figure 6: Back-scattered electron images showing textural characteristics of a remnant garnet crystal in MG-07 (1100°C, 4GPa). A: Overview. Note the darker shade of grey at the centre of the garnet crystal. This composition is closest in composition to the original garnet xenocrysts. Mineral inclusions are situated within the lighter grey parts toward the edge of the garnet. B: Small rounded clinopyroxene inclusions and C: small rounded olivine inclusions. Note that this garnet crystal is less pervasively zoned than the garnet crystals in MG-05 (1200°, 3GPa).

5.2. Phase Chemistry

Table 5: Representative compositions (in wt %) of olivine produced in the experiments. A: Two populations olivine were found in MG-01 (1100°C, 2GPa). The olivine with the lower average fosterite component was located in the charge where an increase in the abundance of clinopyroxene was observed. B: Representative compositions of olivine found as inclusions within garnet. Numbers in parentheses are standard deviations: 39.6 (0.3) is 39.6 ± 0.3 etc. Mineral formulae were calculated on the bases of 4 oxygens.

	A				B			B		
Exp	MG-01	MG-01	MG-04	MG-05	MG-05	MG-07	MG-07	MG-08	MG-09	
P (GPa)	2	2	3	3	3	4	4	4	4	
T (°C)	1100	1100	1100	1200	1200	1100	1100	1200	1100	
Dur (hrs)	48	48	24	24	24	24	24	24	6	
SiO ₂	39.6 (0.3)	39.4 (0.2)	40.5 (0.3)	40.7 (0.3)	40.8 (0.3)	40.1 (0.2)	40.8 (0.2)	40.6 (0.2)	39.7 (0.3)	
Cr ₂ O ₃	-	-	-	-	0.1 (0.1)	-	-	-	-	
FeO	14.7 (0.5)	16.3 (0.8)	11.5 (0.5)	11.2 (0.5)	10.0 (0.5)	12.8 (0.5)	11.0 (0.5)	11.7 (0.3)	12.1 (0.7)	
MnO	0.3 (0.1)	0.3 (0.1)	-	-	-	-	-	-	-	
MgO	44.8 (0.5)	43.6 (0.5)	47.6 (0.2)	47.8 (0.3)	48.7 (0.7)	46.9 (0.6)	48.1 (0.3)	47.6 (0.2)	47.2 (1.0)	
CaO	0.2 (0.0)	0.3 (0.1)	-	0.2 (0.1)	0.3 (0.2)	0.1 (0.1)	0.2 (0.0)	-	1.0 (0.8)	
NiO	0.2 (0.1)	0.1 (0.1)	0.3 (0.1)	0.1 (0.1)	-	-	-	-	0.1 (0.1)	
Total	99.8	100.0	100.0	100.0	99.9	99.8	100.1	99.9	100.0	
xO ²⁻	4	4	4	4	4	4	4	4	4	
Si	1.00	1.00	1.00	1.00	1.00	1.00	1.00	1.00	0.99	
Cr	-	-	-	-	0.00	-	-	-	-	
Fe ²⁺	0.31	0.34	0.24	0.23	0.20	0.27	0.23	0.24	0.25	
Mn	0.01	0.01	-	-	-	-	-	-	-	
Mg	1.68	1.64	1.75	1.76	1.78	1.74	1.76	1.75	1.75	
Ca	0.01	0.01	-	0.00	0.01	0.00	0.00	-	0.03	
Ni	0.00	0.00	0.01	0.00	-	0.00	-	-	0.00	
ΣCations	3.00	3.00	3.00	3.00	2.99	3.00	2.99	3.00	3.01	
Mg#	84	83	88	88	90	87	89	88	87	

Table 6: Representative compositions (in wt %) of clinopyroxene produced in the experiments. A: Representative composition of clinopyroxene found as inclusions within garnet. Numbers in parentheses are standard deviations: 49.8 (1.7) is 49.8 ± 1.7 etc. Mineral formulae were calculated on the bases of 6 oxygens, with Fe³⁺ calculated according to Droop (1987). b/d = below detection

	A						
	MG-01	MG-04	MG-05	MG-07	MG-07	MG-08	MG-09
Exp							
P (GPa)	2	3	3	4	4	4	4
T (C)	1100	1100	1200	1100	1100	1200	1100
Dur (hrs)	48	24	24	24	24	24	6
SiO ₂	49.8 (1.7)	53.6 (0.4)	52.6 (0.4)	53.7 (0.3)	52.2 (1.3)	53.5 (0.4)	52.6
TiO ₂	1.2 (0.5)	0.4 (0.1)	0.5 (0.1)	0.3 (0.1)	0.7 (0.2)	0.3 (0.0)	0.4
Al ₂ O ₃	6.4 (1.6)	1.6 (0.4)	3.2 (0.3)	1.6 (0.2)	4.5 (2.0)	2.1 (0.1)	2.4
Cr ₂ O ₃	0.8 (0.5)	0.7 (0.2)	0.7 (0.1)	0.5 (0.1)	0.9 (0.3)	0.9 (0.1)	0.5
Fe ₂ O ₃	-	-	0.1 (0.1)	0.2 (0.2)	-	-	-
FeO	4.1 (0.5)	3.6 (0.5)	3.0 (0.1)	3.4 (0.1)	3.7 (0.6)	3.1 (0.1)	3.0
MnO	0.3 (0.2)	-	0.1 (0.1)	-	-	b/d	-
MgO	16.5 (1.5)	18.0 (0.4)	17.5 (0.6)	18.0 (0.5)	17.7 (0.4)	17.5 (0.5)	18.7
CaO	20.9 (2.7)	22.2 (0.9)	22.4 (0.6)	22.4 (0.7)	20.3 (1.8)	22.3 (0.6)	22.9
Na ₂ O	-	-	0.1 (0.1)	-	b/d	0.2 (0.0)	-
Total	99.9	100.1	100.1	100.0	100.0	100.0	100.5
xO ²⁻	6	6	6	6	6	6	6
Si	1.81	1.95	1.91	1.95	1.89	1.95	1.91
Ti	0.03	0.01	0.01	0.01	0.02	0.01	0.01
Al	0.27	-	0.13	0.07	0.19	0.09	0.10
Cr	0.02	0.02	0.02	0.01	0.02	0.03	0.02
Fe ³⁺	-	-	0.00	0.01	-	-	-
Fe ²⁺	0.13	0.11	0.09	0.10	0.11	0.09	0.09
Mn	0.01	-	0.00	-	-	-	-
Mg	0.90	0.98	0.95	0.97	0.96	0.94	1.01
Ca	0.82	0.87	0.87	0.87	0.79	0.87	0.89
Na	-	-	0.01	-	-	0.01	-
ΣCations	3.99	4.00	4.00	4.00	3.99	3.99	4.02
Mg#	88	90	91	90	89	91	92

Table 7: Representative compositions (in wt %) of phlogopite produced in the experiments. Numbers in parentheses are standard deviations: 38.6 (0.4) is 38.6 ± 0.4 etc. Mineral formulae were calculated on the bases of 24 oxygens (Σ O, OH, F, Cl). b/d = below detection

Exp	MG-01	MG-04	MG-05	MG-07	MG-08	MG-09
P(GPa)	2	3	3	4	4	4
T(°C)	1100	1100	1200	1100	1200	1100
Dur(hrs)	48	24	24	24	24	6
SiO ₂	38.6 (0.4)	40.2 (0.7)	39.5 (0.4)	40.8 (0.4)	40.5 (0.4)	39.3 (0.4)
TiO ₂	1.3 (0.1)	1.8 (0.3)	2.1 (0.3)	1.1 (0.1)	1.5 (0.1)	1.0 (0.2)
Al ₂ O ₃	17.6 (0.1)	14.3 (0.4)	15.5 (0.4)	13.8 (0.3)	14.1 (0.1)	13.9 (1.5)
Cr ₂ O ₃	-	1.1 (0.1)	1.3 (0.2)	0.7 (0.1)	0.9 (0.2)	0.3 (0.3)
FeO	5.9 (0.2)	4.1 (0.1)	3.8 (0.2)	4.1 (0.1)	4.1 (0.2)	4.5 (0.6)
MgO	22.1 (0.1)	22.8 (0.4)	22.4 (0.3)	23.2 (0.3)	23.1 (0.3)	24.6 (0.5)
CaO	0.1 (0.1)	-	-	b/d	0.1 (0.1)	0.5 (0.4)
Na ₂ O	0.3 (0.0)	-	-	0.3 (0.1)	-	b/d
K ₂ O	9.6 (0.1)	10.3 (0.1)	10.1 (0.1)	9.9 (0.4)	10.2 (0.3)	9.4 (0.3)
F	1.3 (0.4)	0.9 (0.5)	1.5 (0.2)	1.4 (0.2)	1.3 (0.1)	2.1 (0.2)
Total	96.0	95.1	95.5	95.3	95.3	94.8
xO ²⁻	24	24	24	24	24	24
Si	5.88	6.34	5.78	6.28	6.17	6.22
Ti	0.14	0.21	0.23	0.13	0.17	0.12
Al	3.17	2.67	2.67	2.51	2.53	2.59
Cr	-	0.14	0.15	0.08	0.11	0.04
Fe ²⁺	0.75	0.54	0.46	0.53	0.53	0.60
Mg	5.02	5.36	4.87	5.32	5.24	5.81
Ca	0.02	-	-	0.11	0.02	0.08
Na	0.07	-	-	0.08	-	0.01
K	1.86	2.06	1.89	1.94	1.97	1.91
F	0.61	0.44	0.68	0.70	0.62	1.07
Σ Cations	17.52	17.76	16.73	17.69	17.35	18.45
Mg#	87	91	91	91	91	91

Table 8: Representative compositions (in wt %) of remnant garnet crystals present in the experiments. 1: garnet composition furthest removed from garnet xenocryst composition in MG-05; 2: intermediary garnet composition in MG-05; 3: garnet composition closest to garnet xenocryst composition in MG-05; 4: garnet composition furthest removed from garnet xenocryst composition in MG-07; 5: garnet composition closest to garnet xenocryst composition in MG-07; 6: garnet composition furthest removed from garnet xenocryst composition in MG-09; 7: garnet composition closest to garnet xenocryst composition in MG-09. Numbers in parentheses are standard deviations: 41.1 (0.2) is 41.1 ± 0.2 etc. Mineral formulae were calculated on the bases of 12 oxygens, with Fe^{3+} calculated according to Droop (1987). Site occupancy is based on the ideal unit formula of garnet ($\text{X}_3\text{Y}_2\text{Z}_3\text{O}_{12}$) as given in Deer, Howie & Zussman (1992). XPy, XGrss and XAlm were calculated as defined by Deer, Howie & Zussman (1992). b/d = below detection

	1	2	3	4	5
Exp	MG-05	MG-05	MG-05	MG-07	MG-07
P(GPa)	3	3	3	4	4
T(°C)	1200	1200	1200	1100	1100
Dur(hrs)	24	24	24	24	24
SiO ₂	41.1 (0.2)	41.6 (0.2)	42.0 (0.3)	40.8 (0.1)	42.0 (0.3)
TiO ₂	1.0 (0.1)	0.7 (0.1)	0.4 (0.1)	1.4 (0.2)	0.5 (0.1)
Al ₂ O ₃	20.0 (0.3)	21.2 (0.3)	21.3 (0.2)	20.4 (0.2)	21.4 (0.1)
Cr ₂ O ₃	4.0 (0.2)	3.0 (0.3)	3.2 (0.2)	3.2 (0.3)	3.2 (0.1)
Fe ₂ O ₃	b/d	-	b/d	-	b/d
FeO	7.6 (0.2)	7.7 (0.1)	7.5 (0.4)	8.5 (0.3)	7.4 (0.2)
MnO	0.5 (0.1)	0.4 (0.1)	0.3 (0.0)	0.4 (0.1)	0.3 (0.1)
MgO	17.0 (0.5)	18.2 (0.2)	19.7 (0.3)	16.7 (0.4)	20.3 (0.2)
CaO	8.9 (0.6)	7.3 (0.1)	5.8 (0.1)	8.6 (0.4)	5.0 (0.2)
Total	100.1	100.0	100.4	99.9	100.12
xO ²⁻	12	12	12	12	12
Si	2.98	2.99	2.99	2.97	2.99
Al	0.02	0.01	0.01	0.03	0.01
ZO ₄ Tetrahedra	3.00	3.00	3.00	3.00	3.00
Ti	0.05	0.04	0.02	0.08	0.02
Al	1.69	1.78	1.78	1.72	1.79
Cr	0.23	0.17	0.18	0.18	0.18
Fe ³⁺	0.00	-	0.01	-	0.00
YO ₆ Octahedra	1.98	1.99	2.00	1.97	2.00
Fe ²⁺	0.46	0.46	0.44	0.51	0.44
Mn	0.03	0.03	0.02	0.03	0.02
Mg	1.84	1.95	2.10	1.81	2.16
Ca	0.69	0.56	0.44	0.67	0.38
X-ions	3.02	3.00	3.00	3.02	3.00
ΣCations	7.99	7.99	8.00	7.99	7.99
Mg#	80	81	83	78	83
XPy	60.81	65.09	69.86	59.99	71.91
XGrss	11.22	10.02	5.15	12.87	3.79
XAlm	15.26	15.37	14.72	17.05	14.61

Table 8 continued

	6	7
Exp	MG-09	MG-09
P (GPa)	4	4
T (°C)	1100	1100
Dur (hrs)	6	6
SiO ₂	39.7 (0.3)	41.9 (0.1)
TiO ₂	2.4 (0.5)	0.1 (0.1)
Al ₂ O ₃	17.8 (0.7)	22.0 (0.4)
Cr ₂ O ₃	3.9 (0.3)	2.7 (0.1)
Fe ₂ O ₃	b/d	1.1 (0.1)
FeO	7.5 (0.2)	5.8 (0.3)
MnO	0.4 (0.2)	0.3 (0.1)
MgO	9.6 (0.7)	21.4 (0.3)
CaO	19.1 (1.2)	4.7 (0.1)
Total	100.3	100.0
xO ²⁻	12	12
Si	2.97	2.97
Al	0.03	0.02
ZO ₄ Tetrahedra	3.00	2.98
Ti	0.13	0.01
Al	1.54	1.83
Cr	0.23	0.15
Fe ³⁺	0.00	0.06
YO ₆ Octahedra	1.91	2.04
Fe ²⁺	0.47	0.34
Mn	0.02	0.02
Mg	1.07	2.26
Ca	1.53	0.36
X-ions	3.09	2.98
ΣCations	8.00	8.00
Mg#	69	87
XPy	34.48	75.89
XGrss	37.40	1.78
XAlm	15.16	11.47

Table 9: Representative compositions of apatite produced in the experiments (in wt %). Numbers in parentheses are standard deviations: 0.4 (0.14) is 0.4 ± 0.1 etc. Mineral formulae were calculated on the bases of 25 oxygens (ΣO , OH, F, Cl).

Exp	MG-01	MG-07	MG-08	MG-09
P(GPa)	2	4	4	4
T(°C)	1100	1100	1200	1100
Dur(hrs)	48	24	24	24
SiO ₂	-	-	-	0.6 (0.1)
FeO	0.4 (0.1)	0.6 (0.1)	0.5 (0.1)	0.2 (0.1)
MgO	0.1 (0.1)	1.0 (0.1)	1.3 (0.1)	0.2 (0.2)
CaO	53.6 (0.4)	52.8 (0.4)	52.9 (0.7)	53.0 (0.2)
SrO	2.4 (0.4)	1.2 (0.2)	1.2 (0.1)	2.8 (0.3)
P ₂ O ₅	41.8 (0.2)	42.7 (0.2)	42.3 (0.7)	41.1 (0.4)
F	2.3 (0.2)	2.1 (0.3)	2.0 (0.6)	2.8 (0.4)
Total	99.6	99.4	99.36	99.44
xO ²⁻	25	25	25	25
Si	-	-	-	0.10
Fe ²⁺	0.05	0.07	0.07	0.03
Mg	0.02	0.24	0.31	0.05
Ca	9.48	8.99	9.07	9.04
Sr	0.23	0.11	0.11	0.25
P	5.85	5.75	5.72	5.54
F	1.17	1.07	1.00	1.40
Σ Cations	16.81	16.23	16.28	16.41

Table 10: Representative compositions (in wt %) of spinel, ilmenite and perovskite produced in the experiments. A: Representative composition of spinel found as inclusions in garnet. Numbers in parentheses are standard deviations: 1.7 (0.7) is 1.7 ± 0.7 etc. Mineral formulae were calculated on the bases of 4 oxygens for spinel and on the bases of 3 oxygens for ilmenite and perovskite. Fe³⁺ calculated according to Droop (1987). b/d = below detection

	A								
	Sp	Sp		Ilm	Ilm	Ilm	Ilm		Prv
Exp	MG-04	MG-05		MG-01	MG-07	MG-08	MG-09		MG-01
P (Gpa)	3	3		2	4	4	4		2
T (°C)	1100	1300		1100	1100	1200	1100		1100
Dur (hrs)	24	24		48	24	24	6		48
SiO ₂	1.7 (0.7)	1.7 (0.4)	TiO ₂	52.3 (0.8)	52.0 (0.5)	53.5 (0.4)	53.6 (0.3)	TiO ₂	56.4 (0.3)
TiO ₂	2.7 (0.2)	1.9 (0.0)	Al ₂ O ₃	0.3 (0.1)	1.0 (0.2)	0.7 (0.1)	0.6 (0.1)	Al ₂ O ₃	0.4 (0.0)
Al ₂ O ₃	20.5 (3.3)	29.6 (0.5)	Cr ₂ O ₃	0.6 (0.2)	1.77 (0.10)	1.5 (0.3)	1.4 (0.1)	Nb ₂ O ₅	0.8 (0.2)
Cr ₂ O ₃	40.6 (1.6)	34.0 (0.2)	Nb ₂ O ₅	b/d	-	-	b/d	FeO	0.8 (0.1)
Fe ₂ O ₃	2.7 (0.8)	1.7 (0.5)	V ₂ O ₃	1.2 (0.2)	1.9 (0.4)	1.3 (0.5)	0.9 (0.5)	CaO	39.9 (0.3)
FeO	16.7 (0.8)	13.1 (0.2)	FeO	32.0 (0.4)	27.2 (0.2)	27.1 (0.1)	29.3 (0.2)	Total	98.29
MnO	0.4 (0.1)	-	MnO	0.6 (0.1)	0.4 (0.1)	0.4 (0.1)	0.5 (0.0)		
MgO	14.8 (0.6)	17.6 (0.1)	MgO	9.8 (0.3)	13.9 (0.4)	14.2 (0.2)	12.2 (0.2)		
CaO	-	0.5 (0.0)	CaO	1.5 (0.6)	-	-	0.3 (0.3)	xO ²⁻	3
Total	100.2	100.0	Total	98.6	98.2	98.7	98.8	Ti	0.99
xO ²⁻	4	4	xO ²⁻	3	3	3	3	Al	0.01
Si	0.05	0.05	Ti	0.98	0.96	0.98	0.98	Nb	0.01
Ti	0.06	0.04	Al	0.01	0.03	0.02	0.02	Fe ²⁺	0.02
Al	0.73	1.01	Cr	0.01	0.03	0.03	0.03	Ca	0.99
Cr	0.98	0.78	Nb	0.00	-	-	b/d	ΣCations	2.01
Fe ³⁺	0.06	0.04	V	0.02	0.03	0.02	0.02		
Fe ²⁺	0.43	0.32	Fe ²⁺	0.67	0.56	0.56	0.60		
Mn	0.01	0.00	Mn	0.02	0.01	0.01	0.02		
Mg	0.67	0.76	Mg	0.26	0.36	0.37	0.32		
Ca	-	0.02	Ca	0.02	-	-	0.00		
ΣCations	3.00	3.00	ΣCations	2.00	2.00	1.99	1.98		
Mg#	61	71		28	39	40	34		

Table 11: Representative compositions (in wt %; normalised to 100% anhydrous) of quenched melts produced in the experiments. Numbers in parentheses are standard deviations: 17.9 (0.3) is 17.9 ± 0.3 etc. b/d = below detection

Exp	MG-01	MG-04	MG-05	MG-07	MG-08	MG-09
P(Gpa)	2	3	3	4	4	4
T(°C)	1100	1100	1200	1100	1200	1100
Dur(hrs)	48	24	24	24	24	6
SiO ₂	17.9 (0.3)	17.9 (0.3)	21.9 (0.3)	15.2 (1.5)	21.0 (0.4)	31.5 (2.5)
TiO ₂	1.9 (0.2)	4.5 (0.2)	4.3 (0.1)	3.6 (0.5)	4.2 (0.2)	3.6 (0.7)
Al ₂ O ₃	6.4 (0.6)	4.4 (0.2)	5.2 (0.2)	4.5 (0.7)	4.6 (0.2)	11.4 (4.2)
Cr ₂ O ₃	-	b/d	0.1 (0.1)	b/d	b/d	b/d
FeO	11.6 (1.6)	9.3 (0.5)	8.5 (0.2)	9.5 (0.7)	10.92 (0.6)	13.0 (1.4)
MnO	0.3 (0.1)	0.2 (0.2)	0.2 (0.1)	0.4 (0.2)	0.2 (0.1)	b/d
MgO	18.1 (1.1)	20.0 (0.6)	20.3 (0.4)	22.7 (1.1)	20.5 (0.6)	16.7 (2.4)
CaO	37.1 (1.6)	27.9 (0.4)	22.6 (0.7)	31.3 (1.6)	24.5 (0.7)	13.2 (2.8)
Na ₂ O	0.8 (0.1)	0.6 (0.1)	0.5 (0.1)	0.4 (0.2)	0.2 (0.2)	0.8 (0.3)
K ₂ O	0.4 (0.2)	1.6 (0.2)	1.5 (0.1)	1.4 (0.4)	1.4 (0.3)	5.3 (2.2)
P ₂ O ₅	2.9 (0.5)	12.3 (0.6)	13.1 (0.4)	8.6 (1.0)	10.3 (0.5)	2.9 (1.5)
F ⁻	4.2 (0.7)	2.0 (1.1)	2.8 (0.6)	3.9 (1.7)	2.7 (0.6)	2.0 (0.3)
Cl ⁻	0.2 (0.1)	0.1 (0.1)	0.1 (0.1)	0.2 (0.1)	0.5 (0.1)	0.4 (0.1)
Mg#	74	79	81	81	77	69
SiO ₂ +Al ₂ O ₃ (wt %)	24.3	22.3	27.1	19.7	25.6	42.9
Mg/Ca (mol)	0.68	0.99	1.25	1.01	1.17	1.76

5.2.1. Olivine

Olivine produced in the experiments display variable Mg# ranging between 83 and 90 and is consistently lower than the Mg# reported for olivine (Mg# = 93) of the kimberlite starting material. MG-01 (1100°C, 2GPa) produced two populations of olivine having an average Mg# of 84 and 83 respectively; the olivine with the lower average fosterite component being present where an increase in pyroxene abundance was noted in the charge. Furthermore, compared to olivine (average Mg# of 88) produced in the remainder of the experiments the olivine produced in MG-01 has the lowest Mg#. These variations in Mg# do not show any meaningful correlation to changes in the PT conditions, but they do reflect changes in the proportion and composition of other phases. When the size of olivine found as inclusions within garnet permitted reliable microprobe analysis, it was found that the included olivine had a slightly higher Mg# than was measured for the olivine in the remainder of the charge [MG-05 (1200°C, 3GPa) and MG-07 (1100°C, 4GPa)]. Trace amounts of Al₂O₃ were detected for some of the olivine grains included in garnet. CaO and MnO are present in the majority of olivine analysed. When NiO was detected, the concentration was low (≤ 0.3 wt %).

5.2.2. Clinopyroxene

Clinopyroxenes produced in the experiments can be described as Cr-diopside with a Mg# that varies between 88 and 92. Noteworthy is the fairly high but variable Al₂O₃ content of the pyroxenes (1.6 - 6.4 wt %). The highest average Al₂O₃ content measured is for clinopyroxene of MG-01 (6.4wt% Al₂O₃) and the clinopyroxene grains included in garnet of MG-07 (4.2 wt % Al₂O₃). The clinopyroxenes of MG-01 and clinopyroxene grains included in garnet of MG-07 are also similar in having lower Mg#, SiO₂ and CaO content and higher TiO₂ content compared to the clinopyroxenes produced in the remainder of the charges. The cation totals of clinopyroxene never significantly exceeded ideal. Consequently, Fe₂O₃ contents are considered negligible. Clinopyroxene chemistry does not vary as a simple function of P and T, but varies in response to changes and abundance of other phases.

5.2.3. Phlogopite

Phlogopite produced in the bulk of the experiments has a fairly consistent chemistry with an average Mg# of 91. Similar to olivine and clinopyroxene, phlogopite produced in MG-01 has a lower Mg# (average of 87). The phlogopite of MG-01 is also marked

by the absence of Cr_2O_3 and higher Al_2O_3 content compared to phlogopite produced in the remainder of the experiments. The MgO content of phlogopite increases marginally with increasing P while Al_2O_3 content decreases. At constant P, Al_2O_3 content increases with T. For MG-04 (1100°C, 3GPa), MG-05 (1200°C, 3GPa), MG-07(1100°C, 4GPa) and MG-08 (1200°C, 4GPa) slight temperature dependence is seen for the concentrations of SiO_2 , TiO_2 and Cr_2O_3 : at constant pressure, SiO_2 content decreases while TiO_2 and Cr_2O_3 contents increases with temperature. Fluorine (0.9 - 2.3 wt %) was detected in all phlogopite analysed.

5.2.4. Garnet

Garnet crystals are present in MG-05 (1200°C, 3GPa, 24 hours), MG-07 (1100°C, 4GPa, 24 hours) and MG-09 (1100°C, 4GPa, 6 hours) and shows prominent compositional zoning for Ca, Mg, Al, Cr and Ti. The garnet crystals found within MG-05 have three distinct compositional zones which appear to be converging toward a single composition (Figures 7 and 8 A & B). A composition located more towards the centre of the garnet crystals is comparable in composition to the garnet xenocrysts. Compared to the garnet xenocrysts, the composition located toward the centre of the garnet crystals in MG-05, is shifted very slightly to a more grossular-rich composition (Figure 8 A & B). The composition located preferentially toward the edge of the garnet crystals, differs markedly in composition from the garnet xenocrysts and is defined by increases in Ca, Cr and Ti while a decrease is seen for Mg and Al. In contrast to the garnet crystals in MG-05, garnet crystals found in MG-07 and MG-09 only have two compositional zones. A slight increase in the magnitude of the compositional variation between the rim and core compositions of garnet in MG-07 is seen compared to MG-05. However, the pattern of the compositional zonation in the garnet crystals between these experiments is comparable (Figure 7 and 8). An extreme variation between the rim and core compositions is seen for the garnet crystals in MG-09 (Figures 7 and 8 A & D). Additionally, the core composition of the garnet crystals in MG-09 is shifted slightly to a more pyrope-rich composition (Figure 8 A & B) compared to the garnet crystals in MG-05 and MG-07. Atomic proportion plots of Si versus Ti (Figure 7 A) and (Al + Cr) versus Ti (Figure 7 B) reveal a negative correlation between (Al + Cr) and Ti while no clear relationship is observed for Ti and Si. This indicates the preferential incorporation of Ti into the octahedral sites of the garnet structure. A ternary plot of the proportions pyrope, almandine and grossular of the compositional zones show that noteworthy variation in the grossular and pyrope components of the core and rim compositions are present; the grossular component increases in the rim composition while the pyrope component decreases (Figure 8). A less significant variation in the

almandine component is seen (Figure 8). This indicates that Ca/Mg exchange predominates over Fe/Mg exchange. These features are a consequence of the reaction of garnet since the zoning and inclusions were absent from the xenocrystic garnet as determined by BSE images and X-ray element maps.

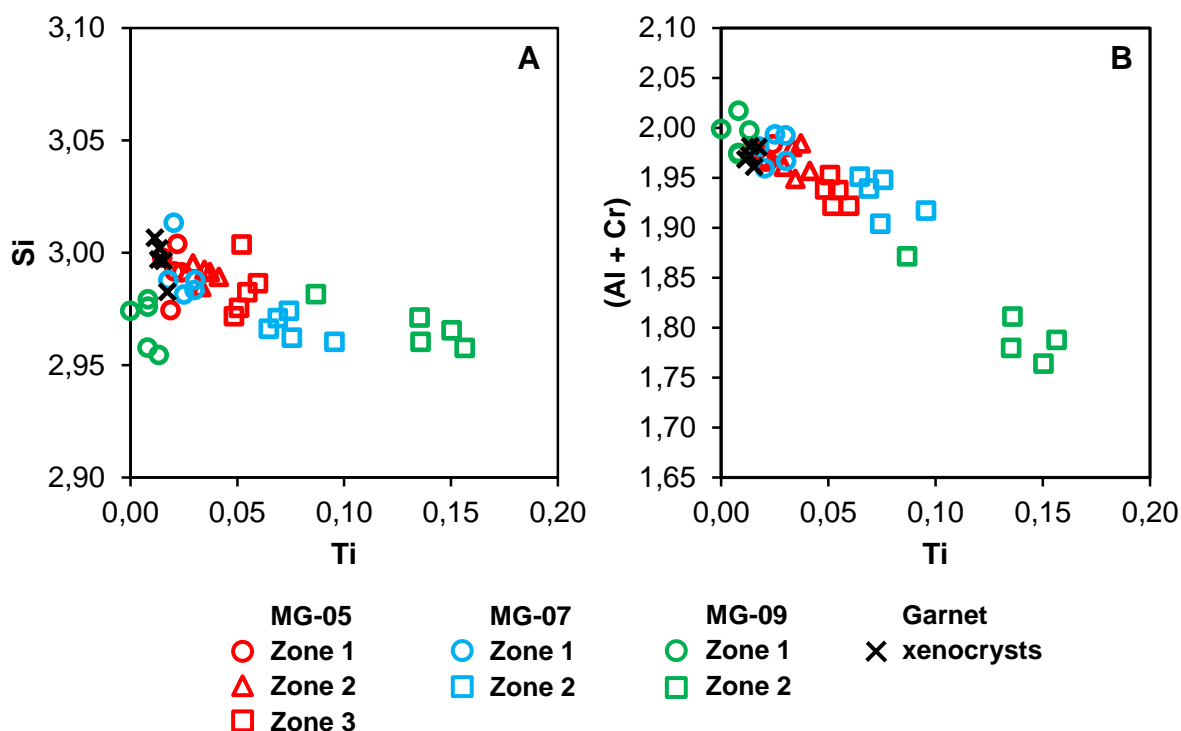


Figure 7: Garnet compositions. Atomic proportion plots of A: Si versus Ti and B: (Al + Cr) versus Ti. Si remains near constant as Ti increases compared to a decrease in (Al + Cr) as Ti increases. This suggests a predominately six-fold co-ordination of Ti within the garnet structure. Colour represent garnet compositions from individual experiments [red = MG-05 (1200°C, 3GPa, 24 hours); blue = MG-07 (1100°C, 4GPa, 24 hours); green = MG-09 (1100°C, 4GPa, 6hours)]. Shapes correspond to different compositional zones within single garnet crystals (circle = composition most similar to xenocrystic garnet; triangle = intermediary composition; square = composition furthest removed from xenocrystic garnet composition). For reference, the composition of the xenocrystic garnet (black X) is included in the plots.

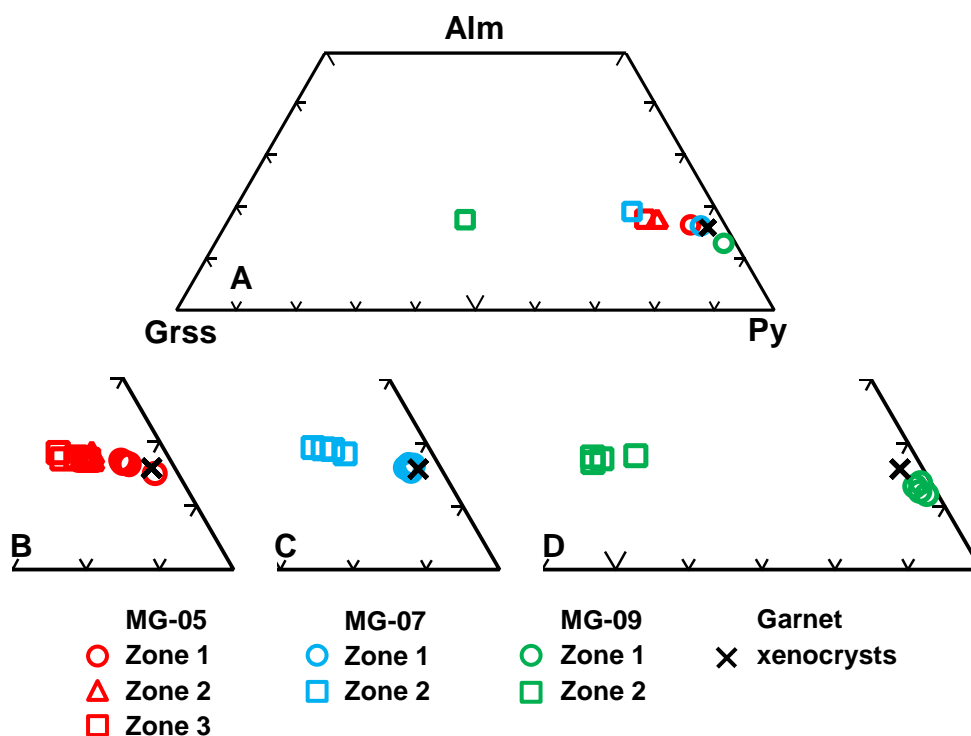


Figure 8: Garnet compositions. A: Ternary plot showing the variation of the proportions pyrope, almandine and grossular between the different compositional zones of the remnant garnet crystals. Each point in A represents the average of the points plotted in B, C and D where B = MG-05 (1200°C, 3GPa, 24 hours); C = MG-07 (1100°C, 4GPa, 24 hours) and D = MG-09 (1100°C, 4GPa, 6hours). A large increase is seen in the grossular component of the rim compositions with a corresponding decrease in the pyrope component. A less significant variation is seen in the almandine component. This indicates that Ca/Mg exchange dominates over Fe/Mg exchange within the garnet rim compositions. Py = pyrope; Alm = almandine and Grss = grossular.

5.2.5. Apatite

Apatite was produced in MG-01 (1100°C, 2GPa), MG-07 (1100°C, 4GPa), MG-08 (1100°C, 4GPa) and MG-09 (1100°C, 4GPa, 6hours) and can be described as fluorapatite (2.0 - 2.8 wt % F). As with phlogopite, the apatite crystals have a fairly similar chemistry across all experiments. P₂O₅ and MgO concentrations increase very slightly with increasing pressure accompanied by a decrease in CaO. This observation does not hold true for MG-09. SrO (1.2 - 2.8 wt %) was measured for all apatite. It should be noted that only a very weak negative correlation is seen between the CaO and SrO contents of the apatites produced

5.2.6. Ilmenite

Ilmenite produced in the experimental runs can be described as magnesian ilmenite. The ilmenites contain appreciable amounts of Cr₂O₃ (0.5 – 1.9 wt %) and MnO (0.3 - 0.7 wt %). V₂O₃ was detected in all ilmenites and Nb₂O₃ was detected in

the ilmenite produced in MG-01 (1100°C, 2 GPa, 48 hours) and MG-09 (1100°C, 4GPa, 6 hours). An increase in the MgO, Cr₂O₃, Al₂O₃ and V₂O₃ content with a corresponding decrease in FeO and MnO content is observed with an increase in pressure. At constant pressure a degree of temperature dependence is observed for some elements: increasing TiO and MgO content and decreasing Al₂O₃, Cr₂O₃ and V₂O₃ content with increased temperature.

5.2.7. *Spinel*

Spinel was only produced in experiments that were devoid of ilmenite and apatite [MG-04 (1100°C, 3GPa) and MG-05 (1200°C, 3GPa)]. The composition of the spinel can be described as magnesiochromite. Spinel produced in MG-05 is only present as crystals included in garnet. The spinels included in garnet have higher concentrations of MgO and Al₂O₃ with lower concentrations of FeO and Cr₂O₃ compared to the spinel produced in MG-04. The calculated Fe³⁺ content of spinels is elevated compared to other mineral phases produced during the same and different experiments. The average Fe³⁺ content of the spinel crystals in MG-04 is 2.7 wt % compared to an average Fe³⁺ content of 1.7 wt % for the spinels included in garnet of MG-05. The variation in the Fe³⁺ content is to be expected due to partitioning of Fe³⁺ between the phases involved.

5.2.8. *Perovskite*

The perovskite produced in MG-01 (1100°C, 2GPa) is Ca and Ti-rich, low in Fe and contain a substantial niobium component (0.56 - 1.05 wt % Nb₂O₅).

5.2.9. *Melt*

The composition of melts produced is shown on plots of selected major elements (Figure 9). Compared to geochemically determined estimates of primary kimberlite melts, the majority of melts produced in this study have significantly lower concentrations of SiO₂, MgO and Cr₂O₃ while concentrations of CaO, Al₂O₃ and P₂O₅ are higher. The composition of the melt produced in MG-09 (1100°C, 4GPa, 6hours) deviates from this observation. The melt produced in MG-09 has elevated concentrations of SiO₂ and Al₂O₃ and a lower CaO content when compared to an experiment performed at the same PT conditions but at a longer duration [MG-07 (1100°C, 4GPa, 24hours)]. Not considering MG-09, some notable correlations are seen for melt composition and experimental temperature. The concentrations of SiO₂ and Cr₂O₃ increase with increasing temperature and the concentration of CaO

decreases. An inverse relationship is seen for the concentration CaO and P₂O₅. At 1100°C, MgO is positively correlated to pressure.

Micro-Raman spectroscopic analyses of the melts produced in the experiments confirmed the presence of CO₃²⁻ in the melts produced for three samples [MG-01 (1100°C, 3GPa), MG-04 (1100°C, 4GPa) and MG-08 (1200°C, 4GPa); Figure 10].

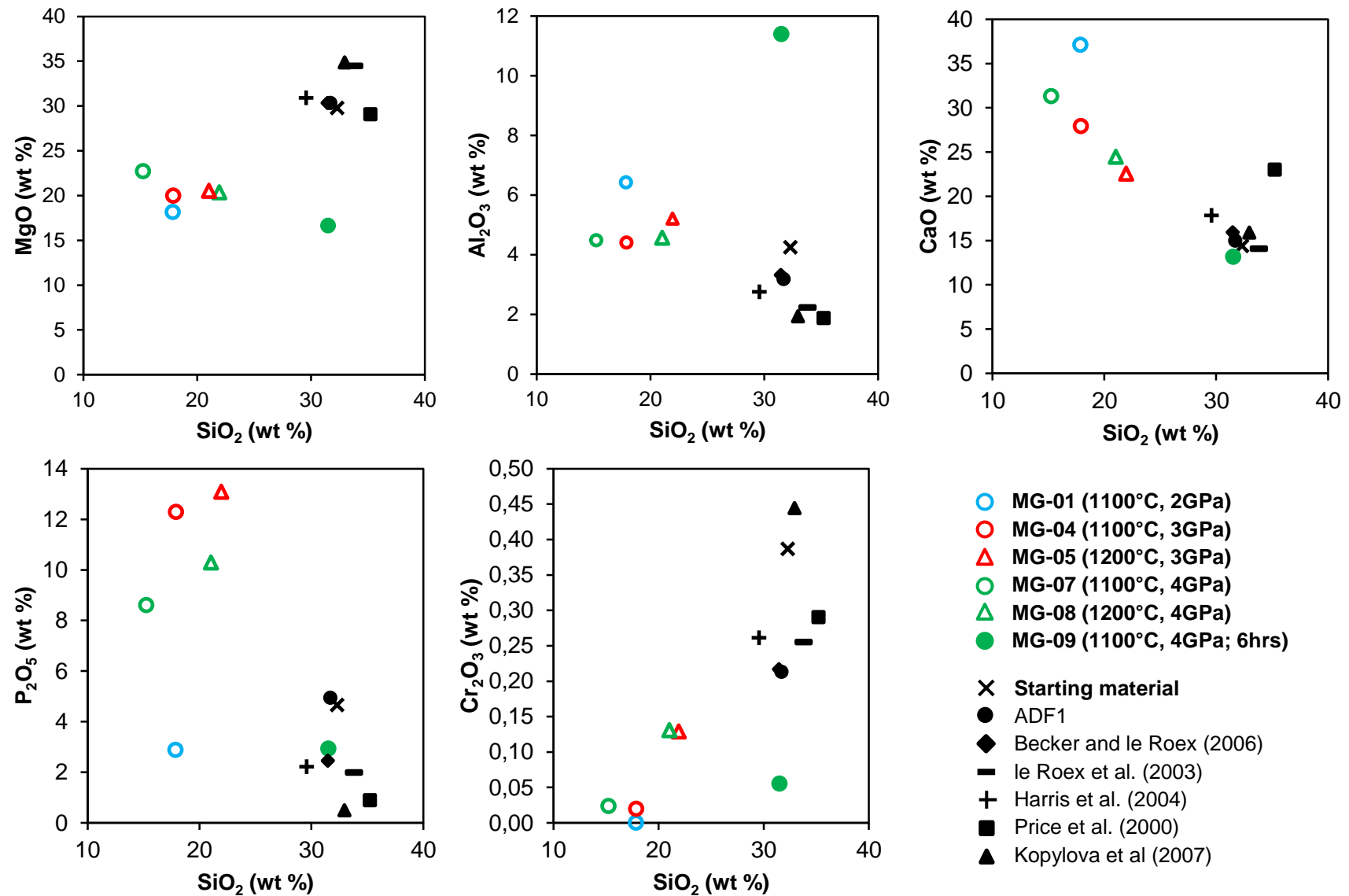


Figure 9: Comparison of melt compositions produced in the experiments to geochemically determined estimates of primary kimberlite melt compositions for selected major oxides (reported in wt %; normalised to 100% anhydrous). For melts produced in the experiments, colour represents pressure: blue = 2GPa; red = 3 GPa; green = 4GPa and shape corresponds to temperature; circle = 1100°C and triangle = 1200°C.

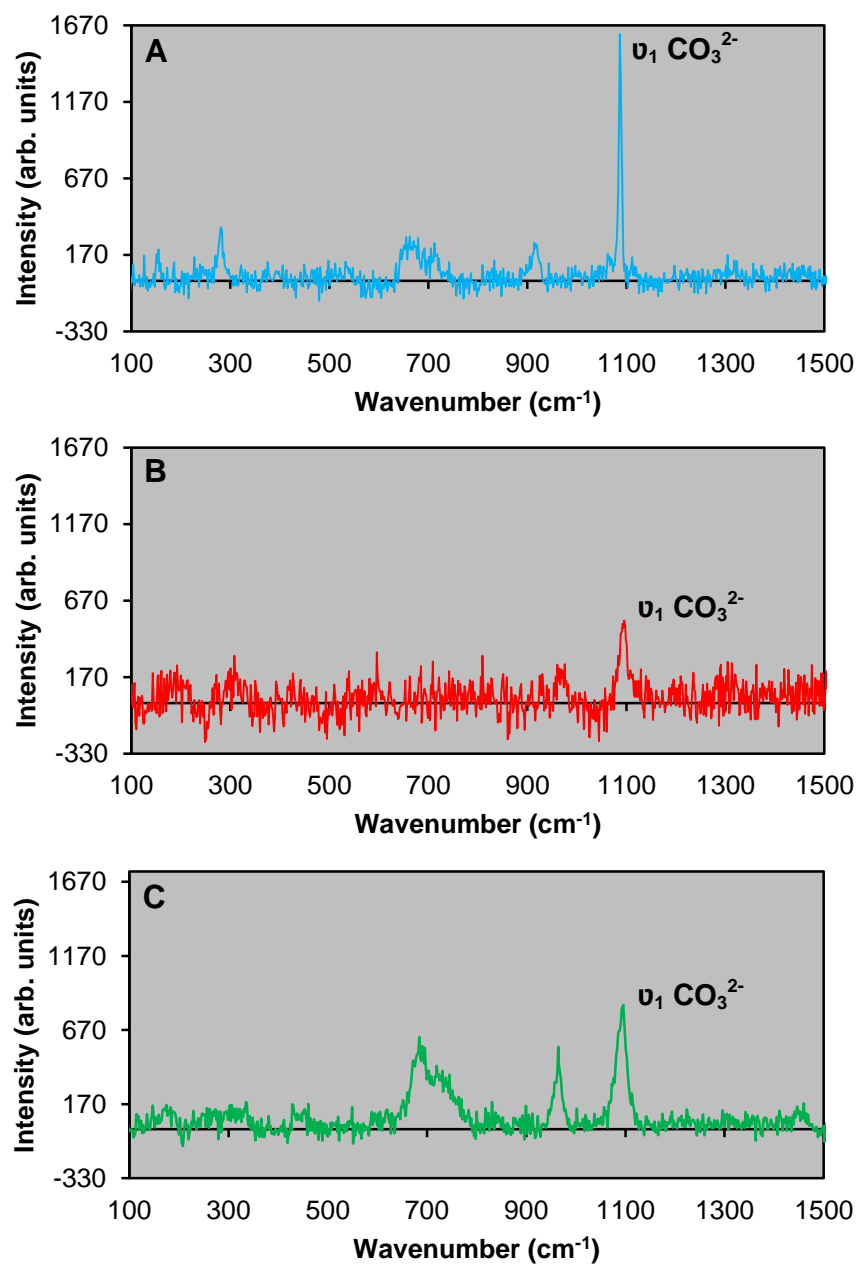


Figure 10: Background-subtracted Raman spectra of melts of A: MG-01 (1100°C, 2GPa) B: MG-04 (1100°C, 3GPa); C: MG-08 (1200°C, 4GPa). Indicated on the spectra is the position of the ν_1 Raman active vibration for carbonate which typically lies between 1050-1100cm⁻¹(Frezotti et al., 2012).

5.2.10. High temperature experiments and Fe-loss to AgPd-capsules

Fe-loss was not detected for low temperature (1100°C) runs using Ag₇₀Pd₃₀ capsules. Fe-loss to the AgPd capsules was detected for higher temperature runs using Ag₅₀Pd₅₀ (1200°C) and Ag₄₀Pd₆₀ (1300°C) capsules. Exact quantification of Fe-loss to capsule walls proved to be problematic since Fe measured within the capsule walls did not decrease uniformly with distance away from the charge. Furthermore, it was established that Fe-loss to the capsule walls varied with position in the capsule. The Fe-loss within the 1200°C runs is believed not to have affected attainment of equilibrium due to the unzoned nature of the run products and low Mg# of olivine. A substantial increase for Fe-loss and distance of Fe penetration into the capsule wall was measured in the 1300°C runs. The effect is clearly visible in the run products as elevated Mg# for both olivine and pyroxene and core to rim changes in Mg# for these phases. It would thus appear that the magnitude of Fe-loss is strongly correlated to increased temperature and increased Pd-content of the alloy. For this reason, the 1300°C experiments are not taken into consideration in this study. Additionally, MG-12 (1300°C, 4GPa) only produced melt which is not considered a consequence of Fe-loss but possibly reflect accidental addition of water to the capsule during welding.

5.3. Modal composition

Table 7 gives the modal proportions (in wt %) of phases in the experiments as determined by mass balance calculations. Lower temperature runs (1100°C) have a higher average abundance of olivine, clinopyroxene and phlogopite compared to the higher temperature runs (1200°C). Furthermore, lower temperature runs produced a smaller melt fraction than the higher temperature runs with very low melt fractions observed for MG-01 (1100°C, 2GPa), MG-07 (1100°C, 4GPa) and MG-09 (1100°C, 4GPa, 6 hours). Noteworthy is the 5 wt % garnet still present in the short duration experiment (MG-09) compared to the low proportion of garnet present in a longer duration experiment (MG-07) performed at the same PT conditions (1100°C, 4GPa). The deformed nature of capsules often resulted in the separation of the melt phase from minerals. Additionally, separation of phases into layers due to gravity and the unequal size distribution of phases in the experiments made image analyses of the samples unreliable.

Table 12: Modal proportion estimates (in wt %) of phases within run products calculated by mass balance. The mass balance calculation was performed by linear least squares regression using the data presented in Tables 4 to 11.

Exp	MG-01	MG-04	MG-05	MG-07	MG-08	MG-09
P (GPa)	2	3	3	4	4	4
T (°C)	1100	1100	1200	1100	1200	1100
Duration (hrs)	48	24	24	24	24	6
OI	48.0	36.6	34.0	37.6	38.4	49.2
Cpx	11.4	13.1	10.4	12.0	10.9	8.7
Phl	10.8	7.3	6.0	13.7	2.9	1.0
Grt	0.0	0.0	2.0	1.0	0.0	5.0
Ap	7.4	0.0	0.0	4.6	1.0	13.0
Ilm	1.0	0.0	0.0	2.2	0.1	2.0
Sp	0.0	2.1	0.9	0.0	0.0	0.0
Prv	1.5	0.0	0.0	0.0	0.0	0.0
Melt	19.5	40.9	46.7	29.1	46.7	21.2

6. Discussion

6.1. Reliability of results

The study produced a set of well equilibrated experiments. The short duration experiment [MG-09 (1100°C, 4GPa, 6 hours)] was performed to document the breakdown process of garnet. This experiment likely did not attain complete equilibration and this is attested to by the large fraction of garnet still present. Correct mineral stoichiometry, the use of a consistent set of internal standards (listed in the appendix in Table A. 1) during SEM analysis for individual phases and the close agreement of results obtained for analyses of a set of standard reference materials and their published values (results given in the appendix in Table A. 2) indicate that phase chemistry determined during SEM analysis are accurate. Low standard deviations for the number of analyses performed on individual phases are a good indication that phase compositions were consistent throughout the charge. Mixing calculations provide a good appraisal of the modal proportions of phases present within run products since the r^2 values fall within acceptable limits. The satisfactory mass balance of Fe and Mg between the starting composition, the phase compositions and the phase proportions indicate that loss of Fe to the capsule walls did not affect attainment of equilibrium for the greater part of the experiments (1100°C & 1200°C). Low Fe^{3+} values calculated for mineral phases indicate that hydrogen diffusion through the capsule walls was negligible and that the redox state of the system remained constant throughout experimental runs.

6.2. Garnet

6.2.1. Garnet stability

Garnet is absent from the run products except where it remains as zoned remnant crystals. This indicates that garnet is not stable under the investigated PT conditions and suggests rapid consumption of peridotite garnet by kimberlitic melts. This result confirms that garnet xenocrysts entrained by ascending kimberlite magmas will not survive prolonged contact with kimberlite magmas and broadly conforms to results of Canil and Fedortchouk (1999) who reported very fast dissolution rates for garnet in kimberlitic melts. Additionally, chemical heterogeneity preserved within remnant garnet crystals serves as clear evidence of the disequilibrium and the reaction relationship that exists between garnet and kimberlitic melts. The more pervasive nature of the zoning within garnet in MG-05 (1200°, 3GPa), garnet's absence in MG-08 (1200°C, 4GPa), as well as at low P and T (1100°C; 2 & 3GPa), is taken as an indication that

the rate of the reaction that consumes garnet increases with increasing T and decreasing P.

6.2.2. *Mechanisms of garnet breakdown*

Recrystallised garnet rim compositions reported around garnet xenocrysts (Table 2, Analyses F & G) used during the kimberlite melting experiments of Chepurov et al. (2013) are similar in composition to the garnet rim compositions observed in the present study. Additionally, zonation patterns which include core to rim increases in Ca, Cr and Ti for peridotite-hosted garnet have been reported in mantle metasomatism studies (Burgess and Harte, 1999; Griffin et al., 1999; Ivanic et al., 2012). Burgess and Harte (1999) labelled these rims 'Type II metasomatism' and attributed their formation to resorption of garnet by a metasomatic melt related to the kimberlite magma. It would thus appear that the formation of a compositionally distinct garnet rim, involving the elements Ca, Mg, Al, Cr and Ti, is characteristic of the interaction of garnet and kimberlite magmas and/or melts related to kimberlite magmas. In the present study, the chemical heterogeneity observed in remnant garnet crystals is interpreted as an intermediary phase preceding the complete reactive assimilation of garnet by the kimberlite magma. The reactive assimilation of garnet by the kimberlite magma manifests itself as the incongruent melting of garnet to form phlogopite as a peritectic product. Taking the mineral assemblage produced in MG-09 (1100°, 4GPa, 6hours), in which garnet remains largely unreacted, as a proxy of the equilibrium mineralogy of the kimberlite starting material (pure ADF1), it is clear that ADF1 will not crystallise a large fraction of phlogopite. This indicates that a large proportion of the phlogopite observed in MG-07 (1100°C, 4GPa, 24 hours), in which only a fraction of garnet remains, must be added to the mineral assemblage by equilibration of garnet with the kimberlite melt. To the ascending kimberlite magma this means, as calculated by mass balance, that the reactive assimilation of 5 wt % garnet by the kimberlite magma can add ~10.4 wt % phlogopite.

6.2.3. *Controls on garnet recrystallization*

The diffusion rates of major cations (Mg, Ca, Fe and Mn) in garnet crystals are very slow and diffusion profiles determined for these cations in garnet are frequently used to calculate time scales of geological processes (Carlson, 2006; Schwandt et al., 1995; Vielzeuf et al., 2007). It has been shown experimentally, that a ~1µm wide diffusion profile is established for Mg, Fe and Ca at the interface between two distinct garnet compositions over a period of 36 days at a temperature of 1200°C (Vielzeuf et

al., 2007). Thus, the formation of patchy zonation across the diameter ($\sim 115\mu\text{m}$) of the garnet crystals in MG-05 (1200°C, 3GPa) within 24 hours, argues against volume diffusion of Ca and Mg in establishing the chemical heterogeneity observed. Additionally, the separation of compositional zones by fairly sharp boundaries and the distribution of inclusions of olivine, clinopyroxene and spinel at the edge or within the rim of garnet crystals (Figures 4 & 6) favour a process of coupled dissolution-precipitation as described by Putnis (2002) and Putnis (2009). The coupling of dissolution and precipitation is suggested by Putnis (2009) to be mainly controlled by the chemistry of the melt at the reaction interface of the dissolving mineral which, even within a small charge, can be different to the overall bulk melt composition. The composition of the melt responsible for the coupling of the dissolution-precipitation process is a combination of chemical components derived from both the dissolving mineral and melt phase producing a solution in which the precipitating phase is stable (Putnis, 2002; Putnis 2009). The size of the areas required to obtain representative SEM analyses of the melt phase make it unlikely that these different melt compositions at the reaction interface between garnet crystals and the kimberlite melt can be detected in experiments involving kimberlite melt. The variation in the garnet zonation patterns (Figure 7 & 8) of the present study indicates that the melt composition responsible for the dissolution-precipitation process is dynamic. The composition changes in response to reaction kinetics as a function of P and T as well as to experimental duration as a larger volume kimberlite melt and garnet become involved. Initially the melt composition is likely dominated by chemical components derived from the dissolving garnet crystals. Rates of diffusion for divalent cations in the melt phase are however, about six orders of magnitude faster than the rates of diffusion for divalent cations in mineral phases (Zhang, 2010). Thus, with time, the melt phase will remove chemical components by diffusion from the site of reaction necessary to stabilize garnet and the initial melt phase that was responsible for the dissolution-precipitation of garnet crystals will no longer support the precipitation of garnet and the garnet will react out. The concept is illustrated by means of a simplified diagram in Figure 11.

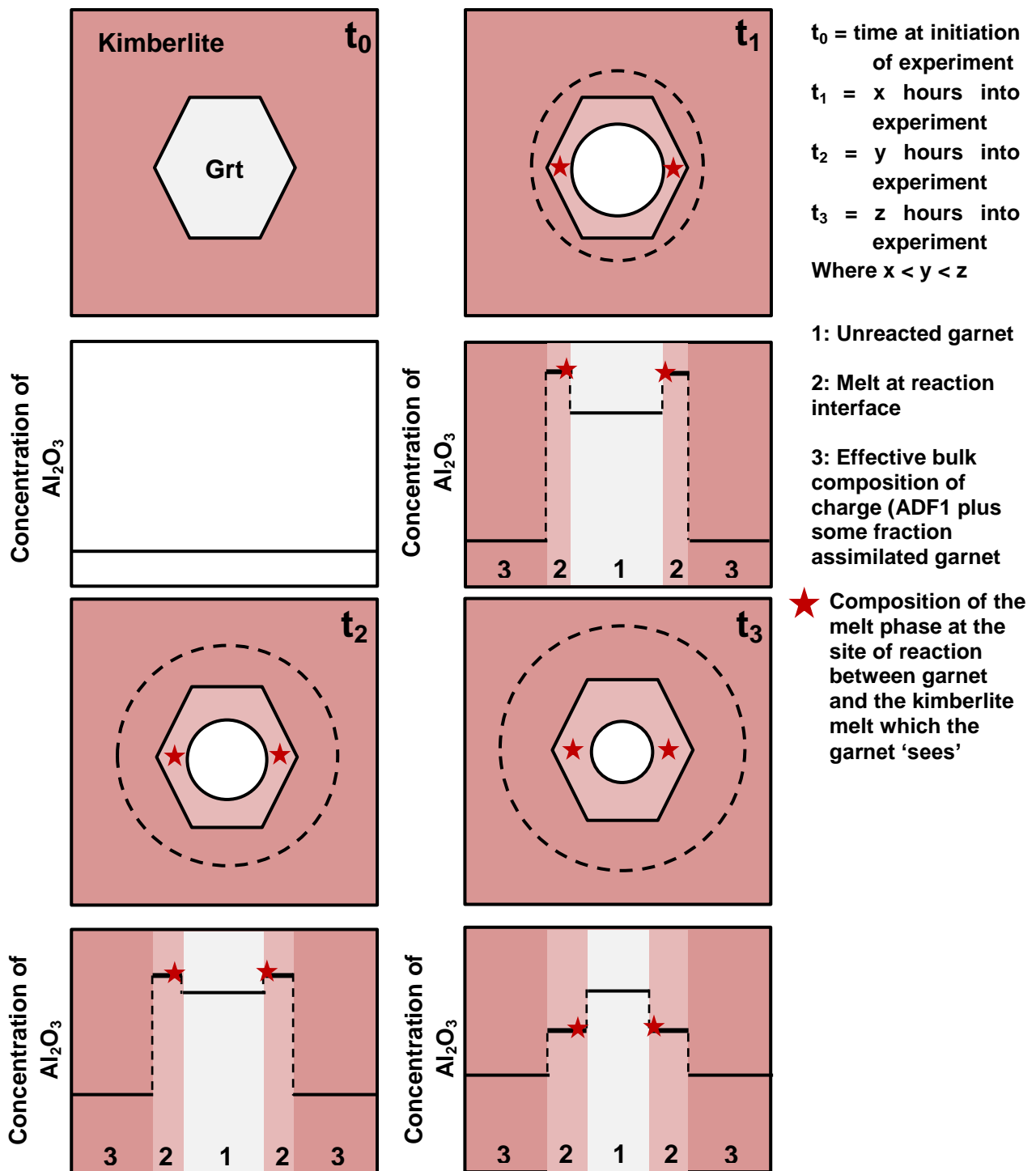


Figure 11: Simplified diagram depicting the dynamic change in melt composition at the interface between the kimberlite melt and the dissolving garnet. The melt at the interface of the dissolving garnet controls the coupled dissolution-precipitation process responsible for the chemical heterogeneity observed in the remnant garnet crystals. The melt composition changes as a function of reaction kinetics and experimental duration. t_0 = time at the initiation of the experiment. At this time garnet is unreacted and the effective bulk composition in the charge is that of the kimberlite sample (ADF1). $t_1 = x$ hours into the experiment. Garnet and the kimberlite have reacted to form a melt phase (2), at the interface of the reacting garnet, in which garnet is stable and precipitates. $t_2 = y$ hours into the experiment. The melt phase (2) changes in composition as more kimberlite sample and garnet become involved in the dissolution-precipitation process. The very high diffusion rate of chemical components in the kimberlite melt relative to garnet causes this melt phase to change in the direction of the effective bulk composition of the charge. $t_3 = z$ hours into the experiment. The composition of the melt phase (2), initially responsible for the dissolution-precipitation process, has changed as to no longer support the precipitation of garnet and garnet only dissolves. The star indicates the composition of the melt phase at the site of reaction between the garnet xenocryst and the kimberlite melt which the garnet 'sees'. Concentration Al_2O_3 was chosen to reflect the change in composition of the melt phase responsible for the dissolution-precipitation process since aluminium is essential to garnet stability and precipitation. Where x hours < y hours < z hours.

6.3. Melt compositions

6.3.1. Variation in melt compositions due to changing PT conditions and charge mineralogy

The melt compositions and mineral assemblages produced in the experiments represent those that would arise through the assimilation of peridotite garnet by the magma during its ascent through the upper mantle. The range of experimental pressures approximately corresponds to a depth interval of 66 to 130km and the range of experimental temperatures agree well with low degrees of cooling thought to be associated with kimberlite magma ascent. Kimberlite source temperatures are estimated at 1350 - 1450°C (Dalton and Presnall, 1998; Kavanagh and Sparks, 2009) and proposed to decrease to ~ 1176°C upon reaching depths equating 2GPa (Wylie and Head, 2007).

Based on SiO₂ (15.2 - 21.9 wt %) content and Mg/Ca ratios (0.68 - 1.26), the melts produced in the experiments cannot be considered kimberlitic melts (Mg/Ca ratios >2; >25 wt % SiO₂; Dalton and Presnall, 1998) and occur within the compositional window of melts described as transitional (10 - 30 wt % SiO₂; Moore and Wood, 1998) to carbonatitic (Mg/Ca ratio = 1; 5 wt % SiO₂; Dalton and Presnall, 1998).

The transition from kimberlitic to more carbonate-like melt compositions in the present study appears to be a strong function of the reaction of garnet with the kimberlite melt. This is apparent when melts produced in two experiments performed at the same PT conditions (1100°C, 4GPa) but at durations of 6 hours (MG-09) and 24 hours (MG-07) respectively, are compared (Table 13). In MG-09 garnet remains largely unreacted, whereas, only a fraction of garnet remains in MG-07 (Table 13, Figure 13 F). In addition, a small proportion of phlogopite crystallised in the short duration experiment compared to the high proportion of phlogopite crystallised in the longer duration experiment (MG-07 = 13.7 wt % phlogopite; MG-09 = 1.0 wt % phlogopite). The melt composition produced in MG-09 is kimberlitic in composition, whereas, the melt produced in MG-07 has a composition transitional between carbonatite and kimberlite. These results are interpreted to reflect incongruent melting of garnet to form phlogopite, with a shift in melt composition from kimberlitic to transitional carbonatitic.

Table 13: Composition of the starting material used in the experiments, the composition of the kimberlite composition ADF 1 and representative compositions of the melts produced in MG-07 and MG-09 (in wt %; normalised to 100% anhydrous). Also given is the modal mineralogy of MG-07 and MG-09 (in wt %). Numbers in parentheses are standard deviations: 15.2 (1.5) is 15.2 ± 1.5 . b/d = below detection

	Starting material	ADF1	Representative compositions of melts produced in MG-07 and MG-09 in wt %			Modal mineralogy of MG-07 and MG-09		
			Exp	MG-07	MG-09	Exp	MG-07	MG-09
			P(Gpa)	4	4	P (Gpa)	4	4
			T(°C)	1100	1100	T (°C)	1100	1100
			Dur(hrs)	24	6	Duration (hrs)	24	6
SiO ₂	32.28	31.68	SiO ₂	15.2 (1.5)	31.5 (2.5)	Ol	37.6	49.2
TiO ₂	1.96	2.07	TiO ₂	3.6 (0.5)	3.6 (0.7)	Cpx	12.0	8.7
Al ₂ O ₃	4.25	3.18	Al ₂ O ₃	4.5 (0.7)	11.4 (4.2)	Phl	13.7	1.0
Cr ₂ O ₃	0.39	0.21	Cr ₂ O ₃	b/d	b/d	Grt	1.0	5.0
FeO	10.41	10.62	FeO	9.5 (0.7)	13.0 (1.4)	Ap	4.6	13.0
MnO	0.22	0.20	MnO	0.4 (0.2)	b/d	Ilm	2.2	2.0
MgO	29.75	30.32	MgO	22.7 (1.1)	16.7 (2.4)	Sp	0.0	0.0
CaO	14.39	14.99	CaO	31.3 (1.6)	13.2 (2.8)	Prv	0.0	0.0
Na ₂ O	0.35	0.37	Na ₂ O	0.4 (0.2)	0.8 (0.3)	Melt	29.1	21.2
K ₂ O	1.10	1.17	K ₂ O	1.4 (0.4)	5.3 (2.2)			
P ₂ O ₅	4.66	4.95	P ₂ O ₅	8.6 (1.0)	2.9 (1.5)			
SO ₃	0.03	0.04	SO ₃	-	-			
NiO	0.18	0.19	NiO	-	-			
F	-	-	F ⁻	3.9 (1.7)	2.0 (0.3)			
Cl	-	-	Cl ⁻	0.2 (0.1)	0.4 (0.1)			
H ₂ O ⁻	0.78	0.82	H ₂ O ⁻	-	-			
H ₂ O ⁺	7.50	7.89	H ₂ O ⁺	-	-			
CO ₂	5.23	5.5	CO ₂	-	-			
			Mg#	81	69			
			SiO ₂ +Al ₂ O ₃ (wt %)	19.72	42.90			
			Mg/Ca (mol)	1.01	1.83			

Figure 12 compares melt compositions as a function of A: molar concentration of Ca, Mg, Fe and Si and B: molar concentration of Ca, P and Si. Excluding the melt produced in MG-09 from the following discussion, a noticeable correlation in melt composition and run temperature is seen. The lower temperature melts (1100°C) are furthest removed in composition from the starting composition and are more Si-poor and Ca-rich compared to the higher temperature runs (1200°C). Up temperature evolution of the melts toward the bulk composition reflects the higher melt fraction produced in the higher temperature runs (Figure 13 F). The melt compositions produced are considered to be mainly controlled by the degree of olivine and phlogopite precipitation (Figure 13 A & C). Crystallization of these phases will make melts increasingly Si-poor and Ca-rich (Kopylova et al., 2007). This is clearly evident from the higher average modal abundance of these phases (olivine = 40.7 wt %;

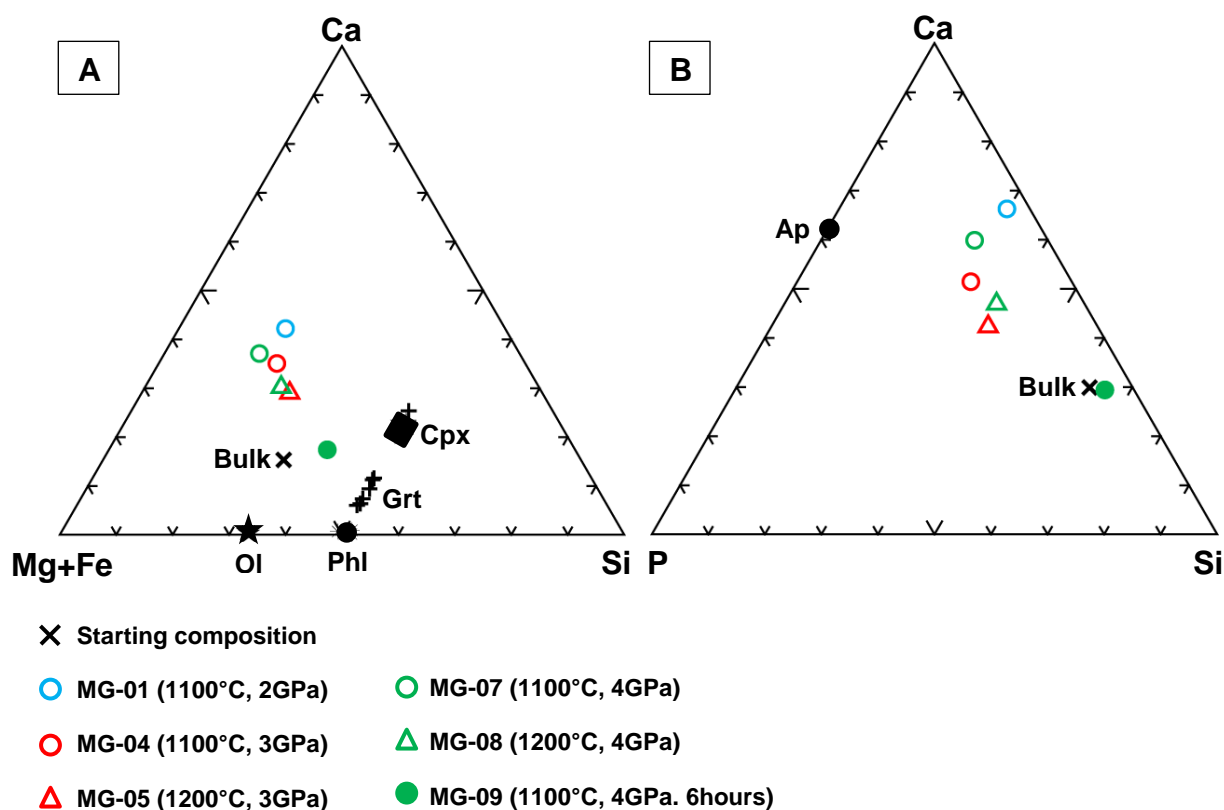


Figure 12: Comparison of melts produced in the experiments to the starting composition as a function of A: molar concentration Ca, Mg, Fe and Si; and B: molar concentration Ca, P and Si. Melt composition is seen to be correlated to experimental temperature and the degree of olivine and phlogopite precipitation. For reference, the position of the compositions of olivine (star), phlogopite (circle), clinopyroxene (square) and garnet (crosses) produced in the experiments are shown in A; and apatite in B. Molar concentrations of melts are given in the appendix (Table A.17.). Colour corresponds to pressure: blue = 2GPa; red = 3GPa; green 4GPa). Shape corresponds to temperature: circle = 1100°C; triangle = 1200°C. Filled green circle = MG-09 (1100°, 4GPa and 6 hours).

phlogopite = 10.6 wt %) in the low temperature runs compared to the lower average modal abundance (olivine = 36.2 wt %; phlogopite = 4.6 wt %) of these phases in high temperature runs. The lower Ca content of MG-04 (1100°C, 3GPa) likely reflects dilution by the higher melt fraction (Figure 13 F) as well as the higher modal abundance of clinopyroxene in this run (Figure 13 B). The P₂O₅ content of the melts produced in the experiments clearly reflects the modal abundance of apatite (Figures 12 B & 13 D). Melting or precipitation of apatite however, is not believed to exert any significant control on the Ca content of the melts. If melting of apatite was responsible for the elevated concentrations of Ca of the melts; the melts with the highest Ca content would plot directly toward the position of apatite in Figure 12 B. Furthermore no correlation exists between melts with lower or higher Ca content and the presence or absence of apatite (Figure 13 D).

Several additional aspects of the mineral assemblages produced in some of the experiments reflect the transitional carbonatitic melt compositions produced. Perovskite crystallisation is controlled by melt composition and temperature (Ogilvie-Harris et al., 2009). The occurrence of perovskite in a single experiment [MG-01 (1100°C, 2GPa)] indicates that the activity of silica was adequately low and the necessary Ca was available in this experiment to permit the precipitation of perovskite (Mitchell, 1973; Mitchell, 2008). Furthermore, spinel forms only a minor component of two experiments [MG-04 (1100°C, 3GPa) & MG-05 (1200°C, 3GPa)]. The formation of phlogopite removes Mg and Al from the system and as a consequence inhibits the formation of spinel. In absence of spinel as a sink for Ti, ilmenite precipitates as the major Ti - bearing phase.

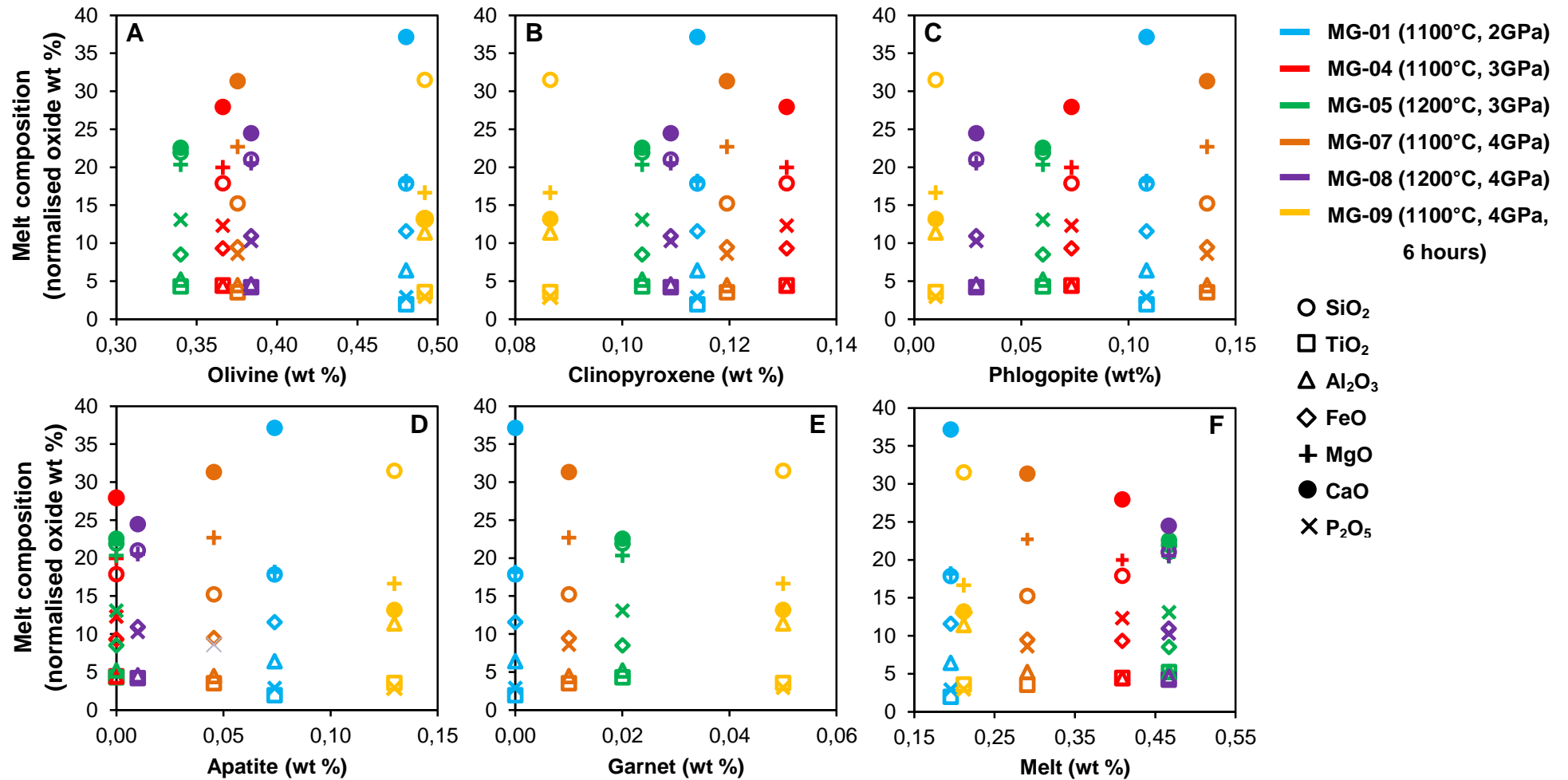


Figure 13: Melt compositions, for selected major oxides (in wt %; normalised to 100 % anhydrous), produced in the experiments as a function of the modal assemblage, for selected phases (in wt %), produced in the experiments. The low SiO₂ and high CaO content of the melts produced in the experiments strongly reflect the degree of olivine and phlogopite precipitation. A: Olivine; B: Clinopyroxene; C: Phlogopite; D: Apatite; E: Melt. Colour represents individual experiments: blue = MG-01 (1100°C, 2 GPa); red = MG-04 (1100°C, 3GPa); green = MG-05 (1200°C, 3GPa); orange = MG-07 (1100°C, 4GPa); purple = MG-08 (1200°C, 4GPa); yellow = MG-09 (1100°C, 4GPa, 6hours). Symbols represent individual major oxides: circle = SiO₂; square = TiO₂; triangle = Al₂O₃; diamond = FeO; cross = MgO; filled circle = CaO; x = P₂O₅

6.3.2. *Comparison between melt compositions produced in the present study and melt compositions produced in two related experimental investigations on orthopyroxene and omphacite breakdown in kimberlitic melts under comparable PT conditions*

Figure 14 compares the melts produced in the present study to melts produced in two related experimental investigations using the same kimberlite starting composition (ADF1, Becker and le Roex, 2006) but with added xenocrystic orthopyroxene (Jacobs, 2012) and omphacite (Burness, 2013). It is immediately apparent that melts produced, under comparable PT conditions, between the three studies are compositionally distinct. The most noticeable difference being the higher Si and lower Ca content of the melts produced in the pyroxene - melting experiments (Figure 14 C). Therefore, the melts produced in the pyroxene - melting investigations are more kimberlitic in composition. The addition of the different minerals to the kimberlite starting composition leads to marginal variations in the composition of the starting material used between the three studies. The most noteworthy difference, as a consequence of the addition of garnet xenocrysts, is increased concentration of Al_2O_3 and Cr_2O_3 of the starting material (Figure 14 B & E). Therefore, it can be concluded that a very narrow compositional control exists on melt compositions produced under comparable PT conditions.

The variation in the compositions of melts produced between the respective studies reflects a complex combination of the incongruent melting of the different added minerals, the mineral assemblages produced and the degree of crystallization. As with the present study, Jacobs (2012) and Burness (2013) invoke precipitation of olivine as a major control on melt compositions produced in their experiments. The fraction of olivine precipitated is, altogether, comparable between the three studies (Figure 14 A). The presence of a large fraction of phlogopite (Figure 12 B) due to the incongruent melting of garnet in the present study is believed to be the determinant in establishing the variation in melt compositions observed between the three studies. Additionally, precipitation of the higher proportion clinopyroxene (Figure 15 C) in the study of Jacobs (2012) and the large fraction of apatite (Figure 15 D) due to the incongruent melting of omphacite in the study of Burness (2013) at lower temperature (1100°C) would deplete the concentration of CaO in their melts relative to the present study. Furthermore, an opposite temperature trend for elevated CaO melt content is seen in the studies of Jacobs (2012) and Burness (2013). Higher concentration CaO within their melts corresponds to higher temperature. Both these authors attributed this to the melting of apatite at higher temperature. As discussed above, melting of apatite is not considered to significantly influence the concentration of CaO in the melts of the present study.

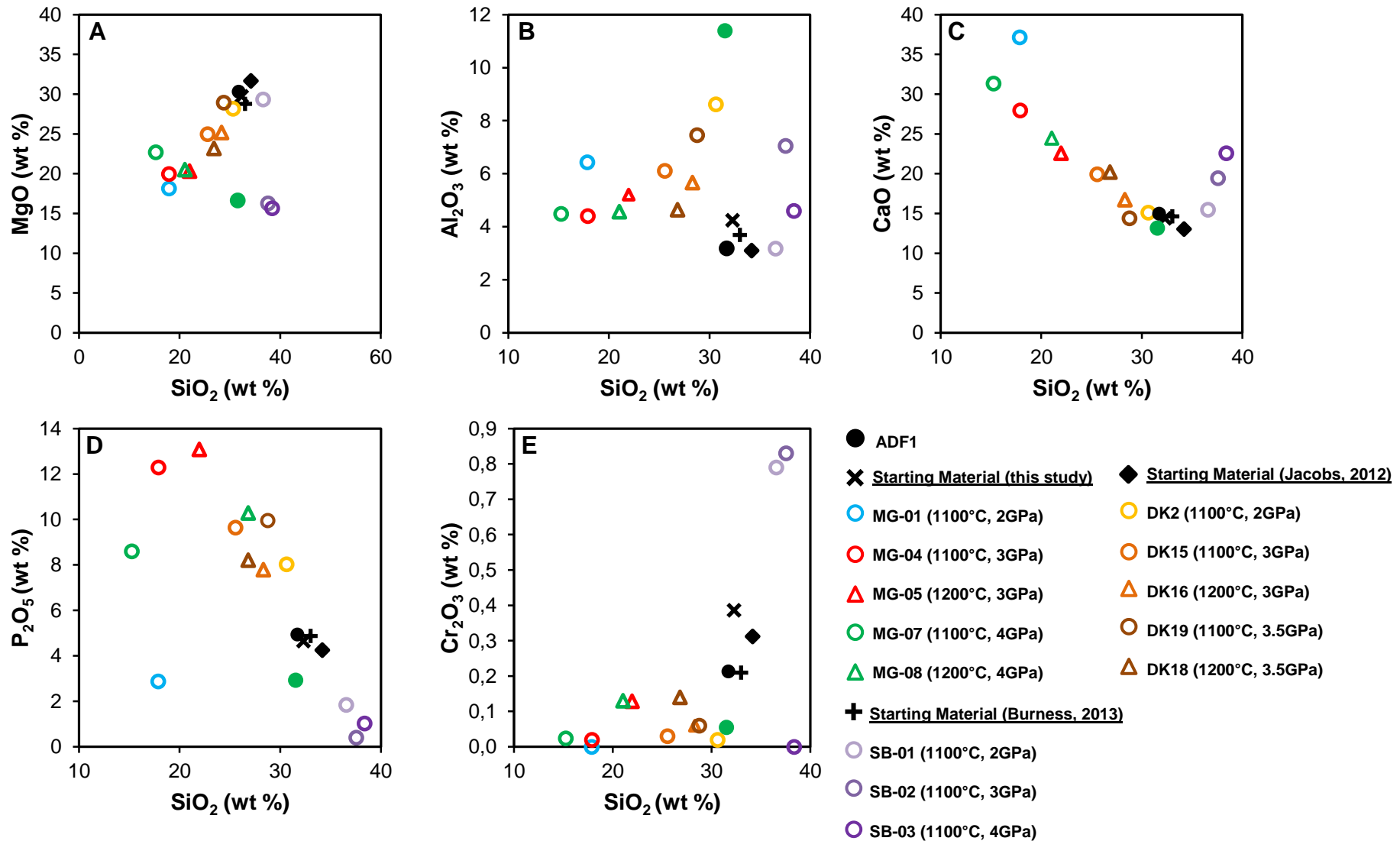


Figure 14: Comparison of melt compositions produced in the present study to melt compositions produced in two related experimental investigations using the same starting kimberlite composition (ADF 1; Becker and le Roex, 2006) but with xenocrystic orthopyroxene (Jacobs, 2012) and omphacite (Burness, 2013). The addition of the different minerals to the starting kimberlite composition leads to small variations in the composition of the starting material used in the respective studies. The large variation in the compositions of the melts produced between the three studies indicate that a very narrow compositional control exist on the melt compositions produced. The 1300°C experiments of Jacobs (2012) and Burness (2013) is not shown due to the lack of successful experiments at 1300°C in the present study.

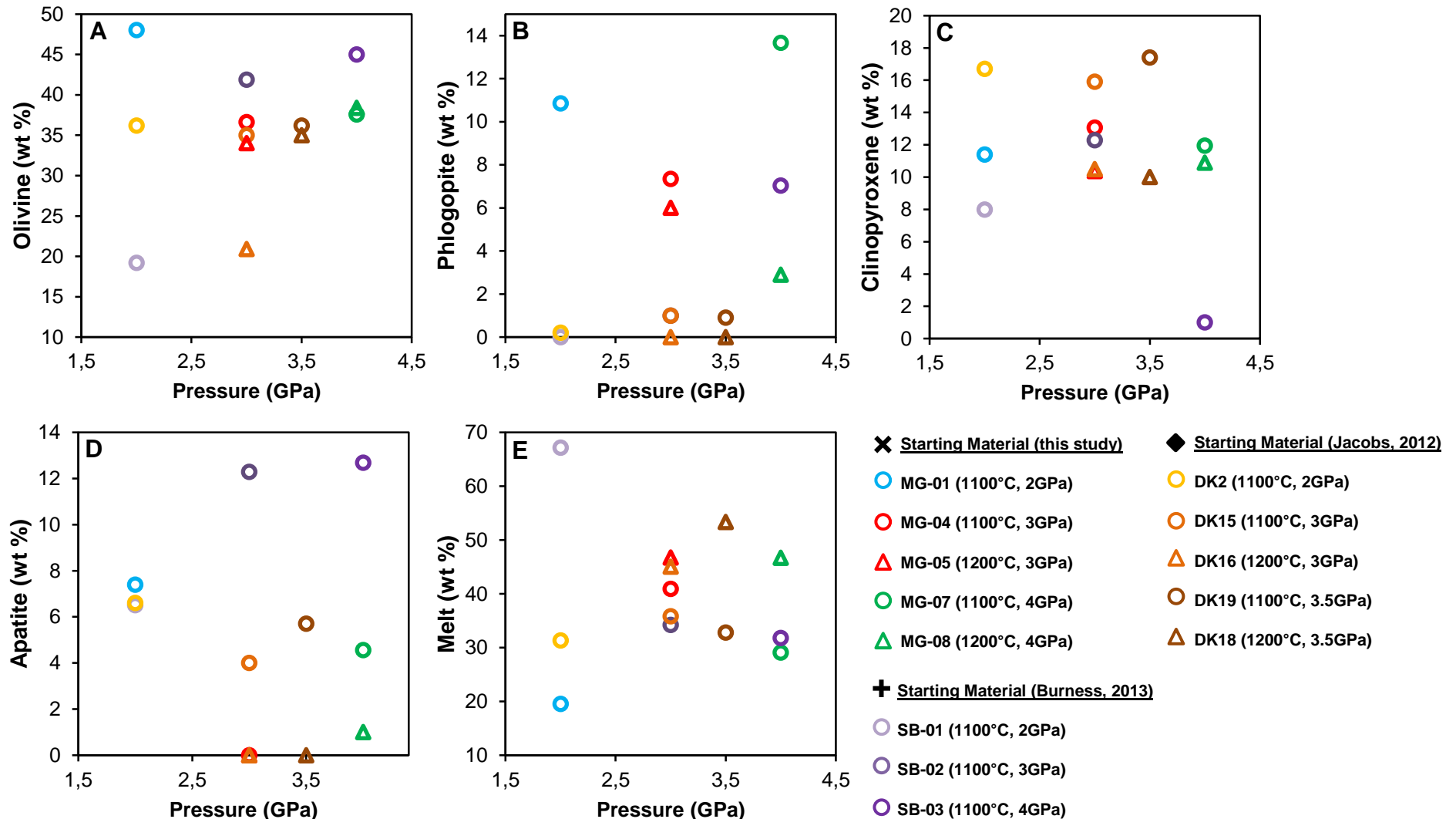
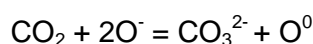


Figure 15: Comparison of the modal assemblage (for selected phases) produced in the experiments of the present study to the modal assemblages produced in the pyroxene melting experiments of Jacobs (2012) and Burness (2013). The most notable differences are the higher average abundance of phlogopite in the experiments of the present study, the higher abundance of apatite in the experiments of Burness (2013) and the higher proportion clinopyroxene in the experiments of Jacobs (2012) at lower temperature (1100°C). The formation of phlogopite as a consequence of the incongruent melting of garnet is believed to be the determinant for the variation in melt compositions observed between the present study and the pyroxene melting investigations.

6.3.3 Controls on carbonate content

CO₂ can dissolve within melts either as molecular CO₂ or as carbonate (Brooker et al., 2001). The speciation of CO₂ in melts is a function of melt composition. Melts with lower SiO₂ content (more depolymerized melt compositions) dissolves CO₂ as carbonate ions (CO₃²⁻) according to the following generalized equilibria (Brooker et al., 2001):



Where O⁻ represents a non-bridging oxygen and O⁰ a bridging oxygen (Brooker et al., 2001; and references therein). Furthermore, CO₂ solubility in melts, in addition to increasing with increasing pressure at constant temperature, has a strong compositional dependence. At a given pressure, more depolymerized melt compositions will be able to accommodate a larger fraction of dissolved CO₂ (Brooker et al., 2001; Brooker et al., 2011; Spera and Bergman, 1984). Additionally, the types of metal cations present in a given melt composition will affect melt CO₂ solubility. CO₂ solubility within melts will increase with the following order of metal cation concentration: Mg < Ca < alkalis < Al (Brooker et al., 2011; Spera and Bergman, 1980). Thus, in consideration of the compositional dependence of CO₂ solubility of melts at a given pressure, it is clear that a large fraction of dissolved CO₂ can be retained as CO₃²⁻ within the melt compositions (Table 11; Figures 12 & 13 F) produced in the present study. The presence of carbonate for three samples (MG-01; MG-04 and MG-08) was qualitatively confirmed by micro-Raman spectroscopic analysis. The ν₁ Raman active vibration for CO₃²⁻ lies between 1050-1100 cm⁻¹ (Frezotti et al., 2012) and its position is clearly visible in the Raman spectra produced for the three samples (Figure 10). The intensity of the Raman vibration is proportional to the quantity of the analysed molecule (Morizet et al., 2011 and references therein). Thus, based on the relative intensities of the carbonate peaks for the three acquired Raman spectra, a qualitative ranking for the amount CO₃²⁻ present in the melts produced, is proposed: MG-04 ≤ MG-08 < MG-01.

Figure 16 (Brooker et al., 2011) demonstrates the maximum amount of CO₂ that can be accommodated in a given SiO₂ + Al₂O₃ melt content (in wt %) at a particular pressure. The CO₂ values that are most relevant to the melts produced in the present study, are those constrained by the 2.5GPa line. The shaded areas on the 2.5 GPa line, indicate the maximum amount of CO₂ that can be accommodated in the melt compositions produced in the present study compared to the melt compositions

produced in the pyroxene melting experiments of Jacobs (2012) and Burness (2013). Thus, at 2.5 GPa, the melt compositions produced in the present study will be able to retain a larger quantity of dissolved CO₂ before saturation and subsequent exsolution of a CO₂-fluid phase than the melt compositions produced in the pyroxene melting experiments. It should be noted that, due to the positive pressure dependence of CO₂ solubility, CO₂ values for melts produced in experiments performed at 3 and 4 GPa, might be displaced to higher values.

Additionally, the purple shaded area on Figure 16, indicates where calculated CO₂ values (in wt %) for the melt compositions produced in the present study would plot; assuming that all the CO₂ present in the starting material was dissolved in the melt fraction produced. It is therefore reasonable to assume that the melts produced was not saturated in CO₂ during the experiments. And, should there have been more CO₂ present in the starting material of the experiments, melts produced would have been able to dissolve a larger quantity of CO₂.

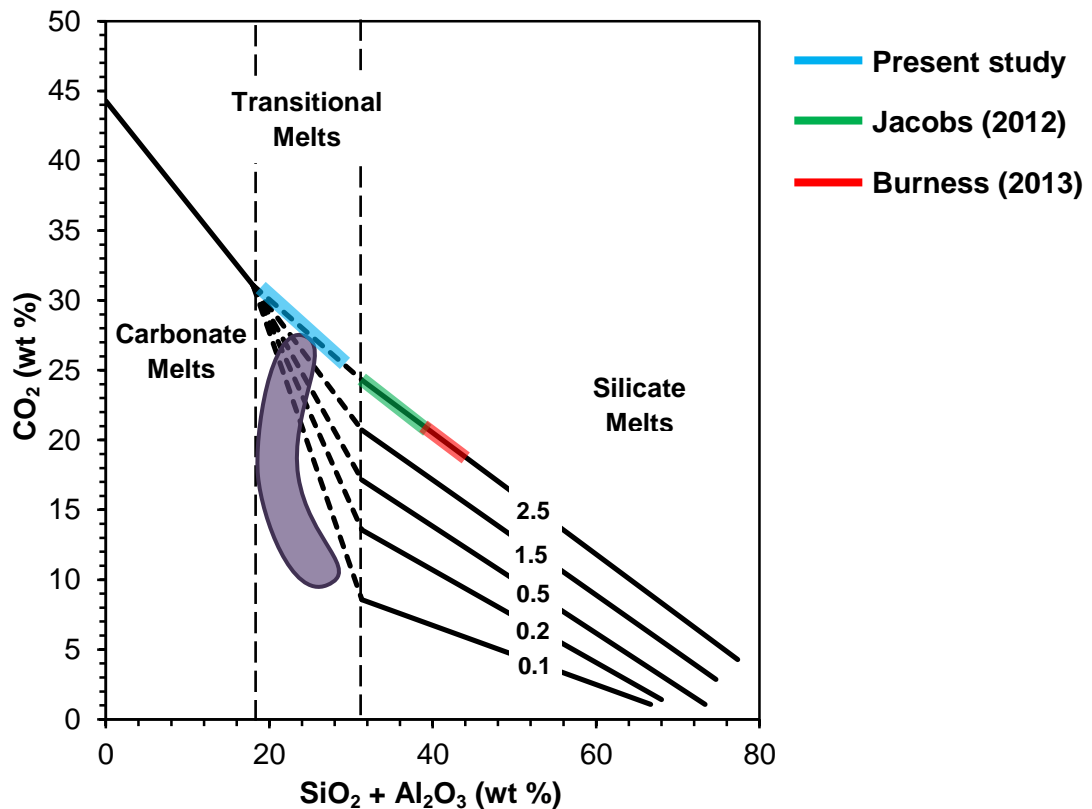


Figure 16: The silicate-carbonate transition (Brooker et al., 2011). The figure demonstrates the maximum amount of CO₂ that can be accommodated for a given SiO₂ + Al₂O₃ melt content (in wt %). Based on composition, the melts produced in the pyroxene melting investigations of Jacobs (2012) and Burness (2013) will reach saturation in CO₂ and thus exsolve CO₂ before the melts of the present study at 2.5 GPa. The purple shaded area indicates where the calculated CO₂ content as a function of melt SiO₂ + Al₂O₃ content (in wt %; normalised to 100% anhydrous) of melts produced in the present study would plot; assuming that all the CO₂ present in the starting material was dissolved in the melt fraction produced. This illustrates that the melts produced during the experiments were likely undersaturated in CO₂ during experiments. Values on the lines are pressure in GPa.

6.3.4 *Consequences of carbonate abundance*

Based on the difference in the melt compositions produced in the present study and the melt compositions produced in the pyroxene melting investigations of Jacobs (2012) and Burness (2013), it can be concluded that kimberlitic melt compositions are a strong function of xenocryst assimilation. Therefore, it can be inferred that during ascent, kimberlite magmas can follow different evolutionary pathways depending on the mineralogical make-up of the sub-continental lithospheric mantle (i.e. whether locally peridotite or eclogite is the predominant mantle lithology) as well as the degree of interaction between the ascending magma and this material. The increased capacity of the melt compositions produced in this study to dissolve CO₂ compared to the melts produced in the pyroxene melting experiments of Jacobs (2012) and Burness (2013), have important implications for both kimberlite ascent mechanisms and the dissolution rate of diamond transported by the kimberlite magma. Increased solubility of CO₂ within melts produced in the present study could impede CO₂ exsolution - driven processes believed to be essential to the rapid ascent of kimberlites (Lensky et al., 2006; Russel et al., 2012; Spera., 1984; Wilson and Head, 2007). As a consequence, kimberlite ascent might never be initiated or kimberlite ascent might occur at more moderate ascent velocities causing kimberlite ascent to cease at deeper levels in the Earth's interior.

Furthermore, experimental evidence suggests, in addition to the redox state and temperature of melts, that diamond dissolution is a strong function of the CO₂ solubility for a particular melt composition. Under the same temperature and oxygen fugacity conditions the dissolution rate of diamond is approximately six times faster in melts of kimberlitic composition than in melts of lamproitic composition. The kimberlitic melt having a higher CO₂ solubility than the lamproitic melt (Kozai and Arima, 2005). It can therefore be inferred that increased solubility of CO₂ of the melts produced as a consequence of the assimilation of garnet, will be able to dissolve diamond to a greater extent than the more silicic melt compositions produced upon the assimilation of pyroxene.

7. Conclusion

The investigation of the interaction of mantle-derived garnet and ascending kimberlite magmas is made possible by experimentally replicating a part of the ascent path of kimberlite magmas through the upper mantle. The experiments showed that garnet is not a stable equilibrium phase within kimberlite magmas under the investigated pressure and temperature conditions. The complete reactive assimilation of garnet by the kimberlite magma is preceded by the formation of a compositionally distinct garnet rim as a consequence of coupled dissolution-precipitation of the garnet xenocrysts. The reactive assimilation of garnet by the kimberlite melt manifests itself by the incongruent melting of garnet to form phlogopite as a peritectic product. It is found that the reactive assimilation of garnet with the kimberlite magma can add ~10.4 wt % phlogopite to the mineral assemblage of the ascending kimberlite magma through equilibration.

The large proportion of phlogopite produced as a consequence of the incongruent melting of garnet together with precipitation of high volumes olivine, produces transitional carbonatitic melts. This is in contrast to SiO₂-enriched melt compositions produced as a consequence of the incongruent breakdown of both orthopyroxene and omphacite in kimberlitic melts. The shift between silicic and carbonate melts appear to be controlled by marginal variation in the Al₂O₃ content of the bulk kimberlite composition due to the assimilation of the respective minerals.

The result of the melt compositions produced in this study is a higher capacity to retain larger quantities of dissolved CO₂. It is proposed that kimberlite melts is a strong function of xenocryst assimilation during their ascent through the upper mantle and can follow different evolutionary pathways depending on whether locally peridotite or eclogite is the predominant lithology present in the sub-continental lithospheric mantle. Increased CO₂ solubility within melt compositions produced can impede exsolution-driven processes believed to be essential to kimberlite ascent as well as increasing the rate of diamond dissolution during its transport by the kimberlite magma. These reasons merit further investigation of the mechanism responsible for the shift between silicic and carbonate melt compositions due to marginal variations in the kimberlite bulk composition as a consequence of the assimilation of different mantle-derived minerals by the ascending kimberlite magma.

The above mentioned implications of increased CO₂ solubility in the melt compositions produced, for both processes essential to kimberlite ascent and the rate of diamond dissolution, merits

8. References

Arndt, N.T., Guitreau, M., Boullier, A.-M., le Roex, A., Tommasi, A., Cordier, P., & Sobolev, A., 2010. Olivine, and the Origin of Kimberlite. *Journal of Petrology*, 51(3): 573-602

Barr, J.A. & Grove, T.L., 2010. AuPdFe ternary solution model and applications to understanding the fO₂ of hydrous, high-pressure experiments. *Contributions to Mineralogy and Petrology*, 160: 631-643

Becker, M. & le Roex, A.P., 2006. Geochemistry of South African on-and off- craton, Group I and Group II kimberlites: Petrogenesis and source region evolution. *Journal of Petrology*, 47 (4): 673-703

Brett, R.C., Russel, J.K. & Moss, S., 2009. Origin of olivine in kimberlite: Phenocryst or impostor? *Lithos*, 112S: 201-212

Brey, G.P., Bulatov, V.K., Gurnis, A.V. & Lahaye, Y., 2008. Experimental melting of carbonated peridotite at 6-10 GPa. *Journal of Petrology*, 49:797-821

Brooker, R.A., Kohn, S.C., Holloway, J.R. & McMillan, P.F., 2001. Structural controls on the solubility of CO₂ in silicate melts. Part I: bulk solubility data. *Chemical Geology*, 174: 225 – 239

Brooker, R.A., Sparks, R.S.J., Kavanagh, J.L. & Field, M., 2011. The volatile content of hypabyssal kimberlite magmas: some constraints from experiments on natural rock compositions. *Bulletin of Volcanology*, 73: 959-981

Burgess, S. R. & Harte, B., 1999. Tracing lithosphere evolution through the analysis of heterogeneous G9/G10 garnet in peridotite xenoliths, I: Major element chemistry. Proceedings of the 7th Kimberlite Conference. Cape Town: Red Roof Design: 66-80.

Burness, S., 2013. To investigate the stability of omphacitic clinopyroxene within a kimberlite magma at upper mantle temperature and pressure conditions. Unpublished Honour's thesis. Stellenbosch: University of Stellenbosch

Canil, D. & Fedortchouk, Y., 1999. Garnet dissolution and the emplacement of kimberlites. *Earth and Planetary Science Letters*, 167: 227-237

Carlson, W.D., 2006. Rates of Fe, Mg, Mn and Ca diffusion in garnet. *American Mineralogist*, 91: 1-11

Chepurov, A.I., Zhimulev, E.I., Agafonov, L.V., Sonin, V.M., Chepurov, A.A. & Tomilenko, A.A., (2013). The stability of ortho- and clinopyroxenes, olivine and garnet in kimberlitic magma. *Russian Geology and Geophysics*, 54: 406-415

Clement, C.R., Skinner, E.M.W. & Scott Smith, B.H., 1984. Kimberlites Redefined. *The Journal of Geology*, 92 (2): 223-228

Dalton, J.A. & Presnall, D.C., 1998. The continuum of primary carbonatitic-kimberlitic melt compositions in equilibrium with lherzolite: data from the system CaO-MgO-Al₂O₃-SiO₂-CO₂ at 6GPa. *Journal of Petrology*, 39 (11&12): 1953-1964

Dawson, J.B. & Stephens, W.E., 1975. Statistical classification of garnets from kimberlite and associated xenoliths. *The Journal of Geology*, 83 (5): 589-607

Deer, W.A., Howie, R.A., & Zussman, J. 1992. *An introduction to the rock-forming minerals*. Harlow: Pearson Prentice Hall

Droop, G.T.R., 1987. A general equation for estimating Fe³⁺ concentrations in ferromagnesian silicates and oxides from microprobe analyses using stoichiometric criteria. *Mineralogical Magazine*, 51:431-435.

Frezzotti, M.L., Tecce, F. & Casagli, A., 2011. Raman spectroscopy for fluid inclusion analysis. *Journal of Geochemical Exploration*, 112: 1–20

Girnis, A.V., Brey, G.P. & Ryabchikov, I.D., 1995. Origin of Group IA Kimberlites: Fluid-saturated melting experiments at 45 – 55 kbar. *Earth and Planetary Science Letters*, 134:283-296

Griffin, W.L., Fisher, N.I., Friedman, J, Ryan, C.G. & O'Reilly, S.Y., 1999. Cr-pyrope garnets in the lithospheric mantle. I. Compositional systematics and relations to tectonic setting. *Journal of Petrology*, 40 (5): 679-704

- Griffin, W.L., Shee, S.R., Ryan, C.G., Win, T.T & Wyatt, B.A., 1999. Harzburgite to Iherzolite and back again: metasomatic processes in ultramafic xenoliths from the Wessolton kimberlite, Kimberley, South Africa. *Contributions to Mineralogy and Petrology*, 134: 232-250
- Harris, M., le Roex, A.P. & Class, C., 2004. Geochemistry of the Uintjiesberg kimberlite, South Africa: petrogenesis of an off-craton, Group I, kimberlite. *Lithos*, 74: 149-165
- Holleck, G.L., 1970. Diffusion and Solubility of hydrogen in palladium and palladium-silver alloys. *The Journal of Physical Chemistry*, 73 (3): 503-511
- Hunter, R.H. & Taylor, L.A., 1982. Instability of garnet from the mantle: Glass as evidence of metasomatic melting. *Geology*, 10: 617-620
- Ivanic, T.J., Harte, B. & Gurney, J.J., 2012. Metamorphic re-equilibration and metasomatism of highly chromian, garnet-rich xenoliths from South African kimberlites. *Contributions to Mineralogy and Petrology*, 164: 505-520
- Jacobs, D. 2012. Orthopyroxene stability within kimberlite magma: an experimental investigation. Unpublished master's thesis. Stellenbosch: University of Stellenbosch
- Jakobsson, S., 2012. Oxygen fugacity control in piston-cylinder experiments. *Contributions to Mineralogy and Petrology*, 164: 397-406
- Johannes, W., Chipman, D.W., Hays, J.F., Bell, P.M., Mao, H.K., Newton, R.C., Boettcher, A.L. & Seifert, F., (1971). An interlaboratory comparison of pressure calibration using the albite-breakdown reaction. *Contributions to Mineralogy and Petrology*, 32: 24-38
- Kavanagh, J.L. & Sparks, R.S.J., 2009. Temperature changes in ascending kimberlite magma. *Earth and Planetary Science Letters*, 286: 404-413
- Kopylova, M.G., Mateev, S. & Raudesepp, M., 2007. Searching for parental kimberlite melt. *Geochimica et Cosmochimica Acta*, 71: 3616-3629
- Kozai, Y. & Arima, M., 2005. Experimental study on diamond dissolution in kimberlitic and lamproitic melts at 1300-1420°C and 1 GPa with controlled oxygen partial pressure. *American Mineralogist*, 90: 1759-1766

Lensky, N.G., Niebo, R.W., Holloway, J.R., Lyakhovsky, V. & Navon, O., 2006. Bubble nucleation as a trigger for xenolith entrapment in mantle melts. *Earth and Planetary Science Letters*, 245: 278-288

le Roex, A.P., Bell, D.R. & Davies, P., 2003. Petrogenesis of Group I kimberlites from Kimberley, South Africa: Evidence from bulk-rock geochemistry. *Journal of Petrology*, 44 (12): 2261-2286

Merrill, B.R. & Wyllie, P.J., 1973. Absorption of iron by platinum capsules in high pressure rock melting experiments. *American Mineralogist*, 58: 16-20

Mitchell, R.H., 1973. Composition of olivine, silica activity and oxygen fugacity in kimberlite. *Lithos*, 6: 65-81

Mitchell, R.H., 2008. Petrology of hypabyssal kimberlite: Relevance to primary magma compositions. *Journal of Volcanology and Geothermal Research*, 174: 1-8

Morizet, Y., Brooker, R.A., Iacono-Mariziano, G. & Kjarsgaard, B.A., 2013. Quantification of dissolved CO₂ in silicate glasses using micro-Raman spectroscopy. *American Mineralogist*, 98: 1788-1802

Ogilvie-Harris, R.C., Field, M, Sparks, R.S.J. & Walter, M.J., 2009. Perovskite from Dutoitspan kimberlite, Kimberley, South Africa: implications for magmatic processes. *Mineralogical Magazine*, 73 (6): 915-928

Price, S.E., Russel, J.K. & Kopylova, M.G., 2000. Primitive magma from the Jericho Pipe, N.W.T., Canada: Constraints on primary kimberlite melt chemistry. *Journal of Petrology*, 41(6): 789-808

Putnis, A., 2002. Mineral replacement reactions: from macroscopic observations to microscopic mechanisms. *Mineralogical Magazine*, 66 (5): 689-708

Putnis, A., 2009. Mineral replacement reactions. *Reviews in Mineralogy and Geochemistry*, 20: 87-124

Russel, J.K., Porritt, L.A., Lavallée & Dingwell, D.B., 2011. Kimberlite ascent by assimilation-fuelled buoyancy. *Nature*: 481, 352-357

Schulze, D.J., 2003. A classification scheme for mantle-derived garnets in kimberlite: a tool for investigating the mantle and exploring for diamonds. *Lithos*, 71: 195-213

Schwandt, C.S., Cygan, R.T. & Westrich, H.R., 1995. Mg-self diffusion in pyrope garnet. *American Mineralogist*, 80: 483-490

Sparks, R.S.J., Baker, L., Brown, R.J., Field, M., Schumacher, J., Stripp, G. & Walters, A., 2006. Dynamical constraints on kimberlite volcanism. *Journal of Volcanology and Geothermal Research* 155: 18-48

Sparks, R.S.J., Brooker, R.A., Field, M., Kavanagh, J., Schumacher, J.C., Walter, M.J. & White, J., 2009. The nature of erupting kimberlite melts. *Lithos*, 112S: 429-438

Spera, F.J & Bergman, S.C., 1980. Carbon dioxide in igneous petrogenesis: I. Aspects of the dissolution of CO₂ in silicate liquids. *Contributions to Mineralogy and Petrology*, 74: 55-66

Spera, F.J., 1984. Carbon dioxide in petrogenesis III: role of volatiles in the ascent of alkaline magma with special reference to xenolith-bearing mafic lavas. *Contributions to Mineralogy and Petrology*, 88: 217-232

Stachel, T. & Harris, J.W., 2008. The origin of cratonic diamonds-Constraints from mineral inclusions. *Ore Geology Reviews* 34: 5-32

Vielzeuf, D., Baronnet, A., Perchuk, A.L., Laporte, D. & Baker, M.B., 2007. Calcium diffusivity in alumina-silicate garnets: an experimental and ATEM study. *Contributions to Mineralogy and Petrology*, 154: 153-170

Watson, E.B. & Price, J.B., 2002. Kinetics of the reaction $\text{MgO} + \text{Al}_2\text{O}_3 \rightarrow \text{MgAl}_2\text{O}_4$ and Al-Mg interdiffusion in spinel at 1200 to 2000°C and 1.0 to 4.0GPa. *Geochemica et Cosmochimica Acta*, 66 (12): 2123-2138

Watson, E.B., Wark, D.A., Price, J.D. & Van Orman, J.A., 2002. Mapping the thermal structure of solid-media pressure assemblies. *Contributions to Mineralogy and Petrology*, 142: 640-652

Wilson, L & Head, J.W., 2007. An integrated model of kimberlite ascent and eruption. *Nature*, 47: 53-57

Wood, B.J., Ekaterina S. Kiseeva, E.S. & Matzen, A.K., 2013. Garnet in the Earth's Mantle. *Elements*, 9: 421-426

Zhang, Y., 2010. Diffusion in Minerals and Melts: Theoretical Background. *Reviews in Mineralogy & Geochemistry*, 72: 5-59

9. Appendices

Appendix 1: Internal standards used during SEM analysis of mineral phases in run products and results of SEM analysis of standard reference material.

Table A.1. Internal standards used during SEM analysis of mineral phases in run products

	Olivine	Pyroxene	Phlogopite	Garnet	Apatite	Ilmenite	Spinel	Perovskite
SiO ₂	Pyrope	Sanidine	Pyrope	Pyrope	Pyrope	-	Pyrope	-
TiO ₂	Ilmenite	Ilmenite	Ilmenite	Ilmenite	-	Ilmenite	Ilmenite Plagioclase	Ilmenite
Al ₂ O ₃	-	Pyrope	Pyrope	Spodumene	-	Pyrope	An ₆₅	Pyrope
Cr ₂ O ₃	Chromite	Chromite	Chromite	Chromite	-	Chromite	Chromite	-
Nb ₂ O ₅	-	-	-	-	-	Pure niobium	-	Pure niobium
V ₂ O ₃	-	-	-	-	-	Pure vanadium	-	-
FeO	Ilmenite	Ilmenite	Ilmenite	Ilmenite	Ilmenite	Ilmenite	Ilmenite	Ilmenite
MnO	Rhodonite	Rhodonite	Rhodonite	Rhodonite	-	Rhodonite	Rhodonite	-
MgO	Olivine	Diopside	Pyrope	Olivine	Pyrope	Pyrope	Pyrope	Pyrope
CaO	Diopside	Diopside	Diopside	Diopside	Apatite	-	-	Apatite
SrO	-	-	-	-	Celestite	-	-	-
Na ₂ O	-	-	Albite	-	-	-	-	-
K ₂ O	-	-	Sanidine	-	-	-	-	-
P ₂ O ₅	-	-	-	-	Apatite	-	-	-
NiO	Olivine	-	-	Olivine	-	Olivine	Olivine	-
F	-	-	Apatite	-	Apatite	-	-	-

Table A.2. Comparison of published major element concentrations (in wt %) of mineral standards and measured values (in wt %) determined by SEM analysis. Mineral formulae were calculated on the basis of 4 oxygens for olivine, 6 oxygens for diopside, 12 oxygens for garnet and 24 oxygens (ΣO , OH, F) for kaersutite. X_{Fo} , X_{Fa} , X_{Py} , X_{Alm} , X_{Spss} , and X_{Grss} calculated as defined by Deer, Howie & Zussman (1992). A: Reported on a water-free basis. n/d= not detected

												A			
Olivine				Diopside				Garnet				Kaersutite			
Actual	Measured	%Dev		Actual	Measured	%Dev		Actual	Measured	%Dev		Actual	Measured	%Dev	
SiO ₂	41.58	41.54	-0.1	SiO ₂	55.37	55.65	0.5	SiO ₂	41.45	41.76	0.8	SiO ₂	40.09	40.03	-0.2
FeO	7.51	7.78	3.5	TiO ₂	0.08	0.07	-9.9	TiO ₂	1.16	1.07	-7.5	TiO ₂	5.04	5.01	-0.6
MnO	0.1	0.06	-42.1	Al ₂ O ₃	0.09	0.03	-68.8	Al ₂ O ₃	21.32	21.26	-0.3	Al ₂ O ₃	12.36	13.02	5.1
MgO	50.43	50.38	-0.1	FeO	0.05	0.03	-38.7	Cr ₂ O ₃	0.58	0.56	-3.0	FeO	12.23	12.24	0.1
NiO	0.38	0.39	2.6	MnO	0.05	0.00	n/d	FeO	11.15	11.48	3.0	MnO	0.18	0.19	5.2
Total	100.00	100.14		MgO	18.62	18.59	-0.1	MnO	0.27	0.25	-8.5	MgO	12.55	12.32	-1.9
				CaO	25.73	25.90	0.7	MgO	19.33	18.99	-1.7	CaO	11.56	11.18	-3.4
xO ²⁻	4	4		Total	99.99	100.28		CaO	4.65	4.39	-5.6	Na ₂ O	2.44	2.58	5.4
Si	1.01	1.01						Total	99.91	99.77		K ₂ O	1.17	1.01	-16.3
Fe ²⁺	0.15	0.16		xO ²⁻	6	6						Total	97.62	97.57	
Mn	0.00	0.00		Si	2.00	2.00		xO ²⁻	12	12					
Mg	1.82	1.82		Ti	0.00	0.00		Si	2.99	3.01		xO ²⁻	24	24	
Ni	0.01	0.01		Al	0.00	0.00		Ti	0.06	0.06		Si	6.24	6.22	
Total	2.99	2.99		Fe ²⁺	0.00	0.00		Al	1.81	1.81		Ti	0.59	0.59	
Mg#	92	92		Mn	0.00	0.00		Cr	0.03	0.03		Al	2.27	2.38	
X _{Fo}	92.29	92.03		Mg	1.00	1.00		Fe ²⁺	0.67	0.69		Fe ²⁺	1.59	1.59	
X _{Fa}	7.71	7.97		Ca	0.99	1.00		Mn	0.02	0.02		Mn	0.02	0.02	
				Total	4.00	4.00		Mg	2.08	2.04		Mg	2.91	2.85	
								Ca	0.36	0.34		Ca	1.93	1.86	
								Total	8.02	8.01		Na	0.74	0.78	
								Mg#	76	75		K	0.23	0.20	
								X _{Py}	66.47	66.47		Total	16.52	16.49	
								X _{Alm}	21.51	21.51		Mg#	65	64	
								X _{Spss}	0.53	0.53					
								X _{Grss}	9.76	9.76					

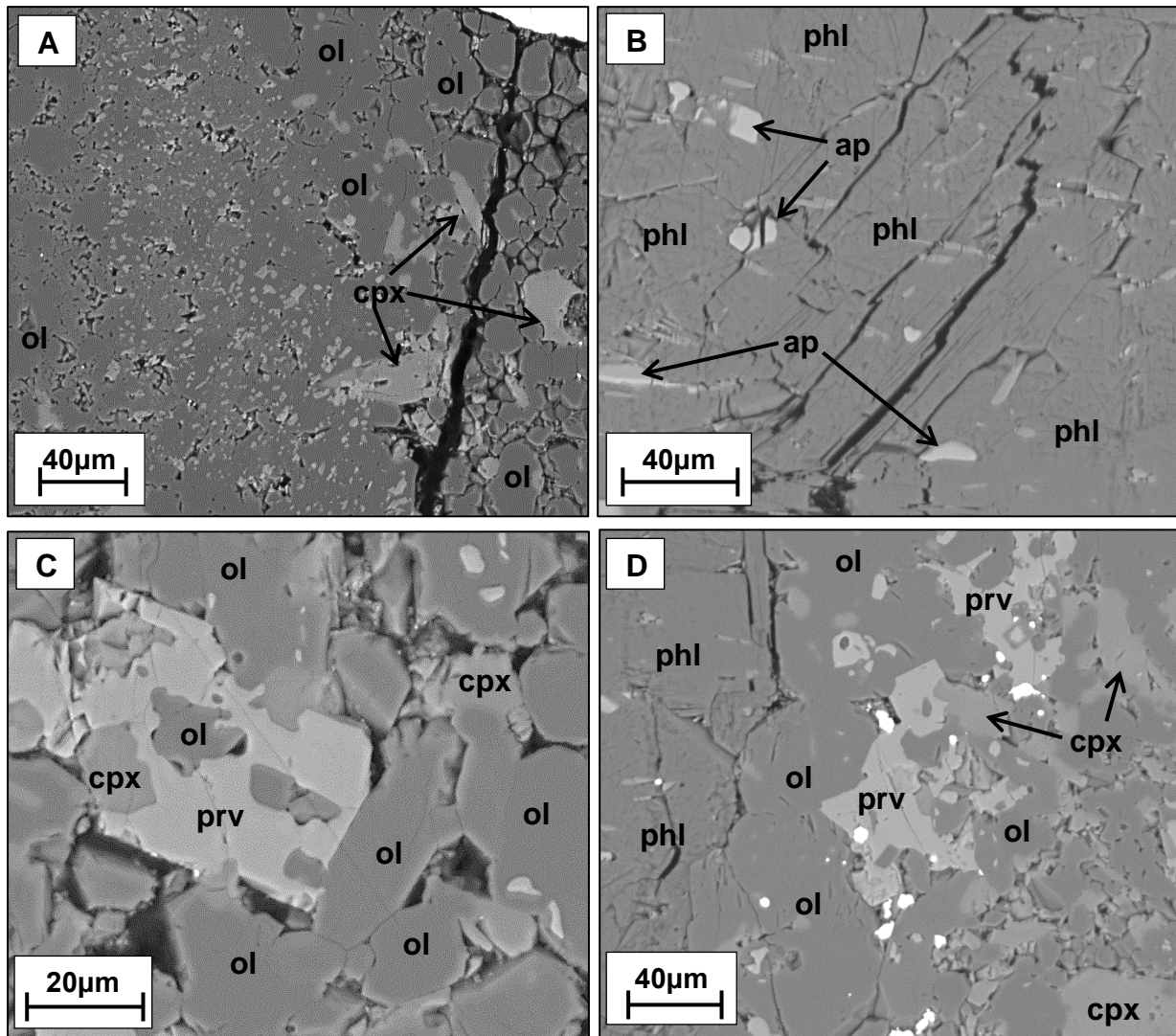
Appendix 2: Back-scattered electron images of textural characteristics of run products

Figure A.1: Back-scattered electron images of textural features produced in MG-01 (1100°C, 2GPa). A: Small clinopyroxene grains surrounded by olivine. Also present is few larger subhedral grains of clinopyroxene. B: Large blade-like phlogopite with small insets of apatite. C: Perovskite enclosing anhedral olivine and pyroxene. D: Irregular perovskite situated between phlogopite-rich layer and olivine plus clinopyroxene layer.

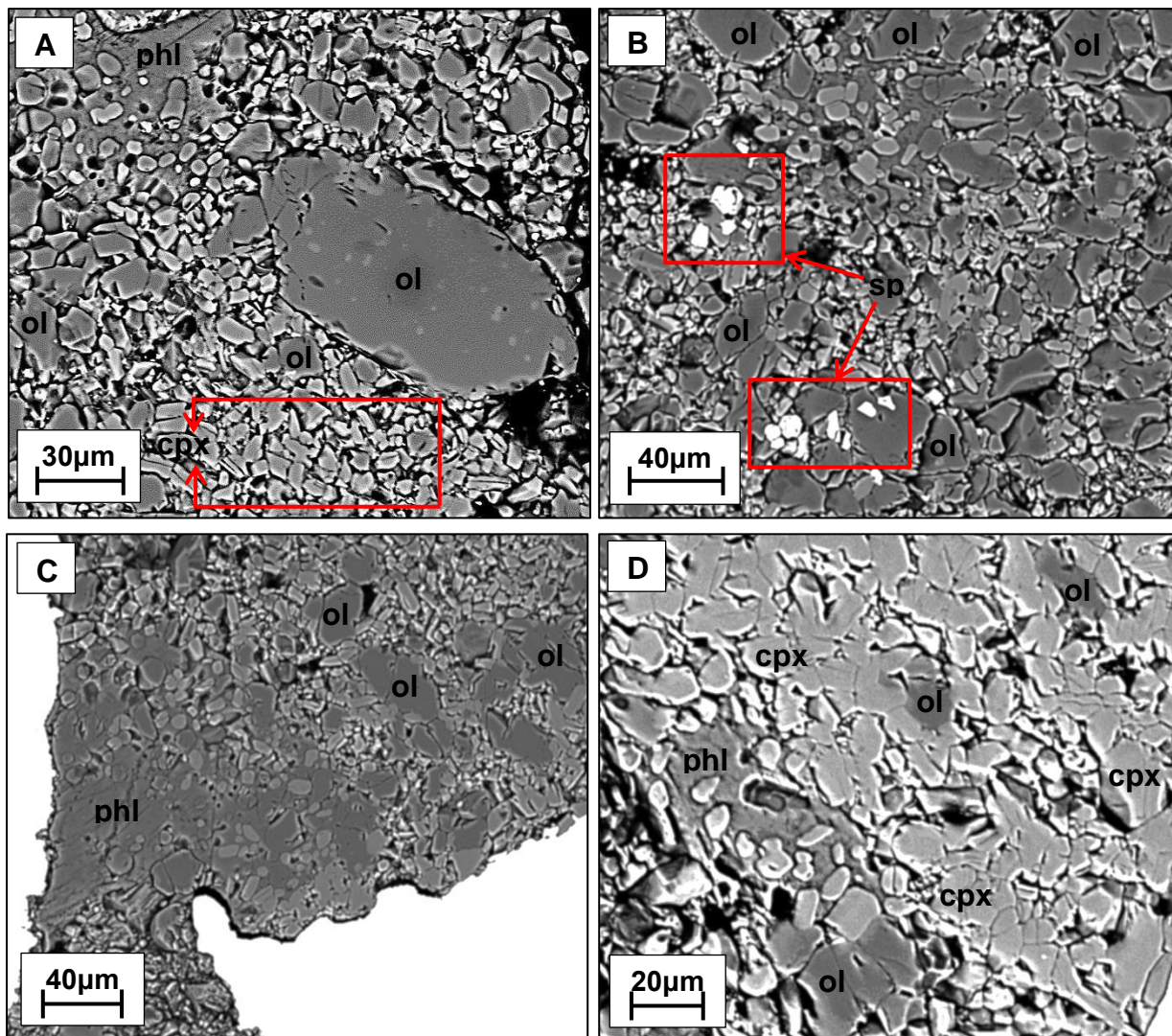


Figure A.2: Back-scattered electron images of textural features produced in MG-04 (1100°C, 3GPa). A: Large subhedral olivine with small inclusions of clinopyroxene. B: Small anhedral spinel crystals. C: Large interstitial pool of phlogopite poikilitically enclosing rounded grains of olivine and clinopyroxene. D: Aggregate of small rectangular subhedral clinopyroxenes.

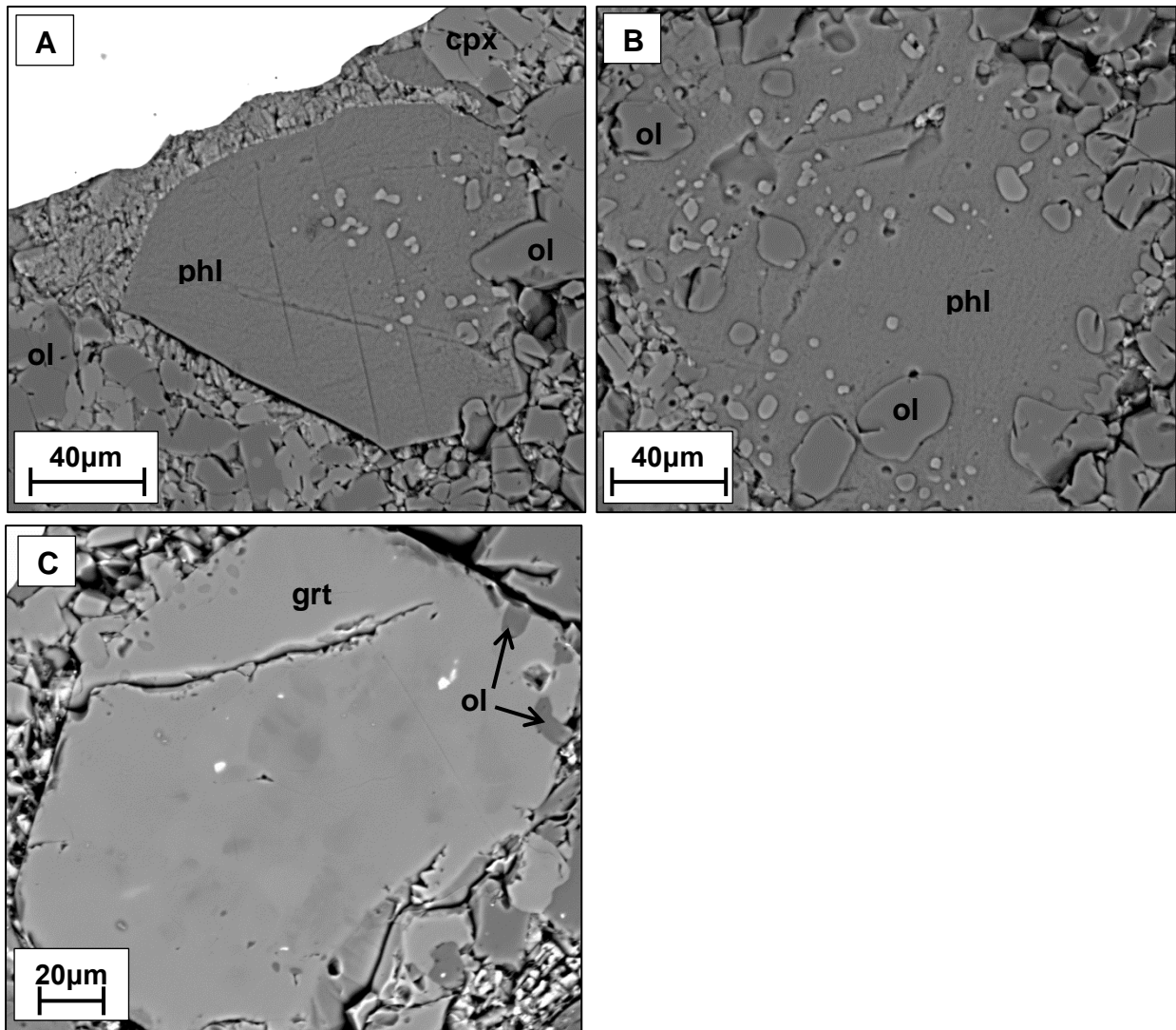


Figure A.3: Back-scattered electron images of textural features produced in MG-05 (1200°C, 3GPa). A: Large phlogopite displaying prominent cleavage. Small inclusions of rounded olivine and clinopyroxene are present in the phlogopite grain. B: Large interstitial pool of phlogopite poikilitically enclosing rounded grains of olivine and clinopyroxene. C: Zoned remnant garnet crystal.

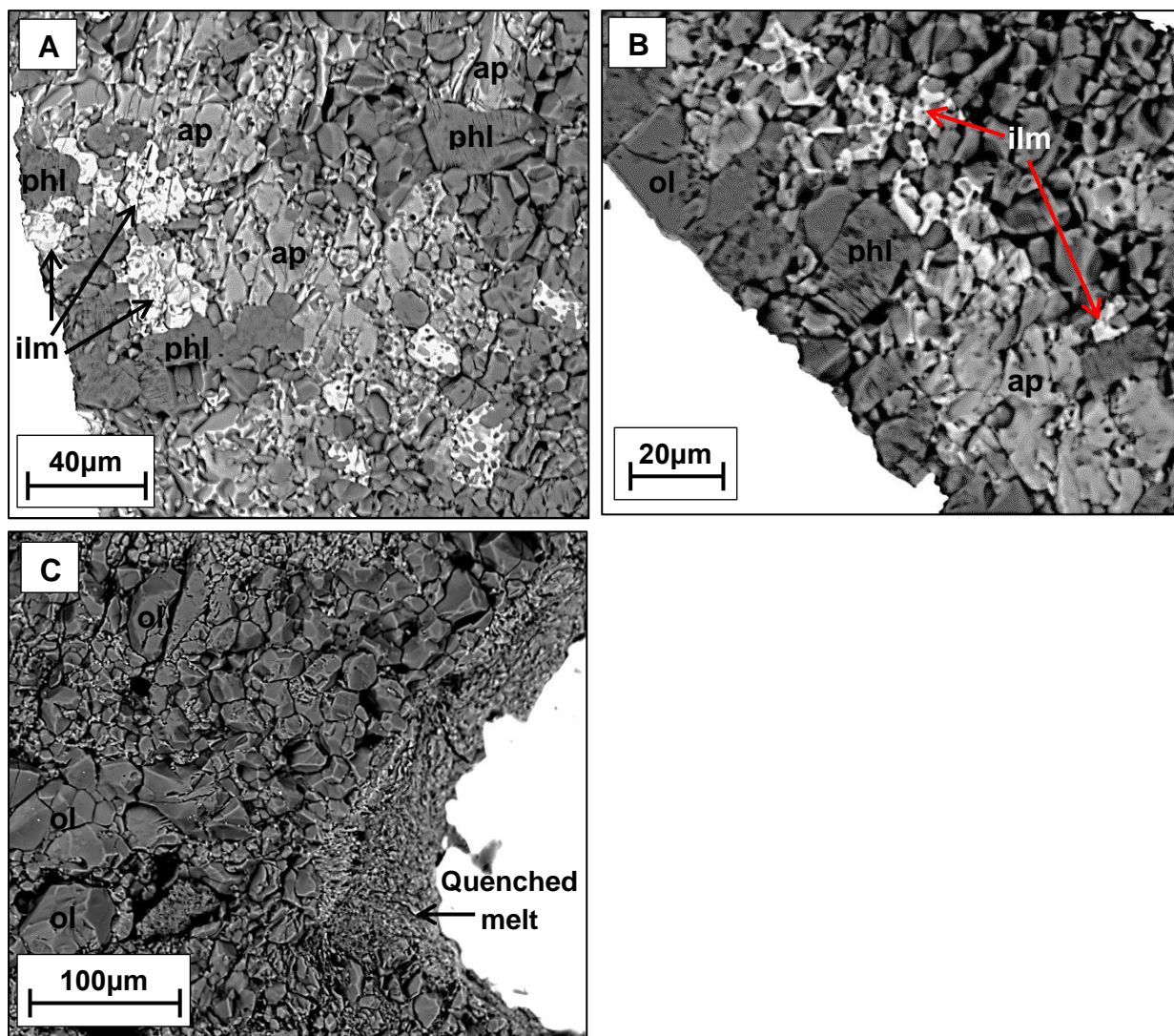


Figure A.4: Back-scattered electron images of textural features produced in MG-07 (1100°C, 4GPa). A: Anhedral apatite, anhedral ilmenite and globular phlogopite. Ilmenite has a pitted appearance due to enclosing small grains of olivine. B: Anhedral apatite and ilmenite with blocky phlogopite. C: Quenched melt separated from adjacent olivine.

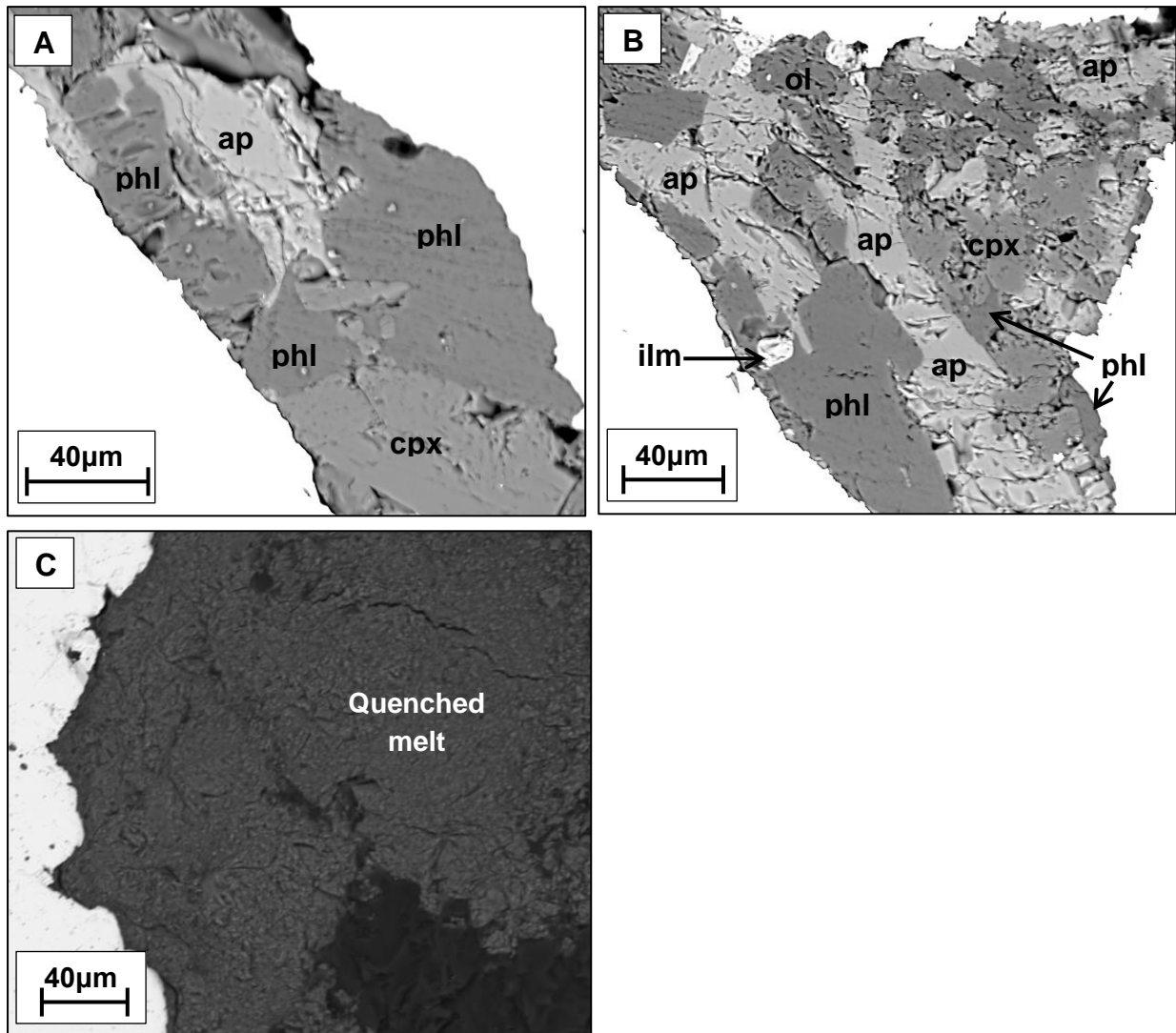


Figure A.5: Back-scattered electron images of textural features produced in MG-08 (1200°C, 4GPa). A: Large anhedral apatite and clinopyroxene adjacent to phlogopite. B: Large elongated apatite separated from adjacent phlogopite and clinopyroxene by fairly straight grain boundaries. C: Large pool of quenched melt.

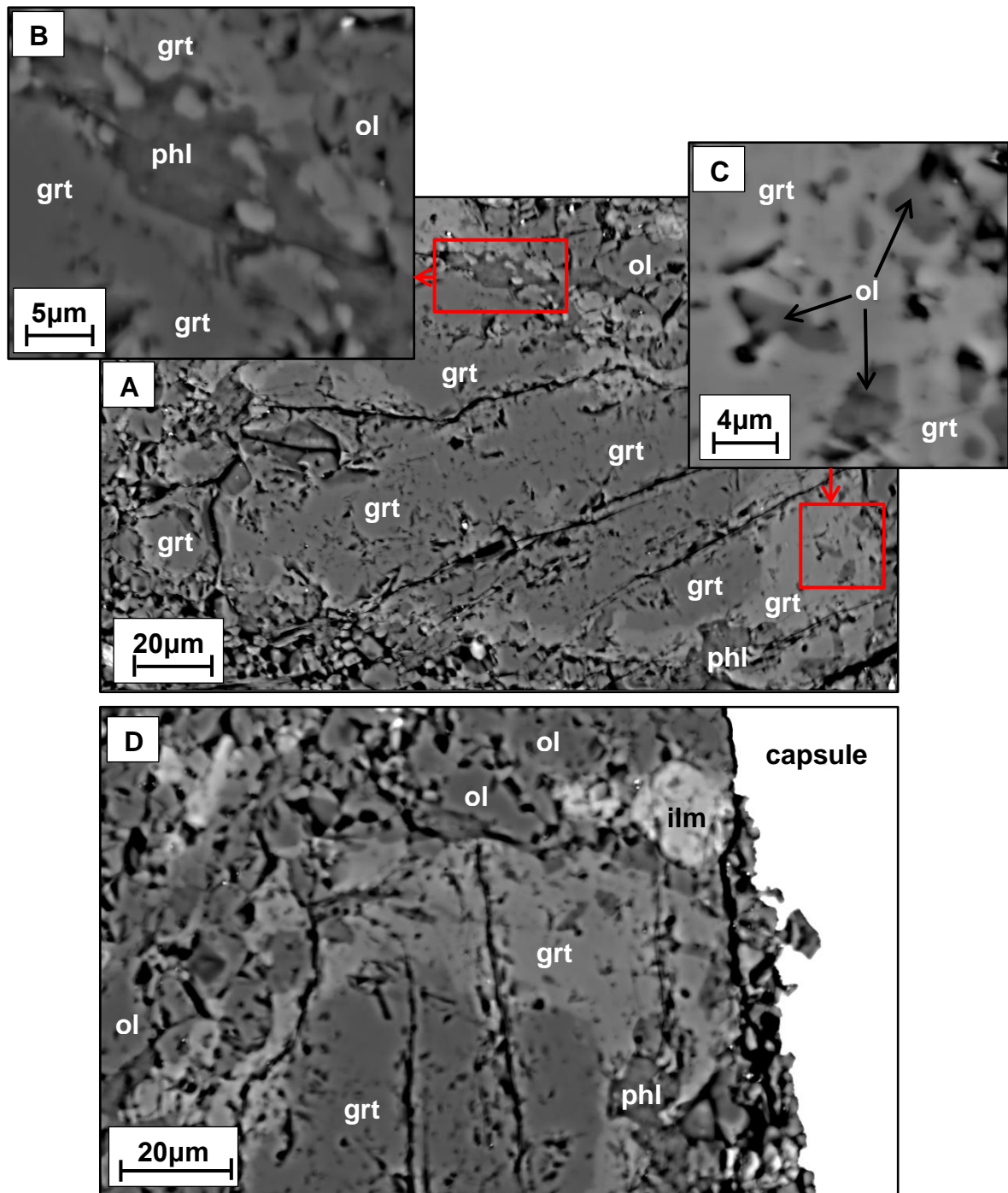


Figure A.6: Back-scattered electron images of textural features of remnant garnet in produced in MG-09 (1100°C, 4GPa, 6hours). A: Overview of the garnet crystal.. Note the somewhat concentric zoning. B: Phlogopite occurs in what appears to be pre-existing fractures within the garnet crystal. C: Small rounded olivine inclusions. D: The lighter shade of grey in the BSE-image defines the composition that is furthest removed in compson from the original garnet grains. This composition is always located toward the edge of the garnet crystal.

Appendix 3: Electron microprobe analyses of mineral phases produced in experiments**Table A.3. Electron microprobe analyses of olivine (in wt %) produced in experiments. Mineral formulae were calculated on the basis of 4 oxygens.**

Exp	MG-01	MG-01	MG-01	MG-01	MG-01	MG-01	MG-01	MG-01	MG-01	MG-01	MG-01	MG-04	MG-04
P (GPa)	2	2	2	2	2	2	2	2	2	2	2	3	3
T (°C)	1100	1100	1100	1100	1100	1100	1100	1100	1100	1100	1100	1100	1100
Dur (hrs)	48	48	48	48	48	48	48	48	48	48	48	24	24
	Higher magnesium olivine					Lower magnesium olivine							
SiO ₂	39.6	39.7	39.6	39.9	39.1	39.5	39.5	39.6	39.3	39.2		40.5	40.2
Cr ₂ O ₃	-	-	-	-	-	-	-	-	-	-		-	-
FeO	14.6	14.3	14.3	14.7	15.6	15.7	15.6	15.9	17.4	17.0		12.2	11.5
MnO	0.2	0.3	0.2	0.3	0.4	0.3	0.3	0.3	0.4	0.3		-	-
MgO	44.9	45.2	45.2	44.7	44.1	43.9	43.9	44.1	43.1	43.0		47.3	47.4
CaO	0.2	0.2	0.2	0.2	0.2	0.3	0.3	0.2	0.3	0.2		-	0.2
NiO	-	0.2	0.3	0.2	0.2	-	0.3	0.2	-	0.2		0.2	0.3
Total	99.5	99.9	99.9	100.0	99.6	99.7	99.8	100.3	100.5	100.0		100.3	99.7
xO ²⁻	4	4	4	4	4	4	4	4	4	4		4	4
Si	1.00	1.00	1.00	1.00	0.99	1.00	1.00	1.00	1.00	0.99		1.00	1.00
Cr	-	-	-	-	-	-	-	-	-	-		-	-
Fe ²⁺	0.31	0.30	0.30	0.31	0.33	0.33	0.33	0.33	0.37	0.36		0.25	0.24
Mn	0.01	0.01	0.00	0.01	0.01	0.01	0.01	0.01	0.01	0.01		-	-
Mg	1.69	1.69	1.69	1.67	1.66	1.66	1.66	1.66	1.63	1.62		1.74	1.75
Ca	0.01	0.01	0.01	0.00	0.01	0.01	0.01	0.01	0.01	0.01		0.00	0.01
Ni	-	0.00	0.01	0.00	0.00	-	0.01	0.00	-	0.00		0.00	0.01
ΣCations	3.00	3.00	3.00	3.00	3.00	3.00	3.00	3.00	3.00	3.00		3.00	3.00
Mg#	85	85	85	84	83	83	83	83	82	82		87	88

Table A.3. continued

Exp	MG-04	MG-04	MG-04	MG-05	MG-05	MG-05	MG-05	MG-05	MG-05	MG-05	MG-05	MG-05
P (GPa)	3	3	3	3	3	3	3	3	3	3	3	3
T (°C)	1100	1100	1100	1200	1200	1200	1200	1200	1200	1200	1200	1200
Dur (hrs)	24	24	24	24	24	24	24	24	24	24	24	24
										Garnet included olivine		
SiO ₂	40.3	40.7	40.9	41.0	40.3	40.6	40.5	40.9	40.9	40.8	40.9	41.1
Cr ₂ O ₃	-	-	-	-	-	-	-	-	0.2	0.1	-	-
FeO	11.6	11.3	10.9	11.0	11.6	11.1	11.8	10.5	10.2	10.3	10.1	9.2
MnO	0.2	-	-	-	-	-	-	-	-	-	-	-
MgO	47.7	47.7	47.8	47.9	47.2	47.8	47.8	48.1	48.7	47.9	48.4	49.8
CaO	0.1	-	-	0.2	0.2	0.1	0.1	0.2	0.1	0.6	0.1	0.2
NiO	0.3	0.3	0.2	-	0.2	0.2	-	0.2	-	-	-	-
Total	100.3	100.0	99.8	100.1	99.6	99.9	100.3	99.9	100.1	99.7	99.5	100.2
xO ²⁻	4	4	4	4	4	4	4	4	4	4	4	4
Si	1.00	1.00	1.01	1.01	1.00	1.00	1.00	1.01	1.00	1.00	1.01	1.00
Cr	-	-	-	-	-	-	-	-	0.00	0.00	-	-
Fe ²⁺	0.24	0.23	0.22	0.23	0.24	0.23	0.24	0.22	0.21	0.21	0.21	0.19
Mn	0.00	-	-	-	-	-	-	-	-	-	-	-
Mg	1.75	1.75	1.76	1.75	1.75	1.76	1.76	1.76	1.78	1.75	1.78	1.81
Ca	0.00	-	-	0.01	0.01	0.00	0.00	0.00	0.00	0.02	0.00	0.00
Ni	0.01	0.01	0.00	-	0.00	0.00	-	-	-	-	-	-
ΣCations	3.00	3.00	2.99	2.99	3.00	3.00	3.00	2.99	3.00	2.98	2.99	3.00
Mg#	88	88	89	89	88	88	88	89	90	89	90	91

Table A.3. continued

Exp	MG-05	MG-07	MG-07	MG-07	MG-07	MG-07	MG-07	MG-07	MG-07	MG-07	MG-08	MG-08	MG-08
P (GPa)	3	4	4	4	4	4	4	4	4	4	4	4	4
T (°C)	1200	1100	1100	1100	1100	1100	1100	1100	1100	1100	1200	1200	1200
Dur (hrs)	24	24	24	24	24	24	24	24	24	24	24	24	24
	Garnet included olivine									Garnet included olivine			
SiO ₂	40.3	40.2	40.2	40.2	40.1	39.8	40.6	40.9	41.0	40.6	40.4	40.5	
Cr ₂ O ₃	0.2	-	-	-	-	-	-	-	-	-	-	-	-
FeO	10.2	13.3	12.7	13.1	12.0	12.8	11.6	10.8	10.7	11.5	11.9	11.5	
MnO	-	-	-	-	-	-	-	-	-	-	0.2	0.2	
MgO	48.8	46.1	46.9	46.6	47.6	47.1	47.8	48.3	48.1	47.6	47.3	47.5	
CaO	0.2	0.2	0.2	-	0.1	0.2	0.1	0.2	0.2	-	-	-	
NiO		-	-	-	-	-	-	-	-	-	-	-	
Total	99.8	99.9	99.9	99.9	99.8	99.8	100.1	100.3	99.9	99.7	99.9	99.6	
xO ²⁻	4	4	4	4	4	4	4	4	4	4	4	4	
Si	0.99	1.00	1.00	1.00	0.99	0.99	1.00	1.00	1.00	1.00	1.00	1.00	
Cr	0.00	-	-	-	-	-	-	-	0.00	-	-	-	
Fe ²⁺	0.21	0.28	0.26	0.27	0.25	0.27	0.24	0.22	0.22	0.24	0.25	0.24	
Mn	-	-	-	-	-	-	-	-	-	-	-	-	
Mg	1.79	1.71	1.74	1.73	1.76	1.75	1.75	1.76	1.75	1.75	1.75	1.75	
Ca	0.01	0.01	0.00	-	0.00	0.00	0.00	0.00	0.01	-	-	-	
Ni	-	-	-	-	-	-	-	-	-	-	-	-	
ΣCations	3.00	3.00	3.00	3.00	3.01	3.01	3.00	2.99	2.98	3.00	3.00	3.00	
Mg#	90	86	87	86	88	87	88	89	89	88	88	88	

Table A.3. continued

Exp	MG-08	MG-08	MG-09	MG-09	MG-09	MG-09	MG-09
P (GPa)	4	4	4	4	4	4	4
T (°C)	1200	1200	1100	1100	1100	1100	1100
Dur (hrs)	24	24	6	6	6	6	6
SiO ₂	40.8	40.8	39.2	39.5	40.0	40.0	39.8
Cr ₂ O ₃	-	-	-	-	-	-	-
FeO	12.0	11.5	12.5	12.6	12.4	10.9	12.1
MnO	-	-	-	-	-	-	-
MgO	47.4	47.9	46.8	47.3	47.6	48.4	45.8
CaO	-	-	0.8	0.5	0.4	0.8	2.3
NiO	-	-	0.2	0.2	-	0.2	-
Total	100.2	100.2	99.5	100.1	100.3	100.3	100.0
xO ²⁻	4	4	4	4	4	4	4
Si	1.00	1.00	0.98	0.98	0.99	0.98	0.99
Cr	-	-	-	-	-	-	-
Fe ²⁺	0.25	0.24	0.26	0.26	0.26	0.22	0.25
Mn	-	-	-	-	-	-	-
Mg	1.74	1.76	1.75	1.76	1.76	1.78	1.70
Ca	-	-	0.02	0.01	0.01	0.02	0.06
Ni	-	-	0.00	0.00	-	0.00	-
ΣCations	3.00	3.00	3.02	3.02	3.01	3.01	3.00
Mg#	88	88	87	87	87	89	87

Table A .4. Electron microprobe analyses of clinopyroxene (in wt %) produced in the experiments. Mineral formulae were calculated on the basis of 6 oxygens, and Fe³⁺ was calculated according to Droop (1987).

Exp	MG-01	MG-01	MG-01	MG-01	MG-01	MG-04	MG-04	MG-04	MG-04	MG-04	MG-05	MG-05
P (GPa)	2	2	2	2	2	3	3	3	3	3	3	3
T (°C)	1100	1100	1100	1100	1100	1100	1100	1100	1100	1100	1200	1200
Dur (hrs)	48	48	48	48	48	24	24	24	24	24	24	24
SiO ₂	47.9	48.5	49.9	52.1	50.3	53.6	53.3	54.2	53.4	53.5	52.5	53.2
TiO ₂	1.9	1.5	1.0	0.7	0.7	0.4	0.5	0.3	0.4	0.4	0.6	0.5
Al ₂ O ₃	7.1	7.6	7.3	3.6	6.5	1.2	2.0	1.1	1.7	1.9	3.4	2.8
Cr ₂ O ₃	0.4	0.2	1.4	0.8	1.4	0.8	0.9	0.6	0.6	0.5	0.7	0.5
Fe ₂ O ₃	-	-	-	-	-	-	-	-	-	-	0.3	0.1
FeO	3.5	4.0	4.7	3.8	4.6	3.4	4.4	3.4	3.3	3.7	2.9	2.9
MnO	-	-	0.3	-	0.2	-	-	-	-	-	-	0.2
MgO	14.5	15.4	17.5	17.5	17.8	18.0	18.0	18.6	18.0	17.5	17.4	18.4
CaO	24.8	21.6	18.0	21.4	18.7	22.4	20.8	22.3	22.8	22.9	22.2	21.4
Na ₂ O	-	-	-	-	-	-	-	-	-	-	0.2	0.2
K ₂ O	-	1.6	-	-	-	-	-	-	-	-	-	-
Total	100.0	100.3	100.1	99.9	100.1	99.7	99.9	100.5	100.1	100.3	100.1	100.31
xO ²⁻	6	6	6	6	6	6	6	6	6	6	6	6
Si	1.77	1.77	1.81	1.90	1.82	1.96	1.94	1.96	1.94	1.94	1.90	1.92
Ti	0.05	0.04	0.03	0.02	0.02	0.01	0.01	0.01	0.01	0.01	0.02	0.01
Al	0.31	0.32	0.31	0.15	0.28	0.05	0.09	0.05	0.07	0.08	0.15	0.12
Cr	0.01	0.01	0.04	0.02	0.04	0.02	0.03	0.02	0.02	0.01	0.02	0.01
Fe ³⁺	-	-	-	-	-	-	-	-	-	-	0.01	0.00
Fe ²⁺	0.11	0.12	0.14	0.11	0.14	0.10	0.13	0.10	0.10	0.11	0.09	0.09
Mn	-	-	0.01	0.00	0.01	-	-	-	-	-	-	0.01
Mg	0.79	0.83	0.95	0.95	0.96	0.98	0.98	1.00	0.98	0.95	0.94	0.99
Ca	0.98	0.84	0.70	0.84	0.73	0.88	0.81	0.87	0.89	0.89	0.86	0.83
Na	-	-	-	-	-	-	-	-	-	-	0.01	0.01
K	-	0.08	-	-	-	-	-	-	-	-	-	-
ΣCations	4.02	4.01	3.99	3.99	4.00	4.00	3.99	4.00	4.00	4.00	4.00	4.00
Mg#	88	87	87	89	87	91	88	91	91	89	91	92

Table A.4. continued

Exp	MG-05	MG-05	MG-05	MG-07	MG-07	MG-07	MG-07	MG-07	MG-07	MG-07	MG-07	MG-07	MG-07
P (GPa)	3	3	3	4	4	4	4	4	4	4	4	4	4
T (°C)	1200	1200	1200	1100	1100	1100	1100	1100	1100	1100	1100	1100	1100
Dur (hrs)	24	24	24	24	24	24	24	24	24	24	24	24	24
										Garnet included clinopyroxene			
SiO ₂	52.7	52.0	52.5	53.7	53.9	53.4	54.2	53.6	53.0	53.8	51.9	52.0	50.2
TiO ₂	0.5	0.6	0.5	0.3	0.2	0.4	0.3	0.2	0.6	0.4	0.6	0.9	0.8
Al ₂ O ₃	2.9	3.4	3.2	1.7	1.8	1.3	1.6	1.6	3.2	1.8	5.7	4.9	6.8
Cr ₂ O ₃	0.6	0.8	0.7	0.6	0.4	0.6	0.3	0.6	0.6	0.6	0.9	1.0	1.2
Fe ₂ O ₃	0.1	0.1	-	0.4	-	0.3	-	0.2	-	-	-	-	-
FeO	3.1	2.9	3.1	3.5	3.4	3.3	3.5	3.4	3.4	3.0	3.8	3.9	4.6
MnO	0.2	0.2	-	-	-	-	-	-	-	-	-	-	-
MgO	17.4	17.1	17.0	18.9	17.9	17.8	17.7	17.6	18.1	17.5	18.0	17.8	17.2
CaO	22.8	22.7	22.7	21.3	22.4	22.7	22.3	23.1	20.7	23.3	18.9	19.8	19.1
Na ₂ O	-	-	0.2	-	-	-	-	-	-	-	-	-	0.2
Total	100.3	99.8	99.8	100.4	99.8	99.8	99.9	100.2	99.6	100.3	99.8	100.28	100.0
xO ²⁻	6	6	6	6	6	6	6	6	6	6	6	6	6
Si	1.91	1.90	1.91	1.94	1.96	1.95	1.97	1.95	1.92	1.95	1.87	1.88	1.82
Ti	0.01	0.02	0.01	0.01	0.01	0.01	0.01	0.01	0.02	0.01	0.02	0.02	0.02
Al	0.12	0.14	0.14	0.07	0.08	0.06	0.07	0.07	0.14	0.08	0.24	0.21	0.29
Cr	0.02	0.02	0.02	0.02	0.01	0.02	0.01	0.02	0.02	0.02	0.02	0.03	0.03
Fe ³⁺	0.00	0.00	-	0.01	-	0.01	-	0.00	-	-	-	-	-
Fe ²⁺	0.10	0.09	0.09	0.11	0.10	0.10	0.11	0.10	0.10	0.09	0.12	0.12	0.14
Mn	0.00	0.01	-	-	-	-	-	-	-	-	-	-	-
Mg	0.94	0.93	0.93	1.02	0.97	0.97	0.96	0.95	0.98	0.95	0.97	0.96	0.93
Ca	0.88	0.89	0.88	0.83	0.87	0.89	0.87	0.90	0.81	0.90	0.73	0.76	0.74
Na	-	-	0.01	-	-	-	-	-	-	-	-	-	0.01
ΣCations	4.00	4.00	4.00	4.00	3.99	4.00	3.99	4.00	3.98	3.99	3.98	3.98	4.00
Mg#	91	91	91	91	90	91	90	90	90	91	89	89	87

Table A.4. continued

Exp	MG-08	MG-08	MG-08	MG-08	MG-08	MG-09
P (GPa)	4	4	4	4	4	4
T (°C)	1200	1200	1200	1200	1200	1100
Dur (hrs)	24	24	24	24	24	6
SiO ₂	53.5	53.9	52.9	53.8	53.5	52.6
TiO ₂	0.3	0.3	0.4	0.4	0.3	0.4
Al ₂ O ₃	2.2	2.0	2.2	2.1	2.1	2.4
Cr ₂ O ₃	1.0	0.7	1.1	0.9	0.8	0.5
Fe ₂ O ₃	-	-	-	-	-	-
FeO	3.1	3.1	3.1	3.2	3.1	3.0
MnO	-	0.2	-	-	-	-
MgO	17.2	18.0	17.0	17.2	17.9	18.7
CaO	22.9	21.6	22.9	22.2	21.8	22.9
Na ₂ O	0.2	0.2	0.2	0.2	0.2	-
Total	100.4	100.0	99.7	100.1	99.7	100.5
xO ²⁻	6	6	6	6	6	6
Si	1.94	1.95	1.93	1.95	1.95	1.91
Ti	0.01	0.01	0.01	0.01	0.01	0.01
Al	0.09	0.09	0.09	0.09	0.09	0.10
Cr	0.03	0.02	0.03	0.03	0.02	0.01
Fe ³⁺	-	-	-	-	-	-
Fe ²⁺	0.09	0.09	0.09	0.10	0.09	0.09
Mn	-	0.01	-	-	-	-
Mg	0.93	0.97	0.92	0.93	0.97	1.01
Ca	0.89	0.84	0.90	0.86	0.85	0.89
Na	0.02	0.01	0.01	0.02	0.01	-
K	-	-	-	-	-	-
ΣCations	4.00	3.99	4.00	3.99	4.00	4.02
Mg#	91	91	91	90	91	92

Table A.5. Electron microprobe analyses of phlogopite (in wt %) produced in the experiments. Mineral formulae were calculated on the basis of 24 oxygens (Σ O, OH, F, Cl)

Exp	MG-01	MG-01	MG-01	MG-01	MG-01	MG-04	MG-04	MG-04	MG-04	MG-04	MG-05	MG-05	MG-05
P (GPa)	2	2	2	2	2	3	3	3	3	3	3	3	3
T (°C)	1100	1100	1100	1100	1100	1100	1100	1100	1100	1100	1200	1200	1200
Dur(hrs)	48	48	48	48	48	24	24	24	24	24	24	24	24
SiO ₂	38.7	38.6	38.0	38.9	38.8	39.8	41.2	39.5	40.4	39.9	39.7	39.1	39.8
TiO ₂	1.2	1.2	1.3	1.2	1.3	1.5	1.7	2.1	1.6	2.0	1.6	1.9	2.2
Al ₂ O ₃	17.6	17.7	17.6	17.6	17.5	14.1	13.8	14.7	14.3	14.9	15.7	15.2	15.7
Cr ₂ O ₃	-	-	-	-	-	1.2	1.0	0.9	1.2	1.2	1.6	1.2	1.2
FeO	5.7	6.0	6.0	6.0	5.7	4.2	3.9	4.1	4.1	4.0	4.0	4.1	3.7
MgO	22.1	22.1	22.0	22.1	22.1	22.7	23.5	22.7	22.6	22.5	22.6	22.0	22.5
CaO	-	0.1	0.1	0.1	0.1	-	-	-	-	-	-	-	-
Na ₂ O	0.3	0.3	0.2	0.3	0.2	-	-	-	-	-	-	-	-
K ₂ O	9.6	9.5	9.5	9.6	9.6	10.1	10.2	10.2	10.4	10.3	10.0	10.2	10.1
F	1.6	1.2	0.9	1.7	1.0	1.2	1.1	1.1	1.0	-	1.8	1.4	1.4
Total	96.1	96.1	95.3	96.7	96.0	94.3	96.0	94.9	95.2	94.8	96.1	94.5	96.1
xO ²⁻	24	24	24	24	24	24	24	24	24	24	24	24	24
Si	5.91	5.91	5.81	5.90	5.88	6.28	6.50	6.24	6.38	6.30	5.80	5.72	5.81
Ti	0.14	0.13	0.15	0.14	0.15	0.18	0.20	0.25	0.19	0.24	0.18	0.21	0.24
Al	3.17	3.20	3.18	3.15	3.13	2.61	2.58	2.73	2.66	2.77	2.71	2.63	2.71
Cr	-	-	-	-	-	0.15	0.12	0.12	0.15	0.15	0.19	0.14	0.14
Fe ²⁺	0.73	0.76	0.77	0.76	0.73	0.56	0.51	0.54	0.55	0.53	0.49	0.50	0.45
Mg	5.04	5.05	5.02	4.99	5.00	5.34	5.53	5.34	5.32	5.29	4.94	4.80	4.91
Ca	-	0.02	0.02	0.02	0.02	-	-	-	-	-	-	-	-
Na	0.08	0.08	0.06	0.07	0.06	-	-	-	-	-	-	-	-
K	1.88	1.84	1.85	1.86	1.86	2.04	2.06	2.05	2.09	2.08	1.86	1.91	1.89
F	0.76	0.57	0.42	0.82	0.49	0.58	0.57	0.55	0.49	-	0.81	0.66	0.66
Σ Cations	17.72	17.57	17.28	17.71	17.33	17.74	18.07	17.82	17.82	17.35	16.96	16.55	16.82
Mg#	87	87	87	87	87	91	91	91	91	91	91	91	92

Table A.5. continued

Exp	MG-05	MG-05	MG-07	MG-07	MG-07	MG-07	MG-07	MG-08	MG-08	MG-08	MG-08	MG-08	MG-09
P (GPa)	3	3	4	4	4	4	4	4	4	4	4	4	4
T (°C)	1200	1200	1100	1100	1100	1100	1100	1200	1200	1200	1200	1200	1100
Dur(hrs)	24	24	24	24	24	24	24	24	24	24	24	24	6
SiO ₂	39.2	39.9	40.6	41.5	40.5	40.6	40.6	40.3	40.4	40.3	40.4	41.2	39.1
TiO ₂	2.4	2.2	1.1	1.0	1.1	1.3	1.0	1.4	1.6	1.5	1.5	1.3	1.0
Al ₂ O ₃	14.9	15.7	14.0	13.3	13.9	13.9	14.0	14.2	14.2	14.3	14.0	14.0	15.0
Cr ₂ O ₃	1.3	1.2	0.8	0.6	0.8	0.7	0.6	0.9	0.8	0.9	1.2	0.7	0.4
FeO	3.6	3.7	4.2	4.2	4.2	4.1	4.1	4.1	4.0	4.3	4.3	4.0	4.1
MgO	22.0	22.6	23.1	22.7	23.5	23.1	23.4	23.1	23.0	22.8	23.4	23.4	24.3
CaO	-	-	0.2	2.5	0.2	0.3	0.2	0.1	0.2	-	0.2	0.2	1.1
Na ₂ O	-	-	0.4	0.2	0.2	0.2	0.3	-	-	-	-	-	-
K ₂ O	10.1	10.2	10.2	9.2	9.8	10.2	10.0	10.2	10.2	10.6	9.9	9.9	9.2
F	1.4	1.4	1.5	1.2	1.4	1.6	1.6	1.2	1.2	1.4	1.4	1.2	2.3
Total	94.3	96.3	95.3	95.9	95.0	95.2	95.2	95.0	95.0	95.3	95.6	95.3	95.6
xO ²⁻	24	24	24	24	24	24	24	24	24	24	24	24	24
Si	5.73	5.84	6.25	6.39	6.23	6.26	6.26	6.13	6.15	6.13	6.15	6.27	6.19
Ti	0.27	0.24	0.13	0.12	0.13	0.15	0.12	0.16	0.18	0.17	0.17	0.14	0.11
Al	2.57	2.71	2.54	2.42	2.53	2.52	2.54	2.54	2.55	2.56	2.50	2.50	2.80
Cr	0.16	0.14	0.09	0.08	0.09	0.09	0.07	0.11	0.09	0.11	0.14	0.09	0.05
Fe ²⁺	0.44	0.45	0.54	0.54	0.54	0.53	0.53	0.53	0.50	0.55	0.54	0.51	0.55
Mg	4.79	4.94	5.30	5.20	5.40	5.31	5.38	5.23	5.21	5.16	5.30	5.30	5.73
Ca	-	-	0.04	0.41	0.03	0.04	0.03	0.02	0.02	-	0.03	0.03	0.19
Na	-	-	0.11	0.07	0.06	0.06	0.09	-	-	-	-	-	-
K	1.89	1.91	2.00	1.81	1.93	2.00	1.97	1.98	1.99	2.05	1.93	1.93	1.87
F	0.62	0.63	0.71	0.58	0.68	0.75	0.78	0.60	0.56	0.68	0.68	0.60	1.16
ΣCations	16.47	16.84	17.71	17.61	17.63	17.71	17.78	17.30	17.26	17.40	17.44	17.36	18.65
Mg#	92	92	91	91	91	91	91	91	91	90	91	91	91

Table A.5. continued

Exp	MG-09	MG-09	MG-09	MG-09
P (GPa)	4	4	4	4
T (°C)	1100	1100	1100	1100
Dur(hrs)	6	6	6	6
SiO ₂	39.7	39.7	38.9	39.1
TiO ₂	1.2	0.8	1.0	1.0
Al ₂ O ₃	13.7	12.8	15.8	12.1
Cr ₂ O ₃	0.2	-	0.8	0.2
FeO	4.6	4.3	4.1	5.5
MgO	24.9	24.3	24.1	25.3
CaO	0.4	0.5	0.2	0.2
Na ₂ O	-	0.2	-	-
K ₂ O	9.5	9.7	9.8	9.0
F	1.8	2.2	2.2	2.2
Total	95.3	93.6	95.9	93.7
xO ²⁻	24	24	24	24
Si	6.29	6.28	6.16	6.20
Ti	0.15	0.10	0.12	0.12
Al	2.56	2.40	2.96	2.25
Cr	0.03	-	0.10	0.03
Fe ²⁺	0.61	0.57	0.54	0.73
Mg	5.88	5.74	5.70	5.97
Ca	0.07	0.09	0.03	0.04
Na	-	0.06	-	-
K	1.92	1.97	1.97	1.82
F	0.91	1.08	1.11	1.10
ΣCations	18.40	18.28	18.68	18.26
Mg#	91	91	91	89

Table A. 6. Electron microprobe analyses of garnet (in wt %). Mineral formulae were calculated on the basis of 12 oxygens, and Fe³⁺ was calculated according to Droop (1987). XPy, XAlm, and XGrss calculated as defined by Deer, Howie & Zussman (1992)

Exp	-	-	-	-	-	MG-05	MG-05	MG-05	MG-05
P (Gpa)	-	-	-	-	-	3	3	3	3
T (°C)	-	-	-	-	-	1200	1200	1200	1200
Dur (hrs)	-	-	-	-	-	24	24	24	24
	Peridotite garnet xenocrysts					Garnet composition furthest removed from garnet xenocrysts			
SiO ₂	42.2	42.0	42.2	42.1	41.7	41.5	41.0	40.9	41.0
TiO ₂	0.3	0.3	0.3	0.2	0.3	1.0	0.9	0.9	1.1
Al ₂ O ₃	21.4	21.2	21.5	21.3	21.4	20.0	20.2	20.0	19.5
Cr ₂ O ₃	3.2	3.2	3.2	3.1	3.2	3.7	3.9	4.0	4.3
Fe ₂ O ₃	-	0.3	-	-	0.4	-	-	0.4	-
FeO	7.4	7.1	7.3	7.2	6.9	7.6	7.5	7.4	7.9
MnO	0.5	0.4	0.3	0.6	0.5	0.4	0.4	0.6	0.5
MgO	20.5	20.6	20.6	20.4	20.6	16.8	17.6	17.2	16.2
CaO	4.9	4.9	4.7	4.8	4.7	9.2	8.1	8.7	9.8
Total	100.3	100.0	100.1	99.7	99.7	100.2	99.7	100.0	100.2
xO ²⁻	12	12	12	12	12	12	12	12	12
Si	3.00	3.00	3.00	3.01	2.98	3.00	2.98	2.97	2.99
Ti	0.01	0.02	0.01	0.01	0.02	0.05	0.05	0.05	0.06
Al	1.79	1.78	1.80	1.79	1.80	1.71	1.73	1.71	1.68
Cr	0.18	0.18	0.18	0.18	0.18	0.21	0.22	0.23	0.25
Fe ³⁺	-	0.02	-	-	0.02	-	-	0.02	-
Fe ²⁺	0.44	0.42	0.44	0.43	0.41	0.46	0.46	0.45	0.48
Mn	0.03	0.03	0.02	0.04	0.03	0.02	0.03	0.03	0.03
Mg	2.17	2.19	2.19	2.17	2.19	1.81	1.91	1.86	1.75
Ca	0.37	0.37	0.36	0.37	0.36	0.71	0.63	0.68	0.76
ΣCations	8.00	8.00	7.99	8.00	8.00	7.98	8.00	8.00	7.99
Mg#	82	83	83	82	83	80	81	81	79
XPy	71.94	72.83	72.98	72.14	73.20	60.20	63.17	61.66	58.01
XGrss	3.45	2.38	2.93	3.42	2.09	12.85	9.70	9.86	12.68
XAlm	14.65	13.96	14.57	14.31	13.68	15.31	15.09	14.76	15.80

Table A.6. continued

Exp	MG-05	MG-05	MG-05	MG-05	MG-05	MG-05	MG-05	MG-05	MG-05	MG-05	MG-05	MG-05	MG-07
P (GPa)	3	3	3	3	3	3	3	3	3	3	3	3	4
T (°C)	1200	1200	1200	1200	1200	1200	1200	1200	1200	1200	1200	1200	1100
Dur (hrs)	24	24	24	24	24	24	24	24	24	24	24	24	24
		Intermediary garnet composition					Garnet composition closest in composition to garnet xenocrysts						
SiO ₂	41.2	41.3	41.6	41.4	41.8	41.8	42.2	41.7	41.8	42.4	41.7	41.7	40.8
TiO ₂	1.0	0.6	0.5	0.6	0.7	0.8	0.3	0.4	0.4	0.4	0.5	0.5	1.4
Al ₂ O ₃	20.1	21.0	21.1	20.9	21.7	21.1	21.6	21.2	21.2	21.4	21.4	21.4	20.2
Cr ₂ O ₃	3.9	3.5	3.0	3.0	2.7	3.1	3.2	3.0	3.5	3.2	3.1	3.1	2.9
Fe ₂ O ₃	-	-	-	-	-	-	-	-	1.1	-	-	-	-
FeO	7.6	7.9	7.5	7.8	7.6	7.6	7.7	7.6	6.7	7.5	7.7	7.7	8.7
MnO	0.6	0.5	0.4	0.4	0.4	0.4	0.3	0.4	0.3	0.3	0.3	0.3	0.5
MgO	17.1	17.8	18.4	18.2	18.2	18.4	19.8	19.6	20.0	19.9	19.3	19.3	16.4
CaO	8.7	7.4	7.2	7.3	7.1	7.3	5.7	5.8	6.0	5.7	5.8	5.8	9.0
Total	100.2	99.8	99.8	99.6	100.1	100.5	100.7	99.7	100.8	100.9	99.9	99.9	100.0
xO ²⁻	12	12	12	12	12	12	12	12	12	12	12	12	12
Si	2.98	2.98	3.00	2.99	2.99	2.99	3.00	2.99	2.97	3.00	2.99	2.99	2.97
Ti	0.05	0.03	0.03	0.03	0.04	0.04	0.01	0.02	0.02	0.02	0.02	0.02	0.07
Al	1.71	1.78	1.79	1.78	1.83	1.78	1.80	1.79	1.77	1.79	1.81	1.81	1.73
Cr	0.22	0.20	0.17	0.17	0.15	0.18	0.18	0.17	0.19	0.18	0.18	0.18	0.17
Fe ³⁺	-	-	-	-	-	-	-	-	0.06	-	-	-	-
Fe ²⁺	0.46	0.47	0.45	0.47	0.45	0.46	0.45	0.46	0.39	0.45	0.46	0.46	0.53
Mn	0.04	0.03	0.03	0.02	0.02	0.02	0.02	0.02	0.02	0.02	0.02	0.02	0.03
Mg	1.84	1.92	1.97	1.96	1.95	1.96	2.09	2.10	2.12	2.10	2.06	2.06	1.79
Ca	0.68	0.57	0.56	0.57	0.54	0.56	0.44	0.45	0.45	0.43	0.45	0.45	0.70
ΣCations	7.99	7.99	8.00	8.00	7.98	7.99	8.00	8.00	8.00	7.99	7.99	7.99	8.00
Mg#	80	80	81	81	81	81	82	82	84	83	82	82	77
XPy	61.03	64.09	65.51	64.93	65.62	65.31	69.72	69.38	71.09	70.15	68.94	68.94	58.59
XGrss	11.00	9.23	9.98	10.24	10.78	9.86	5.58	6.05	2.72	5.31	6.09	6.09	14.33
XAlm	15.33	15.84	15.06	15.55	15.25	15.17	15.11	15.10	13.08	14.87	15.46	15.46	17.42

Table A.6. continued

Exp	MG-07	MG-07	MG-07	MG-07	MG-07	MG-07	MG-07	MG-07	MG-07	MG-07	MG-09	MG-09	MG-09
P (GPa)	4	4	4	4	4	4	4	4	4	4	4	4	4
T (°C)	1100	1100	1100	1100	1100	1100	1100	1100	1100	1100	1100	1100	1100
Dur (hrs)	24	24	24	24	24	24	24	24	24	24	6	6	6
	Garnet composition furthest removed from garnet xenocrysts				Garnet composition closest in composition to garnet xenocrysts					Garnet composition furthest removed from garnet xenocrysts			
SiO ₂	40.7	41.0	40.8	40.7	42.0	41.7	42.1	42.4	41.8	39.7	39.7	39.3	
TiO ₂	1.8	1.3	1.2	1.4	0.6	0.5	0.3	0.4	0.6	2.4	2.7	2.8	
Al ₂ O ₃	20.4	20.3	20.8	20.3	21.6	21.4	21.5	21.4	21.3	17.7	17.2	17.3	
Cr ₂ O ₃	2.9	3.5	3.0	3.5	3.2	3.3	3.2	3.0	3.1	3.7	4.2	4.3	
Fe ₂ O ₃	-	-	-	-	-	-	0.1	-	-	0.1	0.1	-	
FeO	8.6	8.1	8.6	8.3	7.4	7.5	7.5	7.1	7.3	7.6	7.2	7.5	
MnO	0.4	0.4	0.4	0.5	0.5	0.2	0.3	0.3	0.3	0.4	0.5	0.5	
MgO	16.4	17.3	16.7	16.6	20.2	20.3	20.2	20.6	20.2	9.6	9.2	9.0	
CaO	8.9	8.1	8.4	8.5	5.0	4.9	5.2	4.8	5.2	19.2	20.1	19.6	
Total	100.0	99.0	99.9	99.7	100.4	99.7	100.6	100.0	99.9	100.4	100.8	100.3	
xO ²⁻	12	12	12	12	12	12	12	12	12	12	12	12	
Si	2.96	2.97	2.97	2.96	2.98	2.98	2.99	3.01	2.99	2.97	2.97	2.96	
Ti	0.10	0.07	0.06	0.08	0.03	0.03	0.02	0.02	0.03	0.14	0.15	0.16	
Al	1.75	1.74	1.78	1.75	1.81	1.81	1.80	1.79	1.79	1.56	1.52	1.53	
Cr	0.17	0.20	0.17	0.20	0.18	0.19	0.18	0.17	0.18	0.22	0.25	0.25	
Fe ³⁺	-	-	-	-	-	-	0.01	-	-	0.01	0.00	-	
Fe ²⁺	0.52	0.49	0.52	0.51	0.44	0.45	0.45	0.42	0.44	0.47	0.45	0.47	
Mn	0.02	0.02	0.03	0.03	0.03	0.01	0.02	0.02	0.02	0.02	0.03	0.03	
Mg	1.77	1.87	1.81	1.81	2.14	2.16	2.14	2.19	2.15	1.07	1.02	1.00	
Ca	0.69	0.63	0.65	0.66	0.38	0.37	0.40	0.37	0.40	1.54	1.61	1.58	
ΣCations	7.99	7.99	7.99	7.99	7.99	8.00	8.00	7.99	8.00	8.00	8.00	7.99	
Mg#	77	79	78	78	83	83	83	84	83	69	69	68	
XPy	58.87	62.17	60.17	60.17	71.59	72.21	71.26	72.99	71.48	34.34	32.79	32.52	
XGrss	14.32	10.64	13.17	11.90	3.79	3.14	3.70	3.92	4.38	37.62	38.28	37.88	
XAlm	17.40	16.27	17.29	16.87	14.64	14.88	14.86	14.11	14.55	15.23	14.50	15.24	

Table A.6. continued

Exp	MG-09	MG-09	MG-09	MG-09	MG-09	MG-09	MG-09	
P (GPa)	4	4	4	4	4	4	4	
T (°C)	1100	1100	1100	1100	1100	1100	1100	
Dur (hrs)	6	6	6	6	6	6	6	
			Garnet composition closest in composition to garnet xenocrysts					
SiO ₂	40.1	39.4	41.9	42.0	42.0	41.8	41.8	
TiO ₂	1.6	2.4	0.2	-	0.2	0.3	0.2	
Al ₂ O ₃	19.0	17.9	21.7	22.1	22.5	22.3	21.7	
Cr ₂ O ₃	3.5	3.8	2.8	2.7	2.7	2.5	2.3	
Fe ₂ O ₃	-	-	1.1	1.0	1.0	1.3	0.9	
FeO	7.8	7.3	6.1	5.5	6.0	5.3	5.9	
MnO	0.4	-	0.4	0.3	0.2	0.3	0.4	
MgO	10.7	9.4	21.2	21.4	21.4	21.8	21.1	
CaO	17.1	19.6	4.7	4.8	4.7	4.5	4.9	
Total	100.2	99.9	99.9	99.8	100.6	100.0	99.6	
xO ²⁻	12	12	12	12	12	12	12	
Si	2.98	2.96	2.98	2.97	2.96	2.95	2.98	
Ti	0.09	0.14	0.01	-	0.01	0.01	0.01	
Al	1.66	1.59	1.82	1.85	1.87	1.86	1.82	
Cr	0.21	0.22	0.16	0.15	0.15	0.14	0.16	
Fe ³⁺	-	-	-	0.05	0.05	0.07	0.05	
Fe ²⁺	0.49	0.46	0.36	0.33	0.35	0.31	0.35	
Mn	0.02	0.00	0.02	0.02	0.01	0.02	0.02	
Mg	1.19	1.05	2.24	2.27	2.24	2.29	2.24	
Ca	1.36	1.58	0.36	0.36	0.35	0.34	0.37	
ΣCations	8.00	8.00	8.00	8.00	8.00	8.00	8.00	
Mg#	71	69	86	87	86	88	86	
XPy	38.81	33.95	75.21	76.18	75.66	77.32	75.09	
XGrss	33.85	39.35	1.30	1.98	2.05	1.37	2.20	
XAlm	15.94	14.90	12.17	10.98	11.92	10.55	11.72	

Table A.7. Electron microprobe analyses of apatite (in wt %) produced in the experiments. Mineral formulae were calculated on the basis of 25 oxygens (Σ O, OH, F, Cl)

Exp	MG-01	MG-01	MG-01	MG-01	MG-01	MG-07	MG-07	MG-07	MG-07	MG-07	MG-08	MG-08	MG-08
P (GPa)	2	2	2	2	2	4	4	4	4	4	4	4	4
T (°C)	1100	1100	1100	1100	1100	1100	1100	1100	1100	1100	1200	1200	1200
Dur(hrs)	48	48	48	48	48	24	24	24	24	24	24	24	24
FeO	0.3	0.2	0.5	0.4	0.5	0.8	0.5	0.4	0.5	0.6	0.5	0.3	0.6
MgO	-	-	0.2	0.1	0.2	1.2	0.9	0.9	0.9	1.1	1.2	1.2	1.2
CaO	53.5	53.3	53.1	54.1	54.0	52.6	53.2	53.1	52.6	52.3	53.1	52.3	52.1
SrO	2.2	3.0	2.5	1.8	2.3	1.2	1.3	1.4	1.0	1.1	1.3	1.2	1.3
P ₂ O ₅	41.8	41.7	41.7	42.2	41.9	42.6	42.7	42.6	42.7	43.0	42.8	42.8	42.8
F	2.2	2.6	2.0	2.2	2.3	2.2	2.2	2.5	1.9	1.88	1.8	2.7	2.6
Total	99.0	99.7	99.1	99.9	100.1	99.6	99.8	99.8	98.8	99.2	99.8	99.4	99.4
xO ²⁻	25	25	25	25	25	25	25	25	25	25	25	25	25
Fe ²⁺	0.04	0.02	0.07	0.06	0.06	0.10	0.06	0.06	0.06	0.08	0.06	0.04	0.07
Mg	-	-	0.05	0.04	0.04	0.28	0.21	0.21	0.23	0.26	0.28	0.29	0.29
Ca	9.51	9.44	9.45	9.51	9.51	8.95	9.04	8.97	9.03	8.95	9.06	8.81	8.79
Sr	0.21	0.29	0.24	0.17	0.22	0.11	0.12	0.13	0.09	0.10	0.12	0.11	0.11
P	5.87	5.83	5.86	5.86	5.83	5.73	5.73	5.68	5.80	5.81	5.77	5.70	5.71
F	1.14	1.34	1.06	1.16	1.18	1.10	1.10	1.25	0.95	0.95	0.93	1.32	1.28
Σ Cations	16.77	16.92	16.73	16.79	16.84	16.26	16.26	16.30	16.17	16.16	16.22	16.27	16.26

Table A.7. continued

Exp	MG-08	MG-08	MG-09	MG-09	MG-09	MG-09	MG-09
P (GPa)	4	4	4	4	4	4	4
T (°C)	1200	1200	1100	1100	1100	1100	1100
Dur(hrs)	24	24	6	6	6	6	6
SiO ₂	-	-	0.6	0.6	0.6	0.6	0.5
FeO	0.6	0.7	0.3	0.3	-	0.3	0.2
MgO	1.3	1.5	0.5	0.3	-	0.2	0.2
CaO	53.9	53.1	52.8	53.1	52.9	52.8	53.2
SrO	1.1	1.2	2.5	2.7	3.1	2.5	3.0
P ₂ O ₅	41.3	41.6	41.5	40.5	40.8	41.4	41.1
F	1.2	1.6	3.2	2.3	2.9	3.1	2.5
Total	99.0	99.1	100.0	98.9	99.1	99.6	99.7
xO ²⁻	25	25	25	25	25	25	25
Si	-	-	0.10	0.10	0.10	0.10	0.08
Fe ²⁺	0.09	0.09	0.04	0.04	-	0.04	0.03
Mg	0.33	0.37	0.12	0.06	-	0.04	0.04
Ca	9.46	9.22	8.87	9.22	9.06	8.92	9.11
Sr	0.10	0.11	0.22	0.26	0.29	0.22	0.28
P	5.73	5.70	5.51	5.55	5.53	5.53	5.57
F	0.63	0.84	1.56	1.19	1.44	1.54	1.29
ΣCations	16.33	16.34	16.42	16.42	16.41	16.39	16.40

Table A.8. Electron microprobe analyses of spinel (in wt %) produced in the experiments. Mineral formulae were calculated on the basis of 4 oxygens, and Fe³⁺ was calculated according to Droop (1987)

Exp	MG-04	MG-04	MG-04	MG-04	MG-04	MG-05	MG-05
P (GPa)	3	3	3	3	3	3	3
T (°C)	1100	1100	1100	1100	1100	1200	1200
Dur (hrs)	24	24	24	24	24	24	24
						Garnet included spinel	
SiO ₂	1.1	1.6	1.4	2.8	1.8	1.5	2.0
TiO ₂	2.5	2.7	2.9	2.5	3.0	1.8	1.9
Al ₂ O ₃	24.2	23.8	19.2	17.8	17.4	29.9	29.2
Cr ₂ O ₃	39.2	38.6	41.5	41.1	42.5	33.9	34.1
Fe ₂ O ₃	2.2	1.5	3.2	3.0	3.6	2.1	1.3
FeO	15.8	16.4	18.1	16.4	16.6	12.9	13.2
MnO	0.3	0.5	0.4	0.5	0.4	-	-
MgO	14.9	14.8	13.8	15.5	15.0	17.50	17.7
CaO	-	-	-	-	-	0.53	0.6
Total	100.5	100.1	100.4	99.6	100.2	100.1	100.0
xO ²⁻	4	4	4	4	4	4	4
Si	0.03	0.05	0.04	0.09	0.05	0.04	0.06
Ti	0.06	0.06	0.07	0.06	0.07	0.04	0.04
Al	0.85	0.84	0.70	0.64	0.63	1.02	0.99
Cr	0.93	0.92	1.01	1.00	1.03	0.77	0.78
Fe ³⁺	0.05	0.03	0.07	0.07	0.08	0.05	0.03
Fe ²⁺	0.40	0.41	0.47	0.42	0.43	0.31	0.32
Mn	0.01	0.01	0.01	0.01	0.01	-	-
Mg	0.67	0.66	0.63	0.71	0.69	0.75	0.76
Ca	-	-	-	-	-	0.02	0.02
ΣCations	3.00	3.00	3.00	3.00	3.00	3.00	3.00
Mg#	63	62	58	63	62	71	70

Table A.9. Electron microprobe analyses of ilmenite (in wt %) produced in the experiments. Mineral formulae were calculated on the basis of 3 oxygens.

Exp	MG-01	MG-01	MG-01	MG-01	MG-01	MG-07	MG-07	MG-07	MG-07	MG-07	MG-08	MG-08
P (GPa)	2	2	2	2	2	4	4	4	4	4	4	4
T (°C)	1100	1100	1100	1100	1100	1100	1100	1100	1100	1100	1200	1200
Dur (hrs)	48	48	48	48	48	24	24	24	24	24	24	24
TiO ₂	52.7	51.7	51.3	52.7	53.1	51.9	52.8	52.1	51.6	51.7	53.4	53.8
Al ₂ O ₃	0.3	0.3	0.4	0.3	0.3	0.9	0.8	0.9	1.2	1.2	0.6	0.7
Cr ₂ O ₃	0.6	0.9	0.7	0.6	0.5	1.8	1.9	1.8	1.7	1.6	1.3	1.5
Nb ₂ O ₅	-	-	-	0.3	0.3	-	-	-	-	-	-	-
V ₂ O ₃	1.2	1.1	1.4	1.4	0.9	1.8	1.9	1.9	2.4	1.4	2.1	1.2
FeO	31.9	31.5	31.9	32.0	32.5	27.3	27.1	27.0	27.3	27.4	27.0	27.2
MnO	0.6	0.5	0.6	0.6	0.7	0.4	0.4	0.4	0.4	0.5	0.5	0.4
MgO	10.1	10.1	9.6	9.6	9.5	13.5	13.5	14.5	13.9	14.0	14.1	14.1
CaO	0.8	2.4	1.8	1.5	1.1	-	-	-	-	-	0.1	-
Total	98.1	98.7	98.2	99.0	99.0	97.7	98.3	98.6	98.5	97.8	99.1	98.9
xO ²⁻	3	3	3	3	3	3	3	3	3	3	3	3
Ti	0.98	0.97	0.97	0.98	0.98	0.96	0.97	0.95	0.95	0.95	0.97	0.98
Al	0.01	0.01	0.01	0.01	0.01	0.03	0.02	0.03	0.03	0.04	0.02	0.02
Cr	0.01	0.02	0.01	0.01	0.01	0.04	0.04	0.03	0.03	0.03	0.02	0.03
Nb	-	-	-	0.00	0.00	-	-	-	-	-	-	-
V	0.02	0.02	0.03	0.03	0.02	0.03	0.03	0.03	0.04	0.03	0.04	0.02
Fe ²⁺	0.67	0.67	0.68	0.67	0.68	0.57	0.56	0.56	0.56	0.57	0.55	0.56
Mn	0.02	0.02	0.02	0.02	0.03	0.02	0.01	0.01	0.01	0.02	0.02	0.01
Mg	0.27	0.27	0.26	0.25	0.25	0.36	0.35	0.38	0.36	0.37	0.36	0.37
Ca	0.01	0.04	0.03	0.02	0.02	-	-	-	-	-	0.00	-
ΣCations	2.00	2.01	2.00	2.00	2.00	1.99	1.99	2.00	2.00	2.00	1.99	1.99
Mg#	29	29	27	28	27	38	39	40	39	39	40	40

Table A.9. continued

Exp	MG-08	MG-08	MG-08	MG-09	MG-09	MG-09	MG-09	MG-09
P (GPa)	4	4	4	4	4	4	4	4
T (°C)	1200	1200	1200	1100	1100	1100	1100	1100
Dur (hrs)	24	24	24	6	6	6	6	6
TiO ₂	53.4	53.8	53.0	53.9	53.9	53.5	53.5	53.3
Al ₂ O ₃	0.6	0.7	0.9	0.5	0.6	0.7	0.5	0.6
Cr ₂ O ₃	1.3	1.5	1.9	1.5	1.2	1.4	1.4	1.3
Nb ₂ O ₅	-	-	-	-	-	-	-	0.5
V ₂ O ₃	1.2	0.7	1.1	-	1.0	1.3	1.1	1.3
FeO	27.0	27.2	27.1	29.3	29.4	29.5	29.2	29.2
MnO	0.5	0.4	0.3	0.4	0.5	0.5	0.5	0.5
MgO	14.1	14.1	14.5	12.0	12.2	12.4	12.0	12.2
CaO	-	-	-	-	0.5	-	0.5	0.4
Total	98.0	98.4	98.8	97.7	99.2	99.1	98.6	99.3
xO ²⁻	3	3	3	3	3	3	3	3
Ti	0.98	0.98	0.97	1.00	0.98	0.98	0.98	0.97
Al	0.02	0.02	0.02	0.01	0.02	0.02	0.01	0.02
Cr	0.02	0.03	0.04	0.03	0.02	0.03	0.03	0.03
Nb	-	-	-	-	-	-	-	0.01
V	0.02	0.01	0.02	-	0.02	0.02	0.02	0.02
Fe ²⁺	0.56	0.56	0.56	0.61	0.60	0.61	0.60	0.60
Mn	0.02	0.01	0.01	0.02	0.02	0.02	0.02	0.02
Mg	0.37	0.37	0.38	0.32	0.32	0.32	0.31	0.32
Ca	-	-	-	-	0.01	-	0.01	0.01
ΣCations	1.99	1.99	1.99	1.98	1.99	1.99	1.98	1.98
Mg#	40	40	40	34	34	35	34	35

Table A.10. Electron microprobe analyses of perovskite (in wt %) produced in the experiments. Mineral formulae were calculated on the basis of 4 oxygens.

Exp	MG-01	MG-01	MG-01	MG-01	MG-01
P (GPa)	2	2	2	2	2
T (°C)	1100	1100	1100	1100	1100
Dur (hrs)	48	48	48	48	48
TiO ₂	56.3	56.1	56.6	56.4	56.8
Al ₂ O ₃	0.4	0.3	0.3	0.4	0.3
Nb ₂ O ₃	0.8	1.1	0.6	0.9	0.6
FeO	0.9	0.8	0.8	0.7	0.7
CaO	39.6	39.8	40.4	40.1	39.9
Total	97.9	98.0	98.6	98.6	98.4
xO ²⁻	3	3	3	3	3
Ti	0.98	0.98	0.99	0.99	0.99
Al	0.01	0.01	0.01	0.01	0.01
Nb	0.01	0.01	0.01	0.01	0.01
Fe ²⁺	0.02	0.02	0.01	0.01	0.01
Ca	0.99	0.99	1.01	1.00	0.99
ΣCations	2.01	2.01	2.02	2.02	2.02

Appendix 4: Electron microprobe analyses of quenched melts produced in the experiments**Table A.11. Electron microprobe analyses of quenched melts (wt %; normalised to 100% anhydrous) produced in MG-01 (1100°C, 2GPa)**

SiO ₂	18.0	18.3	17.8	18.1	17.3	17.9	17.6	17.8	17.8	17.8
TiO ₂	1.8	2.0	2.4	2.0	1.6	2.0	1.9	1.8	2.0	1.9
Al ₂ O ₃	6.5	6.2	6.3	7.1	5.3	6.4	5.9	7.3	6.3	7.0
Cr ₂ O ₃	-	-	-	-	-	-	-	-	-	-
FeO	10.7	11.7	15.9	10.5	11.5	11.4	11.3	10.1	12.2	10.5
MnO	0.3	0.3	0.5	0.3	0.4	0.4	0.3	-	0.3	0.3
MgO	17.6	18.6	16.2	18.8	19.1	20.1	16.9	17.5	18.5	18.3
CaO	38.5	36.4	33.7	37.4	38.2	35.5	38.2	38.7	37.2	37.7
Na ₂ O	0.9	0.7	0.7	1.0	0.6	0.8	0.9	0.9	0.7	0.9
K ₂ O	0.5	0.2	0.4	0.6	0.2	0.3	0.5	0.6	0.4	0.5
P ₂ O ₅	3.1	2.7	3.0	2.5	2.8	2.8	4.0	3.0	2.4	2.7
F ⁻	3.8	5.	5.1	2.9	5.0	4.1	4.4	3.8	3.5	4.2
Cl ⁻	0.1	0.2	0.2	0.3	0.1	0.2	-	0.2	0.3	-
Mg#	75	74	64	76	75	76	73	76	73	76
SiO ₂ + Al ₂ O ₃	24.4	24.5	24.2	25.2	22.7	24.3	23.5	25.1	24.1	24.8
Mg/Ca (mol)	0.63	0.71	0.67	0.70	0.70	0.79	0.61	0.63	0.69	0.68

Table A.12. Electron microprobe analyses of quenched melts (in wt %; normalised to 100% anhydrous) produced in MG-04 (1100°C, 3GPa)

SiO ₂	17.9	18.3	17.9	18.0	17.7	17.43	17.3	18.2	18.0	18.2
TiO ₂	4.3	4.6	4.3	4.3	4.7	4.41	4.1	4.4	4.7	4.7
Al ₂ O ₃	4.3	4.4	4.3	4.5	4.5	4.68	4.3	4.1	4.4	4.6
Cr ₂ O ₃	-	-	-	-	-	-	0.2	-	-	-
FeO	9.8	9.8	9.2	9.3	9.4	8.19	9.1	9.8	9.5	9.1
MnO	-	0.4	0.4	-	0.3	0.27	0.3	-	0.4	0.4
MgO	19.8	20.0	20.5	20.5	19.1	18.82	20.7	20.5	20.0	19.9
CaO	27.9	28.4	27.6	27.4	28.3	28.27	28.2	27.9	28.0	27.4
Na ₂ O	0.6	0.7	0.6	0.8	0.4	0.73	0.6	0.6	0.5	0.5
K ₂ O	1.5	1.8	1.7	1.5	1.8	2.02	1.6	1.4	1.7	1.5
P ₂ O ₅	12.1	11.6	11.8	12.0	12.5	13.49	12.2	12.0	12.8	12.4
F ⁻	2.9	-	2.6	2.8	2.5	2.95	2.2	2.0	1	2.6
Cl ⁻	0.2	0.1	0.2	0.3	0.1	0.11	0.2	-	0.1	-
Mg#	78	78	80	80	78	80	80	79	79	80
SiO ₂ + Al ₂ O ₃	22.3	22.7	22.2	22.5	22.2	22.11	21.6	22.3	22.4	22.78
Mg/Ca (mol)	0.98	0.98	1.03	1.04	0.94	0.93	1.02	1.02	0.99	1.01

Table A.13. Electron microprobe analyses of quenched melts (in wt %; normalised to 100% anhydrous) produced in MG-05 (1200°C, 3GPa)

SiO ₂	22.3	21.8	21.3	22.0	21.6	22.0	21.9	21.9	22.3	22.3
TiO ₂	4.5	4.2	4.2	4.4	4.2	4.3	4.3	4.3	4.4	4.5
Al ₂ O ₃	5.2	5.4	5.1	5.2	5.0	5.1	5.3	5.1	5.3	5.4
Cr ₂ O ₃	0.2	-	-	0.2	0.2	-	-	0.2	0.2	0.2
FeO	8.7	8.3	8.2	8.6	8.2	8.6	8.5	8.7	8.6	8.6
MnO	0.3	0.4	0.4	0.3	-	0.2	0.4	0.3	0.3	-
MgO	20.6	21.2	19.9	20.0	20.1	19.9	20.5	20.3	20.0	20.8
CaO	22.3	21.9	23.6	23.1	23.4	23.3	22.5	22.2	22.0	21.5
Na ₂ O	0.4	0.5	0.4	0.4	0.5	0.5	0.5	0.6	0.5	0.6
K ₂ O	1.6	1.5	1.4	1.4	1.2	1.5	1.6	1.5	1.6	1.5
P ₂ O ₅	12.5	12.7	13.7	13.1	13.4	13.7	13.2	13.0	12.9	12.7
F ⁻	2.5	3.3	3.0	2.2	3.8	1.9	2.3	2.9	3.1	3.2
Cl ⁻	0.2	0.2	0.2	-	0.2	-	0.1	0.2	-	0.2
Mg#	81	82	81	81	81	80	81	81	81	81
SiO ₂ + Al ₂ O ₃	27.5	27.2	26.4	27.3	26.6	27.0	27.2	27.0	27.6	27.7
Mg/Ca (mol)	1.28	1.35	1.18	1.21	1.19	1.19	1.27	1.27	1.27	1.35

Table A.14. Electron microprobe analyses of quenched melts (in wt %; normalised to 100% anhydrous) produced in MG-07 (1100°C, 4GPa)

SiO ₂	15.5	15.3	15.4	14.8	11.6	16.5	15.8	15.2	17.1	15.3
TiO ₂	3.5	3.5	3.8	3.2	2.4	3.8	4.2	3.5	4.1	3.6
Al ₂ O ₃	4.6	4.5	4.9	4.5	3.2	4.9	3.6	4.7	5.7	4.9
Cr ₂ O ₃	0.2	-	-	-	-	-	-	-	-	-
FeO	9.9	10.1	9.2	8.6	9.5	10.0	10.1	9.3	8.0	10.2
MnO	0.3	0.3	0.4	0.3	0.4	0.2	1.0	0.4	-	0.3
MgO	24.1	23.5	22.1	23.1	22.8	23.5	23.1	22.1	20.3	22.5
CaO	29.8	30.6	30.1	33.2	34.1	28.8	32.1	31.5	32.4	31.0
Na ₂ O	0.3	0.5	0.4	0.5	0.5	0.7	-	0.5	-	0.5
K ₂ O	1.3	1.4	1.4	1.3	0.8	1.6	1.5	1.5	2.3	1.4
P ₂ O ₅	7.7	7.8	8.9	9.1	11.0	7.7	8.7	8.9	8.2	8.3
F ⁻	4.5	4.7	5.6	2.6	6.2	4.0	-	4.0	3.1	4.4
Cl ⁻	0.2	-	0.2	0.1	0.3	0.2	-	0.2	0.2	0.2
Mg#	81	81	81	83	81	81	80	81	82	80
SiO ₂ + Al ₂ O ₃	20.1	19.7	20.2	19.3	14.8	21.4	19.4	19.9	22.9	19.5
Mg/Ca (mol)	1.13	1.07	1.02	0.97	0.93	1.13	1.00	0.98	0.87	1.01

Table A.15. Electron microprobe analyses of quenched melt (in wt %; normalised to 100% anhydrous) produced in MG-08 (1200°C, 4GPa)

SiO ₂	20.6	21.0	20.9	20.9	20.8	21.2	21.8	21.5	20.5	21.2
TiO ₂	4.1	4.2	4.6	4.2	4.1	4.0	4.2	4.3	4.2	4.2
Al ₂ O ₃	4.4	4.5	4.7	4.7	4.3	4.8	4.8	4.7	4.3	4.6
Cr ₂ O ₃	0.2	0.3	-	-	-	-	0.2	0.2	0.3	-
FeO	11.2	10.3	11.7	10.5	11.6	11.4	11.1	10.8	10.0	10.6
MnO	0.5	0.3	0.3	0.2	-	0.3	0.3	-	0.2	0.3
MgO	21.2	19.4	20.6	20.4	20.7	21.5	20.6	20.7	19.7	20.5
CaO	24.7	25.6	24.4	25.0	24.7	23.7	23.5	23.9	25.3	24.2
Na ₂ O	0.3	0.4	0.3	-	0.3	0.3	0.3	-	0.5	-
K ₂ O	1.1	1.4	1.7	1.7	1.3	1.6	1.0	1.2	1.6	1.9
P ₂ O ₅	9.9	11.0	9.5	10.5	10.2	9.7	10.4	10.1	10.9	10.6
F ⁻	2.6	2.0	1.8	2.8	3.0	2.2	2.4	3.5	3.5	2.9
Cl ⁻	0.6	0.6	0.5	0.4	0.4	0.3	0.6	0.6	0.4	0.4
Mg#	77	77	76	78	76	77	77	77	78	77
SiO ₂ + Al ₂ O ₃	24.9	25.5	25.5	25.7	25.1	26.0	26.5	26.3	24.8	25.7
Mg/Ca (mol)	1.19	1.05	1.17	1.13	1.17	1.26	1.22	1.20	1.08	1.18

Table A.16. Electron microprobe analyses of quenched melt (in wt %; normalised to 100% anhydrous) produced in MG-09 (1100°C, 4GPa, 6hours)

SiO ₂	29.6	30.0	34.9	29.7	33.4
TiO ₂	3.2	2.7	4.6	3.8	3.6
Al ₂ O ₃	13.3	13.3	3.8	12.9	13.8
Cr ₂ O ₃	-	-	0.3	-	-
FeO	12.9	11.8	15.3	13.3	11.9
MnO	0.2	-	-	-	0.3
MgO	15.2	15.5	20.8	14.9	16.9
CaO	13.4	14.0	16.6	13.3	8.7
Na ₂ O	1.0	1.0	0.3	1.0	0.9
K ₂ O	6.1	6.2	1.5	6.0	6.9
P ₂ O ₅	3.6	4.3	0.4	3.8	2.6
F ⁻	2.3	1.9	2.3	1.8	1.7
Cl ⁻	0.4	0.3	0.3	0.5	0.4
Mg#	68	70	71	67	72
SiO ₂ + Al ₂ O ₃	42.9	43.2	38.75	42.5	47.1
Mg/Ca (mol)	1.59	1.54	1.74	1.56	2.70

Table A.17. Electron microprobe analyses of quenched melts produced in the experiments. Recalculated to molar concentration.

Exp	MG-01	MG-04	MG-05	MG-07	MG-08	MG-09
P (GPa)	2	3	3	4	4	4
T (°C)	1100	1100	1200	1100	1200	1100
Dur (Hrs)	48	24	24	24	24	6
Si	6.98	6.88	8.22	5.86	8.03	11.92
Ti	0.57	1.29	1.22	1.03	1.21	1.01
Al	2.97	2.00	2.30	2.03	2.06	5.07
Cr	0.00	0.01	0.04	0.01	0.04	0.02
Fe	3.79	3.00	2.66	3.05	3.49	4.13
Mn	0.10	0.08	0.08	0.12	0.08	0.03
Mg	10.58	11.45	11.36	13.00	11.69	9.39
Ca	15.57	11.51	9.06	12.90	10.02	5.35
Na	0.61	0.45	0.35	0.29	0.18	0.61
K	0.21	0.80	0.70	0.71	0.71	2.57
P	0.95	4.00	4.15	2.80	3.33	0.94
Ni	0.00	0.00	0.00	0.00	0.00	0.00
F	5.17	2.47	3.32	4.73	3.22	2.39
Cl	0.10	0.08	0.08	0.10	0.31	0.22
O	52.39	55.99	56.45	53.39	55.65	56.34
Mg#	74	79	81	81	77	69

Appendix 5: Electron microprobe analyses and back-scattered electron images of MG-11 (1300°C, 3GPa).**Table A.18. Electron microprobe analyses of orthopyroxene, clinopyroxene and olivine produced in MG-11 (1300°C, 3GPa). Mineral formulae were calculated on the basis of 6 oxygens for ortho-and clinopyroxene and on the basis of 4 oxygens for olivine.**

	Orthopyroxene Core				Orthopyroxene Rim				Clinopyroxene	
SiO ₂	57.4	58.0	57.2	56.9	58.2	58.1	58.6	58.3	53.7	53.8
TiO ₂	-	-	0.2	-	-	-	-	-	0.9	0.9
Al ₂ O ₃	1.4	0.6	1.3	1.5	0.8	0.8	0.8	0.9	2.9	2.8
Cr ₂ O ₃	0.7	0.6	0.8	0.8	0.5	0.5	0.3	0.6	1.1	0.8
FeO	3.7	3.6	3.8	3.9	2.8	2.8	2.4	2.4	2.2	2.2
MnO	0.2	-	-	0.2	-	-	-	0.2	-	-
MgO	34.8	35.5	34.5	34.4	36.2	36.0	36.5	36.2	25.7	25.6
CaO	1.7	1.4	1.7	1.8	1.5	1.5	1.6	1.8	13.7	13.4
Total	99.89	99.8	99.5	99.4	100.0	99.7	100.2	100.4	100.2	99.6
xO ²⁻	6	6	6	6	6	6	6	6	6	6
Si	1.97	1.98	1.97	1.96	1.98	1.98	1.98	1.98	1.89	1.91
Ti	-	-	0.01	-	-	-	-	-	0.02	0.02
Al	0.06	0.02	0.05	0.06	0.03	0.03	0.03	0.04	0.12	0.12
Cr	0.02	0.02	0.02	0.02	0.01	0.01	0.01	0.02	0.03	0.02
Fe ²⁺	0.10	0.10	0.11	0.11	0.08	0.08	0.07	0.07	0.06	0.07
Mn	0.01	-	-	0.00	-	-	-	0.01	-	-
Mg	1.78	1.81	1.77	1.77	1.84	1.83	1.84	1.83	1.35	1.35
Ca	0.06	0.05	0.06	0.07	0.05	0.06	0.06	0.06	0.52	0.51
ΣCations	4.00	4.00	3.99	4.00	4.00	3.99	3.99	4.00	4.00	4.00
Mg#	94	95	94	94	96	96	96	96	96	95

Table A.18. continued

	Olivine Core				Olivine Rim			
SiO ₂	41.6	41.3	41.8	41.5	41.8	41.8	41.6	41.9
FeO	6.1	6.6	6.5	6.0	5.5	5.7	5.3	4.6
MnO	-	0.2	-	-	-	-	0.2	-
MgO	52.1	51.8	52.2	52.3	52.6	52.3	52.7	53.4
CaO	-	-	-	0.2	0.1	0.1	-	0.2
Total	99.8	99.9	100.5	100.0	100.1	99.9	99.7	100.2
xO ²⁻	4	4	4	4	4	4	4	4
Si	1.00	1.00	1.00	1.00	1.00	1.00	1.00	1.00
Fe ²⁺	0.12	0.13	0.13	0.12	0.11	0.12	0.11	0.09
Mn	-	0.00	-	-	-	-	0.00	-
Mg	1.87	1.87	1.87	1.88	1.88	1.87	1.89	1.90
Ca	-	-	-	0.00	0.00	0.00	-	0.01
ΣCations	3.00	3.00	3.00	3.00	3.00	3.00	3.00	3.00
Mg#	94	93	93	94	94	94	95	95

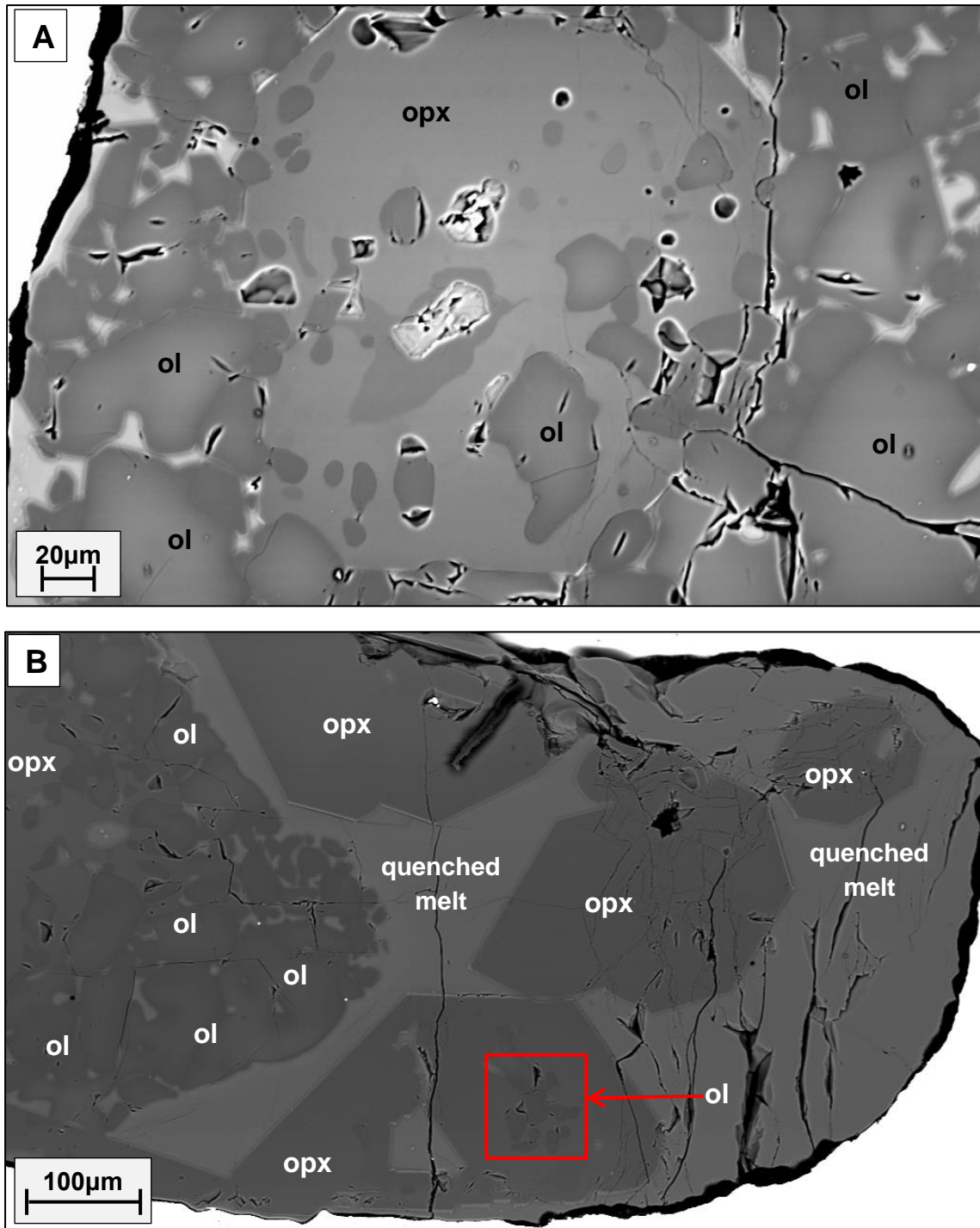


Figure A.7: Back-scattered electron images of MG-11 (1300°C, 3GPa). A: zoned subhedral olivine surrounding large orthopyroxene crystal. The orthopyroxene encloses anhedral grains of zoned olivine. B: large euhedral orthopyroxene crystals within large pools of quenched melt. Zoned subhedral to euhedral olivine is located toward the left in the BSE-image.

Appendix 6: Compositions of melts produced in the experiments of Jacobs (2012) and Burness (2013) and the modal proportion estimates of run products of Jacobs (2012) and Burness (2013)

Table A.19. Electron microprobe analyses of quenched melts (wt %; normalised to 100% anhydrous) produced in the experiments of Jacobs (2012) and Burness (2013).

	Jacobs (2012)							Burness (2013)				
	Bulk Starting material	Exp P (GPa) T (°C) Dur (hrs)	DK2	DK15	DK16	DK19	DK18	Bulk Starting Material	Exp P (GPa) T (°C) Dur (hrs)	SB-01	SB-02	SB-03
SiO ₂	34.16		30.62	25.53	28.30	28.75	26.81	33.00		36.56	37.55	38.37
TiO ₂	1.78		1.42	2.10	2.57	1.64	3.12	2.04		1.46	3.09	0.73
Al ₂ O ₃	3.10		8.62	6.11	5.67	7.46	4.64	3.69		3.18	7.05	4.60
Cr ₂ O ₃	0.31		0.02	0.03	0.06	0.06	0.14	0.21		0.79	0.83	-
FeO	9.96		3.21	9.11	7.78	5.25	11.51	10.39		9.46	6.65	9.67
MnO	0.17		0.08	0.24	0.17	0.12	0.23	0.19		0.30	-	-
MgO	31.66		28.16	24.98	25.19	28.94	23.20	28.78		29.33	16.29	15.66
CaO	13.05		15.12	19.92	16.75	14.40	20.20	14.65		15.48	19.43	22.57
Na ₂ O	0.31		0.91	0.24	3.22	0.64	0.30	0.78		-	0.35	3.07
K ₂ O	1.01		0.36	0.56	1.57	1.30	0.99	1.16		0.98	5.37	1.62
P ₂ O ₅	4.26		8.03	9.64	7.79	9.96	8.21	4.88		1.85	0.40	1.03
SO ₃	0.03		0.42	0.35	0.02	0.10	0.09	0.04		-	-	-
NiO	0.17		0.05	0.04	0.04	0.02	0.04	0.19		-	-	-
F	-		2.97	1.14	0.88	1.36	0.53	-		-	2.98	2.68
Cl	-		-	-	-	-	-	-		-	-	-
Mg#			94	83	85	91	78			85	81	74
SiO ₂ + Al ₂ O ₃			39.24	31.64	33.97	36.21	31.45			39.74	44.60	42.97
Mg/Ca (Mol)			2.59	1.74	2.09	2.79	1.60			2.64	1.17	0.97

Table A.20. Modal mineralogy (in wt %) produced in the experiments of Jacobs (2012) and Burness (2013)

	Jacobs (2012)					Burness (2013)		
Exp	DK2	DK15	DK16	DK19	DK18	SB-01	SB-02	SB-03
P (GPa)	2	3	3	3.5	3.5	2	3	4
T (°C)	1100	1100	1200	1100	1200	1100	1100	1100
Duration (hrs)	48	48	48	48	48	24	24	24
Opx	0.0	0.8	15.0	0.1	0.6	0.0	0.0	3.0
Cpx	16.7	15.9	10.5	17.4	10.0	8.0	5.8	1.0
Omp	0.0	0.0	0.0	0.0	0.0	1.6	0.0	0.0
OI	36.2	35.0	20.9	36.2	35.0	19.2	41.9	45.0
Spl	8.9	7.5	8.6	6.9	1.1	0.0	5.6	0.0
Phl	0.2	1.0	0.0	0.9	0.0	0.0	1.0	7.0
Ap	6.6	4.0	0.0	5.7	0.0	6.5	12.3	12.7
Melt	31.3	35.8	45.0	32.8	53.3	67.1	34.2	31.8